Probing the Gas-Phase Interactions of Ions with Molecules of Biological Significance

Thomas F.M. Luxford

A thesis presented for the degree of Master of Science by Research

University of York

Department of Chemistry

November 2013

Abstract

Ionic complexes containing biological molecules have been prepared in the gas-phase using electrospray-ionisation, to allow for the investigation of their structures using collision-induced dissociation within a quadrupole ion trap. These complexes have been studied as model systems for characterising the non-covalent interactions of biological molecules, without complication from a bulk solvent or crystal lattice.

The first series of experiments investigated the hydrogen bonding interactions between the nucleobases adenine, cytosine, thymine and uracil with the platinum cyanide dianions $[Pt(CN)_4]^{2-}$ and $[Pt(CN)_6]^{2-}$. The $[Pt(CN)_6M_n]^{2-}$ clusters fragmented by the sequential dissociation of the neutral nucleobases, while the $[Pt(CN)_4M_n]^{2-}$ clusters fragmented by either sequential dissociation of the nucleobases or by proton transfer to form $[Pt(CN)_4H]^-$. DFT calculations were performed to support the interpretation that multiple nucleobases bind independently to different sites on the dianion. Comparison of the energies required for fragmentation of the various complexes allowed for the relative binding energies of the different nucleobases to the dianions to be determined.

Next, complexes of arginine with deprotonated monocarboxylic acids, $H_3C(CH_2)_nCO_2{\cdot}Arg^-$, and dicarboxylic acids $HO_2C(CH_2)_nCO_2^-$, were investigated to probe the nature of the interactions as a function of anion size. For the dicarboxylic acid clusters, the chain length was found to have a significant effect on the fragmentation energy of the complexes, with the n=9 and 10 systems fragmenting at significantly lower energies than the corresponding shorter chain analogues. Molecular mechanics calculations indicate that the dicarboxylic acid complexes transition to a ring-structure as the acid chain length increases.

The final series of experiments investigated subnanometre clusters using electrospray-ionisation mass spectrometry, synthesised in-house using previously published methods. Systems consisting of tryptophan and silver nitrate, histidine and chloroauric acid, glutathione and gold nanoparticles, and mercaptosuccinic acid and silver nitrate were investigated, however, no suitable system was found. Suggestions for further work in this area are also described.

Contents

List of Figures

Chapter 2: Experimental and Theoretical Techniques

Chapter 3: Hydrogen Bonding Interactions of Nucleobases with Multiply Charged Anions $[Pt(CN)_6]^{2-}$ and $[Pt(CN)_4]^{2-}$

Chapter 4: Effects of Varying Chain Length on the Interaction of Carboxylate Anions with Gas-Phase Arginine

Chapter 5: Potential Syntheses and Electrospray Ionisation Mass Spectrometry of Subnanometre Clusters

List of Tables

Chapter 3: Hydrogen Bonding Interactions of Nucleobases with Multiply Charged Anions $[Pt(CN)_6]^{2-}$ and $[Pt(CN)_4]^{2-}$

Chapter 4: Effects of Varying Chain Length on the Interaction of Carboxylate Anions with Gas-Phase Arginine

Acknowledgements

I would like to thank my supervisor Dr Caroline Dessent for her continued advice and support during my time in the group. I would also like to thank Dr Ed Bergström for his training on the spectrometers and for his help when things didn’t work as expected. Finally, I would like to thank Dr Naruo Yoshikawa, Andy Harvey and Dr Ananya Sen for all their help and for making day to day life enjoyable.

Author's Declaration

I hereby certify that the research presented in this thesis is my own and to the best of my knowledge, is original except where due reference has been made to other workers.

The research presented in *Chapter 4* builds on results presented in the thesis of Edward Milner (E.M. Milner, MSc Thesis, University of York, 2010). The research presented in *Chapter 5* involves the replication four literature syntheses (T. Tabarin, R. Antoine, M. Broyer and P. Dugourd, *The European Physical Journal D*, 2006, **37**, 237-239; X. Yang, M. Shi, R. Zhou, X. Chen and H. Chen, *Nanoscale*, 2011, **3**, 2596-2601; R. Zhou, M. Shi, X. Chen, M. Wang and H. Chen, *Chemistry – A European Journal*, 2009, **15**, 4944-4951; T. U. B. Rao, B. Nataraju and T. Pradeep, *Journal of the American Chemical Society*, 2010, **132**, 16304-16307).

Chapter 1

Introduction

1.1 Studying Non-Covalent Complexes of Biological Molecules in the Gas-Phase

Non-covalent interactions are of great importance in biological systems. For example, the binding of DNA to form its characteristic double helical structure,[1] the solvation of proteins into their biologically active folded structures[2] and many drug-target interactions[3] all depend on various non-covalent interactions. The gas-phase provides a unique environment for the detailed study of these non-covalent interactions, away from the perturbations that can occur in either bulk solutions or the solid-phase.[4, 5]

While a great variety of gas-phase molecular complexes have been studied over the last twenty five years,[6] in the last decade, there has been a surge in interest in the characterisation of non-covalent complexes containing biological molecules.[7] The detailed geometric structures of such complexes, obtained through experimental methods provide a powerful insight into the non-covalent interactions of biomolecules. Furthermore, these geometric structures provide important benchmarks against which theoretical methods can be tested, since non-covalent interactions continue to provide a challenge to high-level computational theory.[8, 9]

Although much information can be gained from studies in the gas-phase, biological molecules typically exist in condensed phases. This can lead to questions of relevance, as the properties of molecules in the gas and condensed phases differ significantly. For example, in solution, deprotonated tyrosine exists almost entirely in its carboxylate form, while when transferred to the gas-phase, it exists as a mixture of its carboxylate and phenoxide forms.[10] Despite these differences, gas-phase studies have proved to be useful in obtaining a range of information regarding the conformation of biomolecules, which cannot be as easily obtained through the study of these molecules in the condensed phase.[11] For example, Barran et al. used gas-phase techniques to determine the conformation of the gonadotropin-releasing hormone and two novel β-defensins and successfully related these structures of these peptides to their biological activity.[5]

In this introductory chapter, a brief overview of previous studies of gas-phase biomolecule complexes is presented, including a review of the methods used to generate the gas-phase biomolecules and the experimental techniques that have been applied to characterise their structures. A short review of the theoretical methods generally applied to interpret experimental results on these systems is also presented.

1.2 Techniques for Producing Gas-Phase Complexes of Biological Molecules

The earliest studies of gas-phase biomolecule complexes involved the production of uncharged clusters in molecular beams using supersonic jet expansions.[12-15] Biomolecules were typically heated to vaporisation and mixed with a noble gas prior to supersonic expansion. However, this is not an ideal technique, as many biomolecules are unstable at high temperatures and will decay before their vaporisation temperature is reached. The use of laser ablation circumvents this problem by vaporising the biomolecules without the need for significant heating.[16, 17]

The ablated biomolecules will pass through a molecular beam of a noble gas and become entrapped. Once in the molecular beam, the biomolecules will undergo collisional cooling, at which point it is possible for them to aggregate to form molecular clusters.[18]

Gas phase ions can be produced by the soft ionisation techniques electrospray ionisation (ESI) and matrix-assisted laser desorption ionisation (MALDI). ESI and MALDI were developed in the 1980s by John Fenn[19-21] and Franz Hillenkamp[22] respectively, with the 2002 Nobel Prize in chemistry awarded to John Fenn and Koichi Tanaka for the development of these techniques.[23, 24] In ESI, a precursor solution is passed through a charged needle, in which ions will accumulate at the tip and highly charged droplets will be ejected. These droplets will evaporate to leave the bare gas-phase ions.[23] In MALDI, a UV laser is fired at a matrix containing a precursor to the ion. This results in desorption and ionisation of the matrix and analyte molecules to form gas-phase ions.[25, 26] Both ESI and MALDI are useful techniques for the production of gas-phase biomolecular ions, as they leave very little residual energy on the analyte, meaning that fragmentation is unlikely. Furthermore, this can allow for weak non-covalent interactions to be retained upon the transfer of the analyte to the gas-phase, making them ideal for the generation of molecular clusters.[27]

1.3 Experimental Techniques for Studying Non-Covalent Complexes of Gas-Phase Biological Molecules

Electronic spectroscopy of uncharged complexes in a molecular beam can be achieved using laser spectroscopy techniques such as laser induced fluorescence[28] and resonance enhanced multiphoton ionisation (REMPI).[29] Fourier transform IR and Fourier transform microwave spectroscopy can be used to obtain vibrational[30] and rotational spectra,[31, 32] respectively. Nir et al. have used vibrationally resolved REMPI spectroscopy to investigate the interactions between different nucleobases in base pairs, with complexes such as guanine-cytosine and guanine-guanine.[33, 34] The comparison of the experimental REMPI spectra to those obtained theoretically using *ab initio* methods allowed for the gas-phase structure of these complexes to be determined.

Electronic and vibrational spectroscopy of ions in a mass spectrometer is possible using ultraviolet photodissociation (UVPD)[35] and infrared multiphoton dissociation (IRMPD)[36] respectively. In these methods, the ion being investigated is isolated and is subsequently fragmented using a laser pulse to produce a fragment ion. Repeating this fragmentation at different laser wavelengths can be used to generate a plot of fragment ion intensity as a function of wavelength. As fragmentation will only occur following excitement at a resonant frequency, this method allows for an ‘action spectrum’ of the ion to be generated.[37, 38] Williams et al. used IRMPD to investigate the stabilisation of the zwitterionic structure of arginine by the complexation of different species. By comparing the experimentally and theoretically obtained IR spectra, the relative proportions of canonical and zwitterionic amino acid can be determined. From this, the gas-phase zwitterionic structure of arginine has been shown to be stabilised relative to the non-zwitterionic form by alkali metal cations, halide anions and water molecules.[39-41]

Collision induced dissociation (CID) mass spectrometry can be used to probe the lowest energy pathways for the fragmentation of an ion. This can be used to provide information relating to the structure of the ion. An electric field is used to increase the kinetic energy of the precursor ion and accelerate it into an inert target gas. Over the course of hundreds of collisions with the target gas, the excess kinetic energy of the ion will be converted into vibrational energy. This process will continue until an energy threshold is reached, leading to fragmentation of the ion.[42-45] CID has been used to examine the interactions of nucleobases with metal cations. Vrkic et al. used mass spectrometry to map the aggregation of adenine and silver (I) cations in the gas-phase, and CID to probe their structures.[46, 47] More recently, Ali et al. used CID to investigate the structures of complexes containing the nucleobase uracil with a range of metal dications.[48, 49] CID has also been used to investigate the structure of amino acids in the gas-phase, as zwitterionic and canonical amino acids will fragment through different channels. This has been used to provide complimentary results to the IRMPD studies described above and show that alkali metal cations and halide anions will effectively stabilize the zwitterionic form of arginine, relative to the canonical form.[50, 51]

Ion mobility spectrometry (IMS) is a distinctive technique which has grown considerably in popularity in recent years.[52] It uses an electric field to direct ions through a drift tube containing an inert gas. The time for an ion to pass through the drift tube will be directly related to the collision cross section of the ion.[52] Comparison of the experimentally obtained collision cross section of the ion to those obtained theoretically from molecular models can allow for a great deal of structural information to be obtained, as each conformer will have a characteristic collision cross section.[52-54] IMS is an ideal method for the study of very large ionic systems, and has been used to investigate the structure of complexes containing multiple proteins.[55-57] Duijn et al. used the technique to examine the GroEL-GroEL protein dimer, which plays an important role in the biological activity of the *e-coli* bacterium.[58]

1.4 Computational Techniques for Studying Non-Covalent Complexes of Gas-Phase Biological Molecules

It is not always possible or practical to produce certain biomolecule complexes as isolated species in the gas-phase and in such situations, theoretical methods provide an ideal way to probe their properties in the absence of experimental data. For example, De Leon et al. used computational methods to investigate the non-covalent interactions of amino acids with [80] fullerene.[59] Moreover, theoretical techniques are essential in this general area as a compliment to experimental results, as has been mentioned above for the interpretation of spectroscopic, CID and IMS data.

Larger systems can be challenging to study with pure *ab initio* methods due to the large number of electrons present. Density functional theory (DFT) methods provide a more accessible alternative for such systems.[60] Older functionals do not provide a proper treatment of dispersion interactions, which play an important role in the structure of non-covalent complexes.[61] Recently, considerable effort has been expended in developing dispersion-corrected density functionals, for example MO6[62-64] and DFT-D3,[65] which provide a much better approximation of the intermolecular interactions.[66-68] These newer functionals appear to provide a good balance between computational cost and performance for larger biomolecular systems that include dispersion interaction.

1.5 Overview of Thesis

The primary goal of this thesis is to investigate the non-covalent interactions and geometric structures of gas phase complexes of biological molecules. Such complexes are characterised using low-energy collision induced dissociation to probe the fragmentation channels and fragmentation energies of the different systems. The ultimate aim of this research is to characterise systems that will be investigated in future laser spectroscopy experiments using a commercial mass spectrometer that has been modified for laser spectroscopy.

Chapter 2 describes the experimental and theoretical techniques that are used in the following chapters. *Chapter 3* describes a series of complexes made up of a platinum cyanide multiply charged anion, $[Pt(CN)_6]^{2-}$ or $[Pt(CN)_4]^{2-}$ with one or more nucleobases, and *Chapter 4* describes a series of complexes containing the amino acid arginine and various carboxylate anions. In both chapters, an experimental study using collision induced dissociation is conducted to probe the non-covalent interactions within the complexes, and a computational study is conducted to aid the interpretation of the experimental results. *Chapter 5* describes attempts to synthesise subnanometre clusters that could be introduced into the gas-phase using electrospray ionisation. These subnanometre clusters were investigated as the basis for potential complexes with biomolecules.

Chapter 2

Experimental and Theoretical Techniques

2.1 Bruker Esquire 6000 Quadrupole Ion Trap Mass Spectrometer

The mass spectrometry experiments described in *Chapters 3-5* were conducted using a Bruker Esquire 6000 quadrupole ion trap mass spectrometer.[69] The mass spectrometer is a benchtop instrument and has three sections: the electrospray ionisation source, the ion optics and the quadrupole ion trap mass analyser. These stages are described in the following sections. The spectrometer is setup to allow for tandem mass spectrometry using collision induced dissociation within the quadrupole ion trap, which is also discussed.

This instrument allows for mass spectra to be taken up to a mass to charge ratio (*m/z*) of 35-3000 in normal mode, with a typical resolution of *m/z* 0.35 (full width half maximum) and allows for tandem mass spectrometry up to MS^{11}.

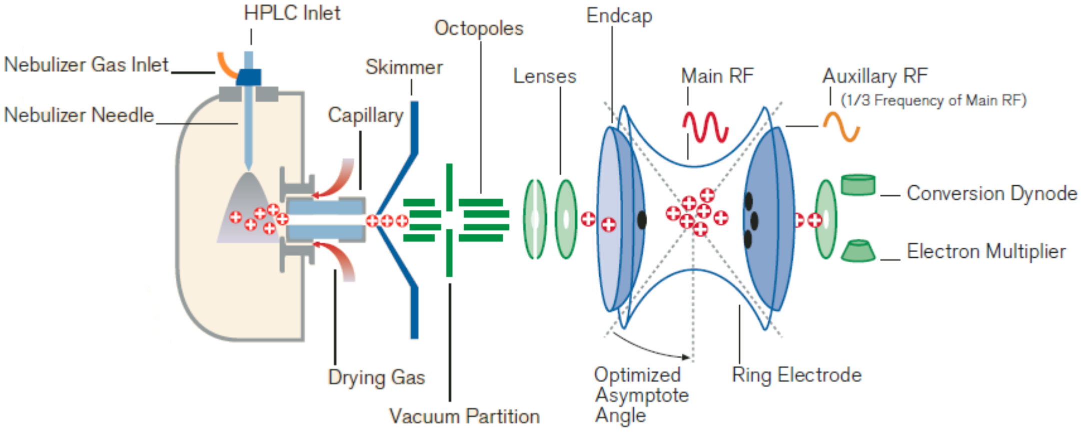

Figure 2.1: Schematic of the Bruker Esquire 6000 mass spectrometer. Adapted from [69].

2.1.1 Electrospray Ionisation

While the Bruker Esquire 6000 mass spectrometer has a number of ionisation source options, all experiments described in this thesis used the electrospray ionisation (ESI) source. The Agilent ESI source is set up slightly differently from the traditional design, with an orthogonal sprayer design. This design increases sensitivity, robustness and reproducibility of the spectrometer for a wide range of injection conditions.[69] Once they have been electrosprayed, the ions will move into a perpendicular electrostatic field, which will direct them through a transport capillary, a skimmer and into the ion optic region.

Despite the novel setup, the ESI source will function similarly to traditional designs.[20, 23] A solution containing a precursor to the desired ions is put into a syringe and is injected through a fused-silica capillary at a constant rate (typically 2-5 μL min^{-1}) using a syringe driver. The capillary will transport the solution to a charged needle, in which ions will accumulate at the tip to form a Tayor cone.[70] With the help of a nitrogen nebulizer gas, highly charged droplets will break off of the tip of the cone and will begin to evaporate. This results in an increase in the electrostatic repulsion from the ions in the droplet, and when a small enough radius is reached, the repulsion becomes large enough to overcome the surface tension of the solvent. When this occurs, the droplet will undergo Coulomb fission producing a number of smaller, charged 'progeny' droplets, which will then repeat the process of solvent evaporation and fission.[71]

The final conversion of charged droplets to bare gas phase ions can be explained by two models. In the charge residue model, the cycle of solvent evaporation and Coulomb fission will continue until a droplet contains only a single ion, at which point the remaining solvent will evaporate to leave the bare ion.[72, 73] In the ion evaporation model, once the droplets reach a small enough size, the Coulombic repulsions become sufficiently strong to eject an ion on the surface of the droplet out into the gas phase.[74] While not fully understood, both mechanisms have proved to be valid under different conditions.[75] It has been observed that smaller ions, such as the ones investigated in this thesis, appear to enter the gas phase mainly through the ion evaporation mechanism.[76]

The ions will be directed through a heated capillary (typically 100-300°C), which along with a nitrogen drying gas, will remove any remaining solvent from the ions. Finally, the ions will pass through a skimmer and into the ion optic region of the mass spectrometer.

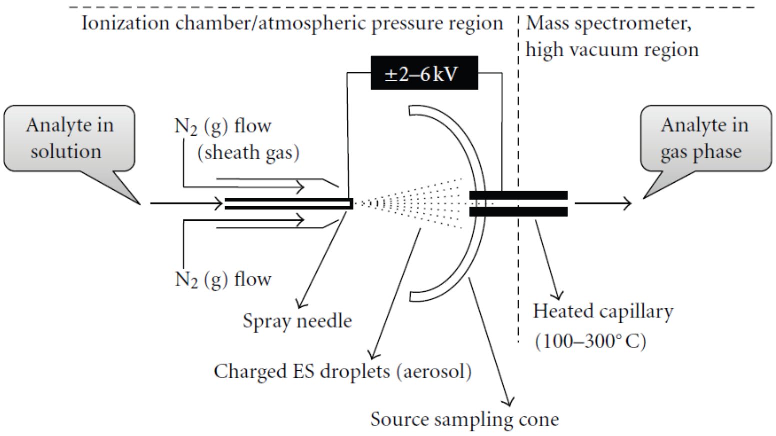

Figure 2.2: Schematic representation of an electrospray ionisation source. Adapted from [77].

2.1.2 Ion Optics

In order for the ions to be detected, they must pass from the atmospheric pressure ionisation chamber to the low pressure ion trap region of the instrument. This is achieved using a set of ion optics to transfer the ions between the different pumping regions. The ions will enter an octupole, which will direct them through a vacuum partition and into a second octupole. This octupole then directs the ions through a pair of electrostatic lenses, which focus the ions into the quadrupole ion trap.

2.1.3 Quadrupole Ion Trap

The quadrupole ion trap (QIT) constrains ions within an area of space using electrostatic forces from three electrodes: two hyperbolic end-cap electrodes and one ring electrode.[78, 79] Ions within the trap will move in a Lissajous curve (the shape of a distorted figure eight), as described by the Mathieu equation.[80, 81] As the ions are of the same charge, they will repel each other, leading to a gradual expansion of their trajectories over time, eventually resulting in the uncontrolled ejection of the ions from the trap. This is avoided by the presence of a damping gas, usually helium, at a low pressure ($\sim 10^{-3}$ Torr) within the trap. Collisions of the ions with helium will remove the excess energy and prevent expansion of the ions, in a process referred to as ion cooling.[78]

Ions can be ejected from the QIT using a technique termed resonant excitation, which involves the application of an oscillating potential to the end cap electrodes, resulting in the acceleration of ions out of the QIT. Resonance excitation at a given frequency of oscillation will correspond to the ejection of ions with a specific *m/z*.[78]

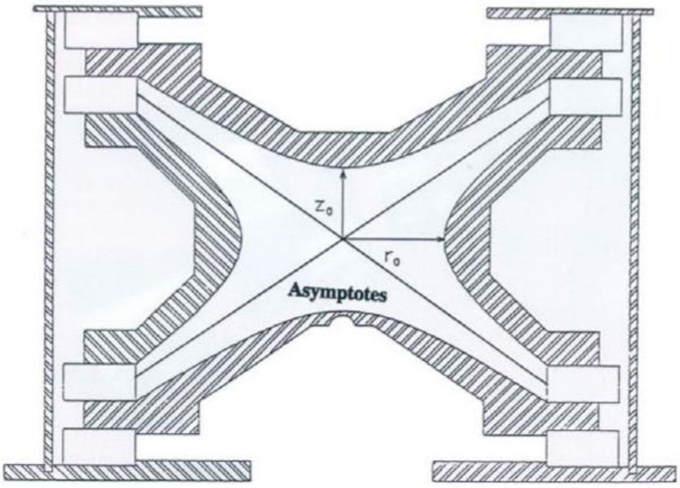

Figure 2.3: Schematic representation of the quadrupole ion trap. Adapted from [78].

In the Bruker Esquire 6000 mass spectrometer, ions will enter the QIT through a hole in one of the end cap electrodes. The ions will be held in the QIT for a short period of time before being scanned out using resonance excitation and into a detector. This will generate a plot of ion intensity against RF voltage, which is calibrated to produce the mass spectrum. The mass spectra presented in this thesis are produced by averaging many individual mass spectra produced in the manner described here.

2.1.4 Collision Induced Dissociation

The Bruker Esquire 6000 mass spectrometer is setup to allow for tandem mass spectrometry in the QIT using collision induced dissociation (CID). For this the target ion must first be ‘mass selected’, which involves ejecting ions of all other *m/z* out of the QIT using resonance excitation. Next, resonance excitation is used to carefully accelerate the remaining ions without ejecting them from the QIT. The accelerated ions will collide with the helium buffer gas, which over hundreds of collisions will result in the increased translational energy being converted into vibrational energy. Once a singly charged ion obtains enough vibrational energy to overcome the lowest energy transition state, it will fragment to form a neutral fragment and an ionic fragment.[81] The mass selection and CID stages may be repeated up to eleven times, as long as there is sufficient ion intensity. Finally, the remaining ions are scanned out of the QIT and a fragmentation mass spectrum is generated.[78] Examples of spectra produced at different points in this process are shown in *Figure 2.4*.

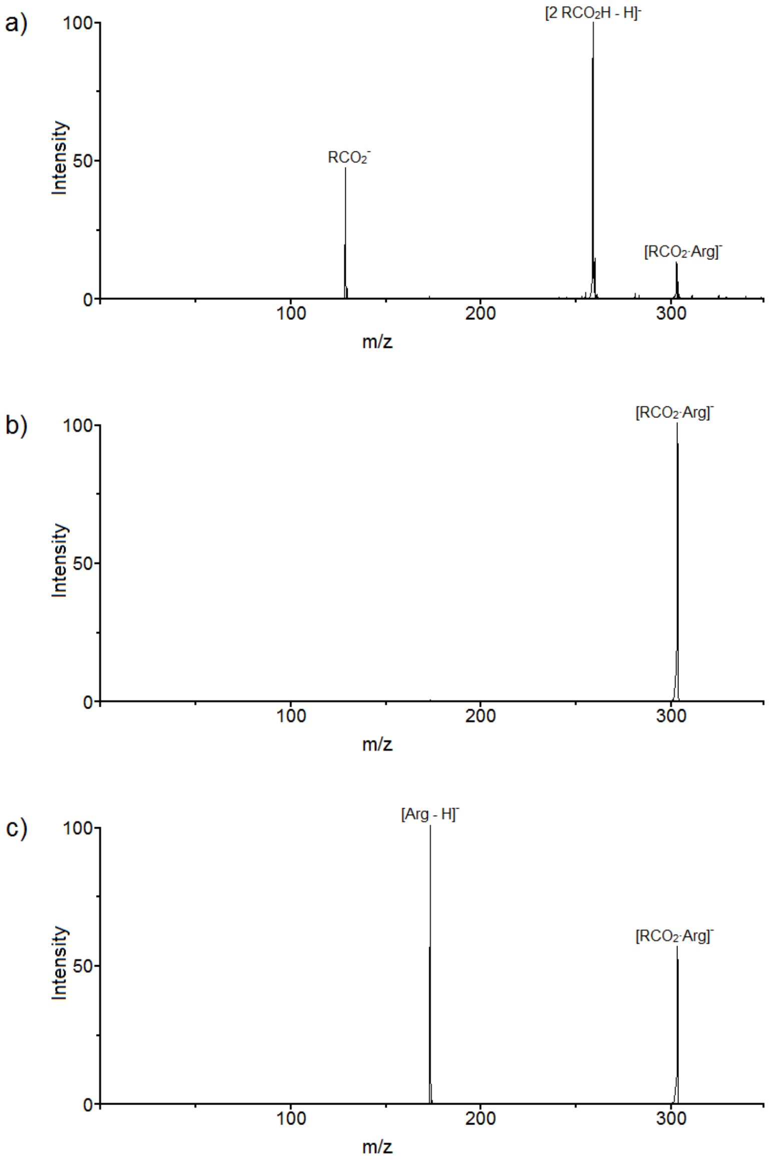

Figure 2.4: a) Negative ion mass spectrum of a mixture of arginine (Arg) and enanthic acid (RCO_2H), b) mass spectrum of mass selected $[RCO_2{\cdot}Arg]^-$ cluster ion prior to collision induced dissociation, c) mass spectrum of $[RCO_2{\cdot}Arg]^-$ ion after collision induced dissociation. More information about this system is given in *Chapter 4*.

By varying the end cap voltage, the energy transferred to the ions in CID can be controlled.[82] Comparing the energies at which ions fragment will provide an insight into the relative barrier heights for the fragmentation mechanisms of different ions.[83] In this thesis, this is achieved by plotting the relative intensities of the precursor and fragment ions against fragmentation energy to produce a CID curve and taking the energy at which the relative intensity of the precursor ion reaches 50% ($E_{1/2}$). An example CID curve is displayed in *Figure 2.5*.

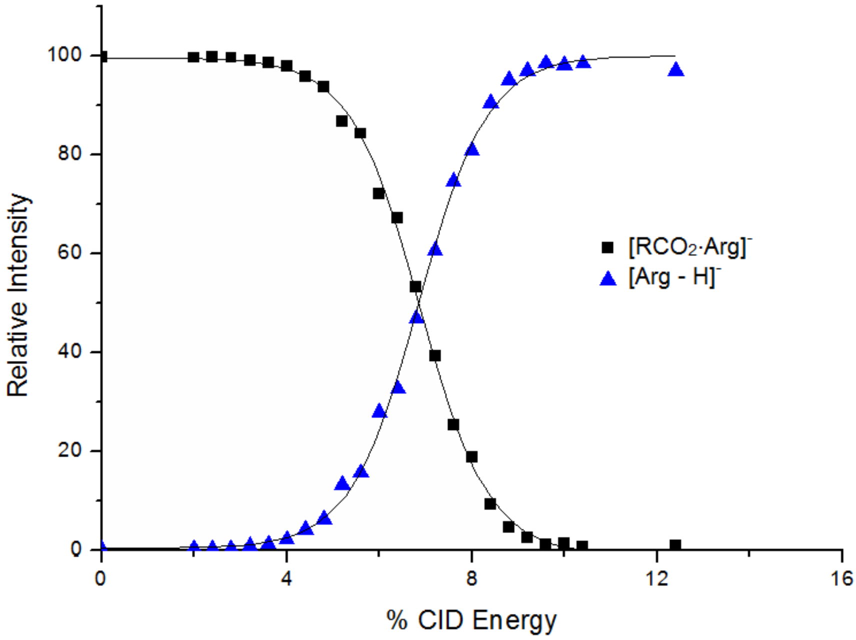

Figure 2.5: % fragmentation curve for the collision induced dissociation of enanthic acid and arginine cluster ($[RCO_2{\cdot}Arg]^-$). More information about this system is given in *Chapter 4*.

The energy transferred to the ions upon excitation is not perfectly uniform, and larger ions receive slightly less energy and so will fragment at higher voltages. This means that the fragmentation energies should not be directly compared for ions with significantly different mass to charge ratios. Typically, the maximum difference required for comparison of energies is considered to be m/z 100.[84] Additionally, this means that the conversion from end cap voltage to absolute collision energy is complicated and requires extensive calibration of the spectrometer. The collision energies in this thesis are therefore quoted as "% CID energy", where 100% is the maximum end cap voltage of the spectrometer.

2.2 Computational Methods

2.2.1 Density Functional Theory

Quantum mechanical calculations are based on solving the Schrödinger equation (2.1),

$$H\Psi = E\Psi \tag{2.1}$$

Where H is the Hamiltonian operator, E is the energy and Ψ is the wavefunction of the system. By solving the Schrödinger equation, the energy of a particular molecular arrangement can be determined, allowing for a potential energy surface (PES) to be obtained. By calculating the first derivative of the energy, local minima on the PES can be obtained. This is the principle by which *ab initio* structure optimisations, such as the ones described in *Chapter 3* are conducted.

The Born Oppenheimer approximation greatly simplifies the Schrodinger equation by treating the motion of the electrons and nuclei separately, from which the electronic Hamiltonian is reduced to three terms: the electron kinetic energy, electron nucleus attraction and the electron-electron repulsion.[85] In density functional theory calculations, the energy of a system is determined using a functional of the electron density, referred to as a basis set.[86, 87] The basis set used for the calculations in *Chapter 3* are described in more detail in *Section 3.3.2*.

2.2.2 Molecular Mechanics

Molecular mechanics uses classical mechanics to provide a computationally inexpensive way to calculate the energy and geometry of a molecular system. Force fields, which contain empirically derived information relating to the energy associated with various structural parameters are used to calculate the potential energy of a given molecular arrangement.[88, 89] Structure optimisation is achieved using an energy minimisation algorithm. In this, the structure is modified slightly and the energy is recalculated. If the recalculated energy is lower, then the process will be repeated for the new structure, but if the recalculated energy is higher, the process is repeated for original structure with a different modification. This will be repeated until a local minimum on the PES is obtained.[90]

Conformer searches, such as the ones described in *Chapter 4*, can be used to quickly obtain a large number of low-energy structures. A process referred to as simulated annealing is used to simulate the cooling of a structure from a high temperature. At high temperatures, the structure can ‘escape’ from its local minimum on the PES, before being optimised to a new local minimum as the system cools.[91] By repeating this, a large number of structures with different local minima will be obtained, of which the lowest energy structures are saved. More details about the conformer search calculations performed in *Chapter 4* are provided in *Section 4.2.2*.

Chapter 3

Hydrogen Bonding Interactions of Nucleobases with Multiply Charged Anions $[Pt(CN)_6]^{2-}$ and $[Pt(CN)_4]^{2-}$

3.1 Introduction

Cancer is one of the leading causes of death in the developed world and its treatment has become one of the most important subjects in a range of scientific fields. Currently, the most effective methods of treatment include surgery, radiotherapy and chemotherapy.[92] Chemotherapy utilises cytotoxic compounds to destroy the cancer cells.[93] An early success in chemotherapy was cisplatin, $Pt(NH_3)_2Cl_2$, which binds to DNA, linking the two strands and thereby interfering with the process of DNA replication, killing the cell.[94-96] The downside of cisplatin (as well as many other anticancer drugs), is that it is poorly selective for cancer cells and therefore has severe side effects as non-cancerous cells are killed.[96, 97] It is therefore of great importance to develop new and more selective anticancer drugs.

While the cytotoxic activity of cisplatin is a complex process, a fundamental understanding of the cisplatin-nucleic acid interactions in simple model systems are useful to inform future drug development and also to provide benchmark experiments for improving computational tools used to study such systems. Such model systems can be probed using tandem mass spectrometry to provide a range of information regarding the mechanism by which the interaction occurs.[98-103]

This chapter describes the hydrogen bonding interactions of the nucleobases adenine, cytosine, thymine and uracil with multiply charged anions (MCAs) $[Pt(CN)_6]^{2-}$ and $[Pt(CN)_4]^{2-}$. The intermolecular interactions are probed using low energy collision induced dissociation in a quadrupole ion trap, the results of which are supported by density functional theory calculations. While there is a significant amount of work investigating the microsolvation of MCAs with solvent molecules,[104-111] the information available for similar systems, in which an MCA is solvated by larger organic molecules is much more limited. The work presented in this chapter therefore provides new information regarding the hydrogen bonding interactions of MCAs.

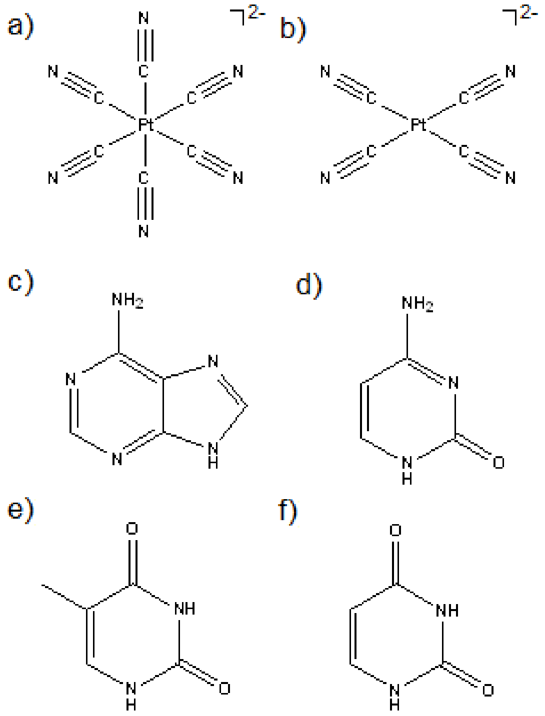

Figure 3.1: Chemical structures of the species used in this chapter. a) Platinum hexacyanide dianion (O_h), b) platinum tetracyanide dianion (D_{4h}), c) adenine, d) cytosine, e) thymine, f) uracil.

3.2 Experimental

3.2.1 Experimental Methods

Experiments were performed using a Bruker Esquire 6000 Quadrupole Ion Trap mass spectrometer equipped with an electrospray ionisation ion source and run in negative ion mode, as described in *Chapter 2*. The ion signal was optimised using the automatic tuning function of the spectrometer, with an injection rate of 2.0 µL min^{-1}, nebulising gas pressure of 10.0 psi, drying flow rate of 8.0 L min^{-1}, source temperature of 100˚C and ion excitation time of 40 ms. All spectra were averaged for 30 seconds, from m/z 50-600 with a resolution of m/z 0.35 (FWHM). Fragment spectra were obtained using the manual CID function of the spectrometer, with an isolation window of m/z 1.0-4.0 and CID energy values quoted as a percentage of the maximum resonance excitation voltage (100% = 2.50 V).

The investigated clusters were produced by electrospraying solutions of the platinum cyanide precursor and the nucleobase, both at 1×10^{-3} mol dm^{-3} in deionised water. $K_2Pt(CN)_4$ was used as a precursor for the $[Pt(CN)_4]^{2-}$ ion and $K_2Pt(CN)_6$ was used as a precursor for the $[Pt(CN)_6]^{2-}$ ion. All chemicals were purchased from Sigma-Aldrich and were used as provided, with no additional purification.

All spectra are presented with their intensities normalised, such that the most intense signal has an intensity of 100%. This allows for easy comparison between fragmentation spectra, even where the absolute intensity of the parent ions varies considerably. CID curves were obtained by plotting the relative intensities of the signals in the fragmentation mass spectra relating to the parent and fragment ions against fragmentation energy, in steps of 0.4%. Typical experimental errors (obtained from repeat runs) were ±3%. $E_{1/2}$ values were obtained by taking the energy at which the relative intensity of the precursor ion signal reaches 50%.

3.2.2 Computational Details

Structure optimisation and frequency calculations were performed using density functional theory methods with the B3LYP exchange and correlation functional[86] and the LANL2DZ basis set[112-115] using Gaussian 09.[116] Structure optimisation calculations were performed, along with frequency calculations on the optimised structures to ensure that there are no negative frequencies and that the optimised structure is a true minimum on the potential energy surface. The basis set used here has been used successfully to examine similar chemical systems[117, 118] and provides a good balance between computational cost and accuracy.

3.3 Results and Discussion

3.3.1 Platinum Hexacyanide Clusters

Figure 3.2 displays the negative ion electrospray ionisation (ESI) mass spectra of solutions of potassium platinum hexacyanide ($K_2Pt(CN)_6$) with the nucleobases adenine (Ad), cytosine (Cy), thymine (Th) and uracil (Ur). While all of the spectra are dominated by the peak resulting from the platinum hexacyanide dianion, $[Pt(CN)_6]^{2-}$, peaks resulting from adducts of the nucleobases with dianionic platinum hexacyanide, $[Pt(CN)_6M_n]^{2-}$ (M = Ad, Cy, Th or Ur) are clearly visible. Guanine was not investigated due to its poor solubility in water, meaning that clusters with significant intensity could not be produced. As there are no vacant coordination sites on the platinum metal centre, the nucleobases are expected to complex to the dianion by forming hydrogen bonds to the cyanide ligands.

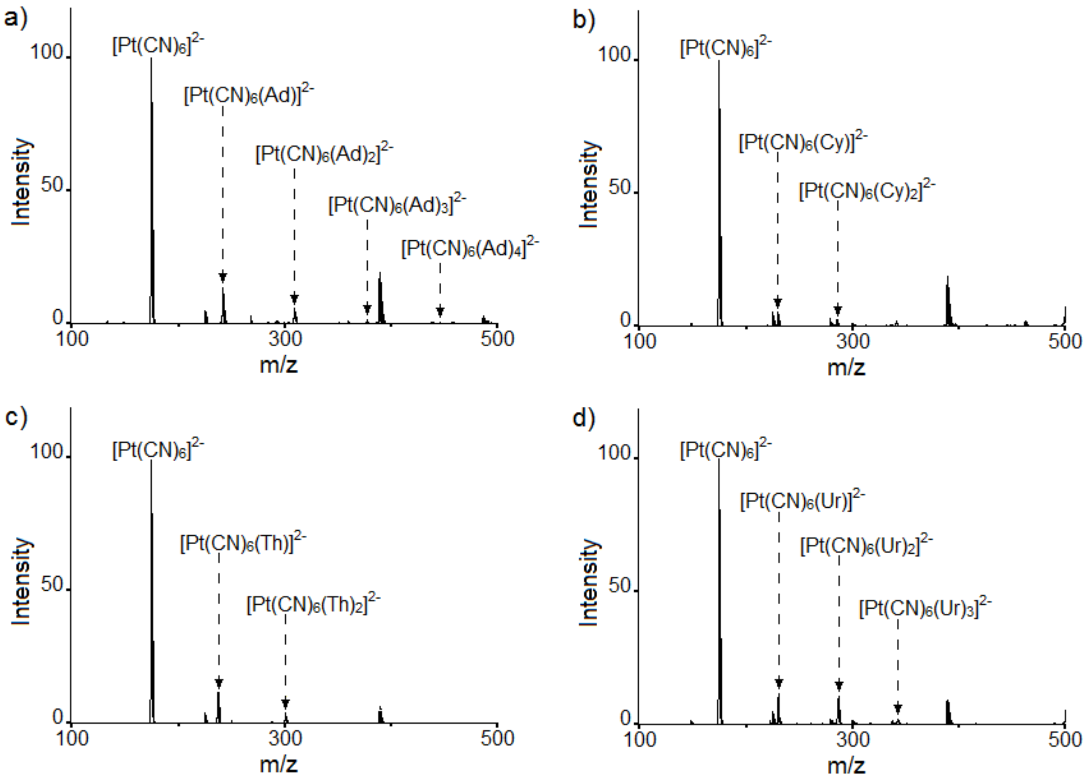

Figure 3.2: Negative ion mass spectra for mixtures of potassium platinum hexacyanide with a) adenine, b) cytosine, c) thymine d) uracil.

Fragmentation spectra of the clusters were obtained by isolation of the ions and fragmentation using resonance excitation. Upon isolation of the clusters, small fragment peaks (< 1%) can be seen in the mass spectra, indicating that these speciesare metastable.[119] In all cases, these metastable fragmentation products are the same as those obtained by fragmentation of the ions with resonance excitation. *Figure 3.3* displays the fragment spectra of the clusters containing platinum hexacyanide and a single nucleobase, $[Pt(CN)_6M]^{2-}$. For each of the nucleobases, there is only one fragmentation channel observed, which involves the dissociation of a neutral nucleobase from the cluster, leaving the bare $[Pt(CN)_6]^{2-}$ dianion (3.1).

$$[Pt(CN)_6M]^{2-} \rightarrow [Pt(CN)_6]^{2-} + M \qquad (3.1)$$

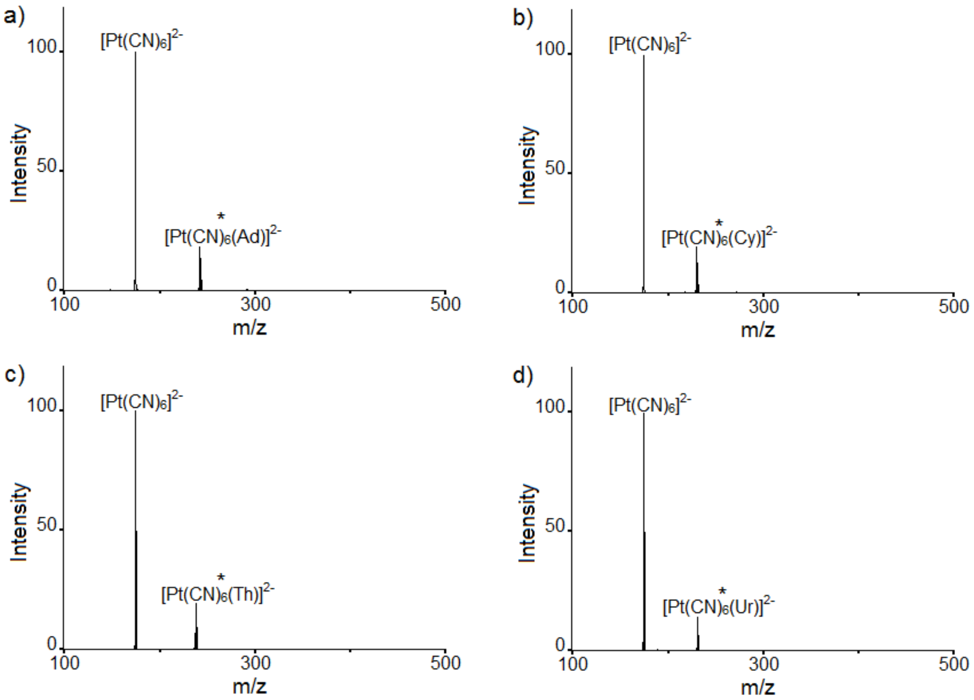

Figure 3.3: Negative ion fragmentation mass spectra of $[Pt(CN)_6(M)]^{2-}$, for a) M = Ad at 6.4%, b) M = Cy at 4.8%, c) M = Th at 4.4% d) M = Ur at 4.8%. Precursor ions are marked with *.

The clusters with two nucleobases, $[Pt(CN)_6M_2]^{2-}$, primarily fragment in the same way as those with one nucleobase (*Figure 3.4*), by the neutral dissociation of a single nucleobase to produce $[Pt(CN)_6M]^{2-}$ (3.2a). At higher collision energies, a second peak, corresponding to the bare $[Pt(CN)_6]^{2-}$ ion is also observed (3.2b). This fragmentation pathway could occur through two mechanisms: either both nucleobases dissociate simultaneously, or one nucleobase dissociates through pathway 3.2a to form $[Pt(CN)_6M]^{2-}$, which undergoes a secondary fragmentation to form $[Pt(CN)_6]^{2-}$.

$$[Pt(CN)_6M_2]^{2-} \rightarrow [Pt(CN)_6M]^{2-} + M \qquad (3.2a)$$

$$[Pt(CN)_6M_2]^{2-} \rightarrow [Pt(CN)_6]^{2-} + 2\ M \qquad (3.2b)$$

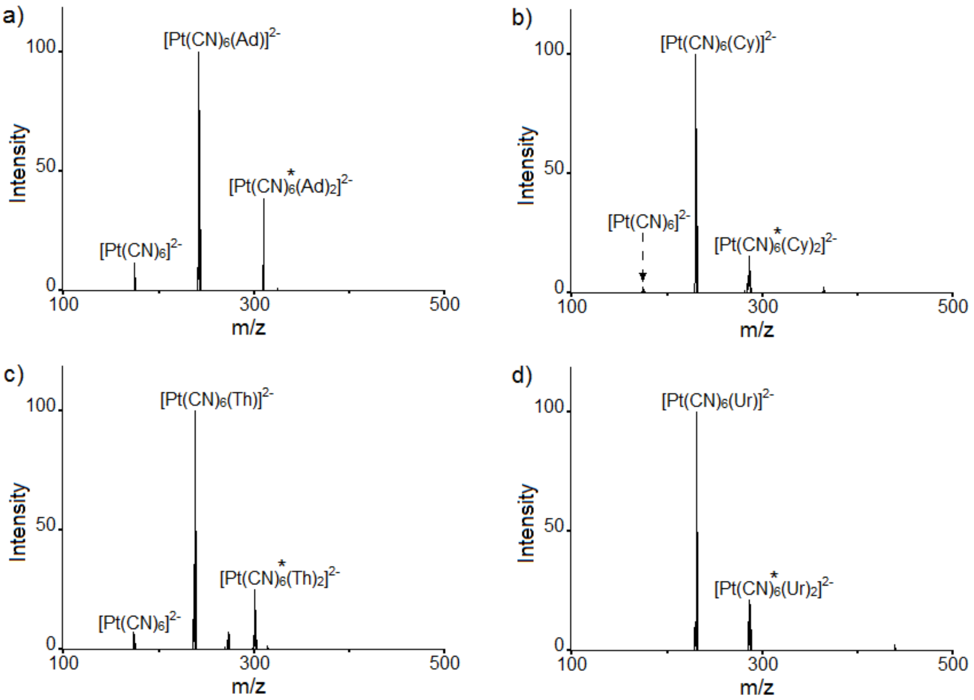

Figure 3.4: Negative ion fragmentation mass spectra of $[Pt(CN)_6(M)_2]^{2-}$, for a) M = Ad at 6.0%, b) M = Cy at 4.0%, c) M = Th at 4.4% d) M = Ur at 4.4%. Precursor ions are marked with *.

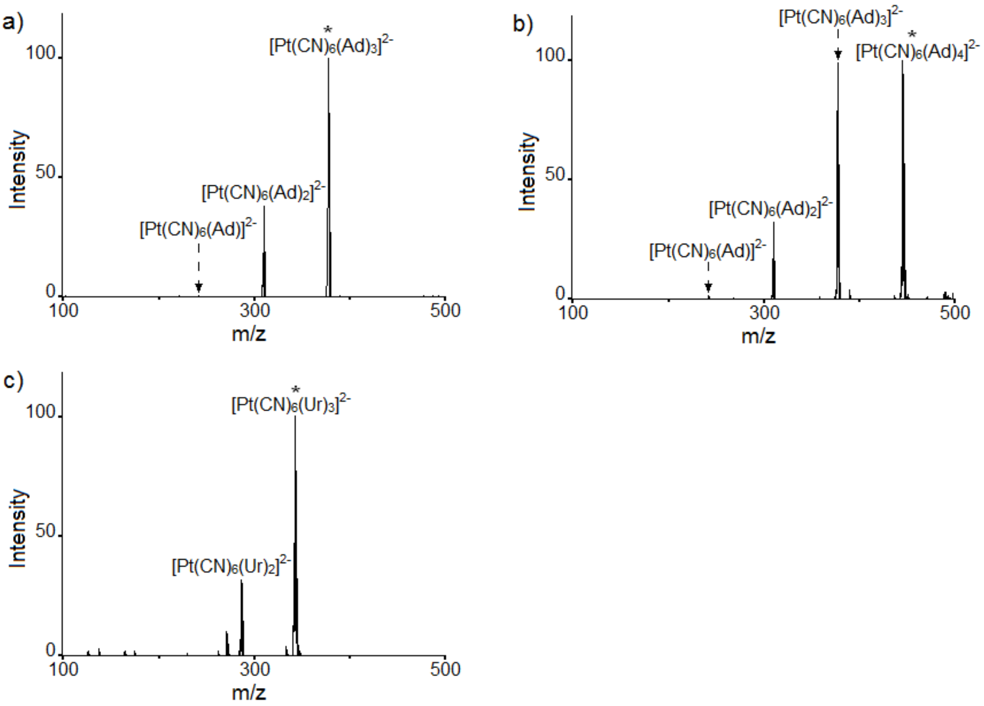

Figure 3.5: Negative ion fragmentation mass spectra of a) $[Pt(CN)_6(Ad)_3]^{2-}$ at 4.0%, b) $[Pt(CN)_6(Ad)_4]^{2-}$ at 4.0%, c) $[Pt(CN)_6(Ur)_3]^{2-}$ at 4.0%. Precursor ions are marked with *.

Clusters with three or more nucleobases also fragment in a similar manner (*Figure 3.5*). The most intense fragmentation pathway involves the loss of a single uncharged nucleobase (3.3a), with the loss of multiple nucleobases also observed as minor fragments at higher energies (3.3b and 3.3c).

$$[Pt(CN)_6M_n]^{2-} \rightarrow [Pt(CN)_6M_{(n-1)}]^{2-} + M \qquad (3.3a)$$

$$[Pt(CN)_6M_n]^{2-} \rightarrow [Pt(CN)_6M_{(n-2)}]^{2-} + 2\ M \qquad (3.3b)$$

$$[Pt(CN)_6M_n]^{2-} \rightarrow [Pt(CN)_6M_{(n-3)}]^{2-} + 3\ M \qquad (3.3c)$$

Table 3.1: Fragment ions for clusters $[Pt(CN)_6M_n]^{2-}$. M = Ad, Cy, Th, Ur; n = 1-4.

m/z	Precursor Ion	Product Ions
242.7	$[Pt(CN)_6(Ad)]^{2-}$	$[Pt(CN)_6]^{2-}$
310.2	$[Pt(CN)_6(Ad)_2]^{2-}$	$[Pt(CN)_6(Ad)]^{2-}$, $[Pt(CN)_6]^{2-}$
337.9	$[Pt(CN)_6(Ad)_3]^{2-}$	$[Pt(CN)_6(Ad)_2]^{2-}$, $[Pt(CN)_6(Ad)]^{2-}$
445.3	$[Pt(CN)_6(Ad)_4]^{2-}$	$[Pt(CN)_6(Ad)_3]^{2-}$, $[Pt(CN)_6(Ad)_2]^{2-}$, $[Pt(CN)_6(Ad)]^{2-}$
230.6	$[Pt(CN)_6(Cy)]^{2-}$	$[Pt(CN)_6]^{2-}$
286.2	$[Pt(CN)_6(Cy)_2]^{2-}$	$[Pt(CN)_6(Cy)]^{2-}$, $[Pt(CN)_6]^{2-}$
238.2	$[Pt(CN)_6(Th)]^{2-}$	$[Pt(CN)_6]^{2-}$
301.2	$[Pt(CN)_6(Th)_2]^{2-}$	$[Pt(CN)_6(Th)]^{2-}$, $[Pt(CN)_6]^{2-}$
231.1	$[Pt(CN)_6(Ur)]^{2-}$	$[Pt(CN)_6]^{2-}$
287.2	$[Pt(CN)_6(Ur)_2]^{2-}$	$[Pt(CN)_6(Ur)]^{2-}$, $[Pt(CN)_6]^{2-}$
343.2	$[Pt(CN)_6(Ur)_3]^{2-}$	$[Pt(CN)_6(Ur)_2]^{2-}$

There are two possible arrangements for the clusters when two nucleobases are present (*Figure 3.6*). Either each nucleobase will form a hydrogen bond to a separate cyanide ligand and they will bind separately, or the nucleobases will hydrogen bond together to form a base-pair, of which one of the nucleobases will form a hydrogen bond to one of the cyanide ligands. Both are plausible, although the structure in which nucleobases are binding separately seems more likely. Due to the unsolvated double negative charge, the platinum complex is unstable in the gas phase,[120] but hydrogen bonds from the nucleobases can help to solvate the complex, increasing its stability.[104, 121, 122] If the nucleobases were binding separately, they would form more hydrogen bonds to the platinum hexacyanide dianion, better solvating the charge and therefore making the structure more stable. This will be discussed further in *Section 3.3.4*.

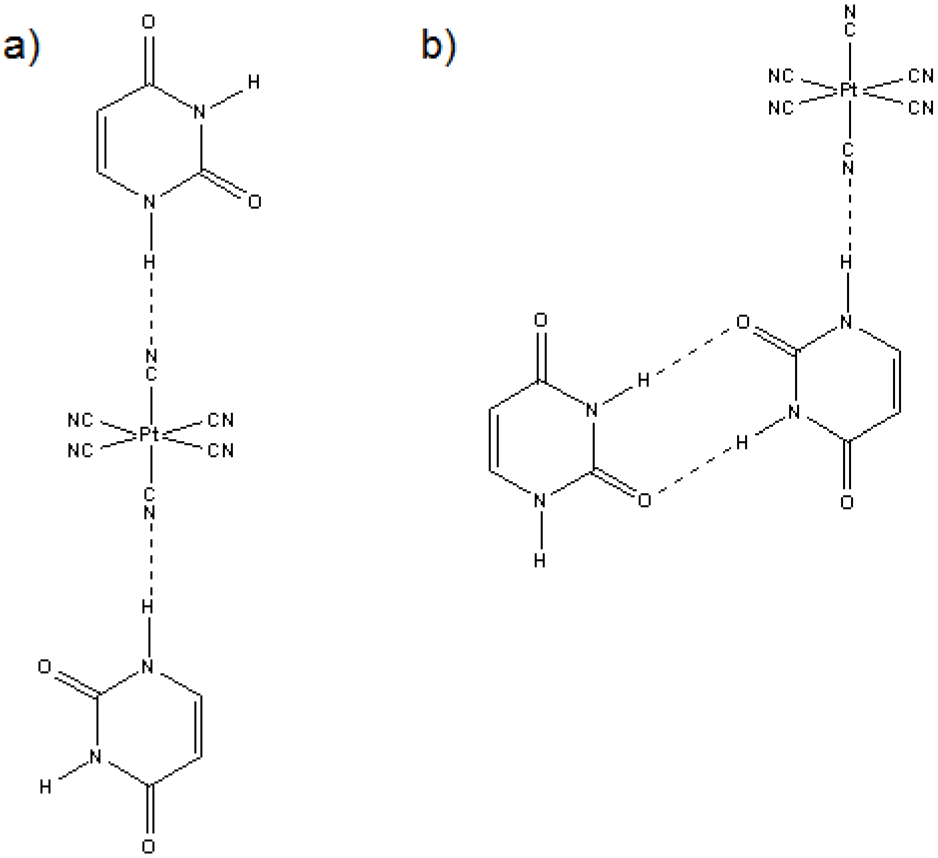

Figure 3.6: Potential structures for the $[Pt(CN)_6(Ur)_2]^{2-}$ cluster, with a) the nucleobases complexing separately to different cyanide ligands, b) with the nucleobases complexing as a base pair to a single cyanide ligand.

3.3.2 Platinum Tetracyanide Clusters

Figure 3.7 shows the ESI mass spectra of a set of analogous mixtures of adenine, cytosine, thymine and uracil with potassium platinum tetracyanide, ($K_2Pt(CN)_4$). The spectra resemble those of the platinum hexacyanide mixtures, with the mass spectra dominated by the platinum tetracyanide dianion, $[Pt(CN)_4]^{2-}$, and smaller peaks attributable to nucleobase adduct clusters, $[Pt(CN)_4M_n]^{2-}$ also visible.

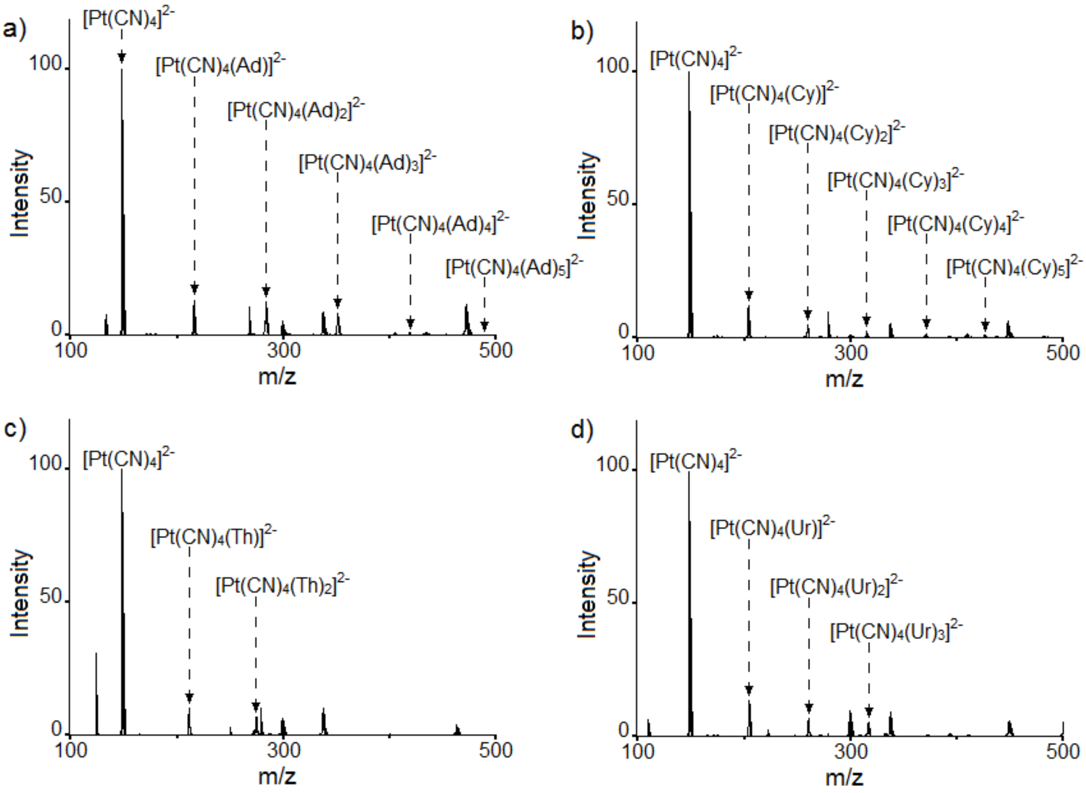

Figure 3.7: Negative ion mass spectra for mixtures of potassium platinum tetracyanide with a) adenine, b) cytosine, c) thymine d) uracil.

Platinum tetracyanide takes a square planar geometry,[123, 124] meaning that unlike platinum hexacyanide, it has a vacant site within the primary coordination sphere. This means that it is possible for the nucleobases to coordinate directly to the platinum centre through a nitrogen or oxygen atom, rather than hydrogen bonding to one of the cyanide ligands. However, direct coordination of the nucleobases seems unlikely, considering how the platinum complex is already unstable in the gas phase due to the high electron density, caused by the unsolvated double charge.[120] Coordination of the nucleobase would donate additional electron density to the platinum centre, further reducing the stability, while hydrogen bonding of the nucleobases to the cyanide ligands would lower the electron density of the complex.[104]

As with the hexacyanide clusters, small fragmentation peaks are observed upon isolation of the clusters, indicating that they are metastable.[119] While most of these metastable decay peaks are the same as the fragmentation peaks, $[Pt(CN)_3]^-$ is also observed. Upon fragmentation of the $[Pt(CN)_4M_n]^{2-}$ clusters, the intensity of the $[Pt(CN)_3]^-$ peak does not change significantly.

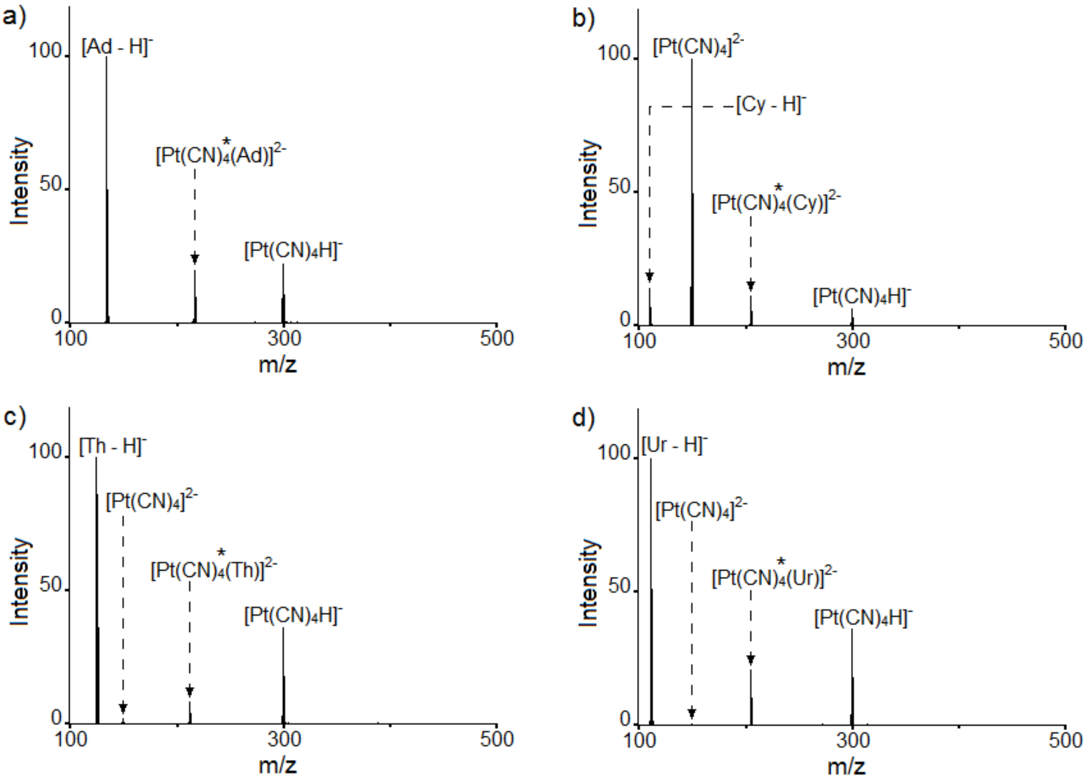

Figure 3.8: Negative ion fragmentation mass spectra of $[Pt(CN)_4(M)]^{2-}$, for a) M = Ad at 6.8%, b) M = Cy at 6.4%, c) M = Th at 6.4% d) M = Ur at 5.6%. Precursor ions are marked with *.

Upon resonance excitation, the clusters containing one nucleobase will fragment through two channels (*Figure 3.8*). The uncharged nucleobase can dissociate from the cluster, leaving the platinum tetracyanide dianion (3.4a) in an analogous manner to that observed for the platinum hexacyanide clusters. The second fragmentation channel involves deprotonation of the nucleobase, and protonation of the platinum complex, producing two monoanionic species (3.4b). The resulting isocyanide ligand (-CNH) has been well characterised.[125]

$$[Pt(CN)_4M]^{2-} \rightarrow [Pt(CN)_4]^{2-} + M \tag{3.4a}$$

$$[Pt(CN)_4M]^{2-} \rightarrow [Pt(CN)_4H]^{-} + [M - H]^{-} \tag{3.4b}$$

The clusters with different nucleobases will fragment through these two channels in different proportions. The clusters containing adenine, thymine and uracil fragment almost entirely through deprotonation, with signals corresponding to direct dissociation barely visible. On the other hand, the cluster containing cytosine fragments mostly through dissociation. The difference is most likely the result of the low acidity of cytosine, which has the highest gas-phase pk_a of the four nucleobases investigated,[126] meaning that deprotonation is extremely unfavourable compared to the other nucleobases.

The observation that the platinum tetracyanide clusters tend to fragment by deprotonation, while the hexacyanide clusters do not can be explained by the relative stabilities of the bare platinum cyanide ions. Both the platinum tetracyanide and hexacyanide complexes are dianionic, which means that they will be unstable in the gas phase.[120] $[Pt(CN)_6]^{2-}$ has the excess charge spread over thirteen atoms, whereas $[Pt(CN)_4]^{2-}$ has the charge spread over only nine atoms. This means that $[Pt(CN)_4]^{2-}$ will be more unstable and so, the barrier height for the direct dissociation pathway will be higher. Therefore, fragmentation will occur more readily through the deprotonation pathway.

The most intense fragmentation channel of the clusters containing two nucleobases (*Figure 3.9*) is the direct dissociation of a single nucleobase (3.5a). In addition to this, a signal for a deprotonated dimer of the nucleobase $[M_2 - H]^-$ is also observed (3.5b). This dimerization channel is not observed for the cytosine clusters, which can be attributed for the low acidity of cytosine.[126] For clusters with the remaining nucleobases, the dimerization channel is considerably more intense for adenine and uracil than for thymine. The significant difference between the clusters containing thymine and uracil is interesting, given the similarity of their structures. Signals can also be seen for the fragmentation products of the one-nucleobase clusters:

$[Pt(CN)_4H]^-$, $[Pt(CN)_4]^{2-}$ and $[M - H]^-$ (3.5c and 3.5d). These are most likely the result of secondary fragmentations of the clusters.

$$[Pt(CN)_4M_2]^{2-} \rightarrow [Pt(CN)_4M]^{2-} + M \tag{3.5a}$$

$$[Pt(CN)_4M_2]^{2-} \rightarrow [Pt(CN)_4H]^- + [M_2 - H]^- \tag{3.5b}$$

$$[Pt(CN)_4M_2]^{2-} \rightarrow [Pt(CN)_4]^{2-} + 2\ M \tag{3.5c}$$

$$[Pt(CN)_4M_2]^{2-} \rightarrow [Pt(CN)_4H]^- + [M - H]^- + M \tag{3.5d}$$

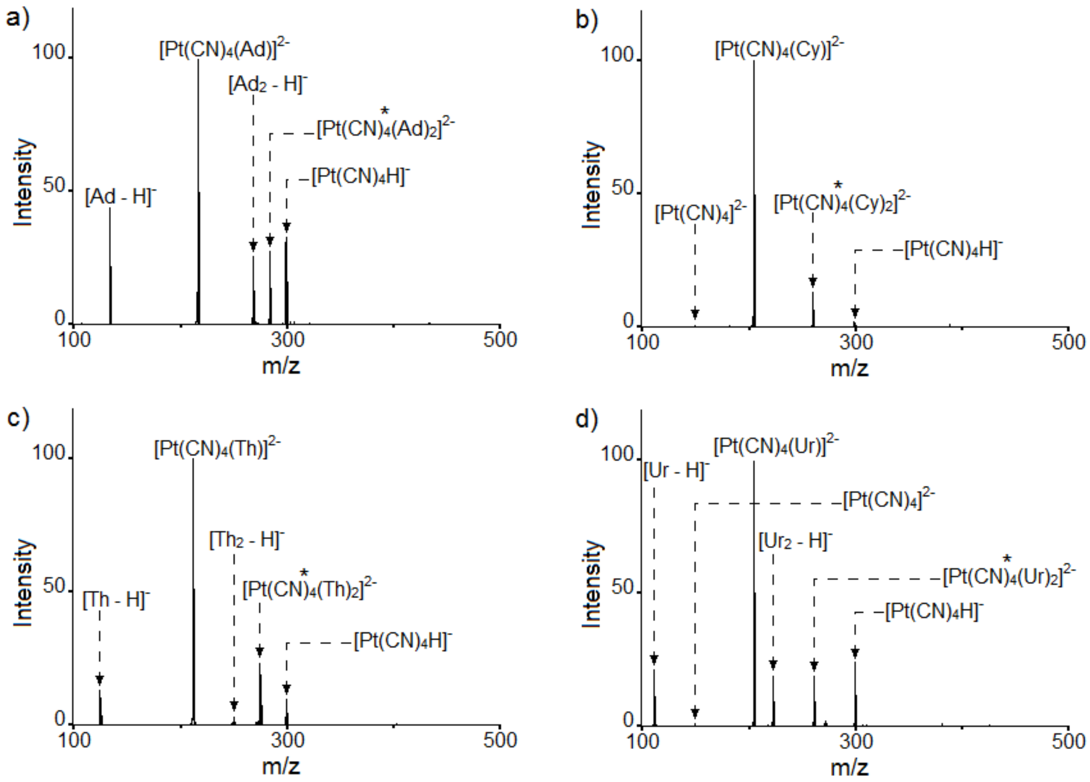

Figure 3.9: Negative ion fragmentation mass spectra of $[Pt(CN)_4(M)_2]^{2-}$, for a) M = Ad at 6.8%, b) M = Cy at 4.8%, c) M = Th at 5.6% d) M = Ur at 5.6%. Precursor ions are marked with *.

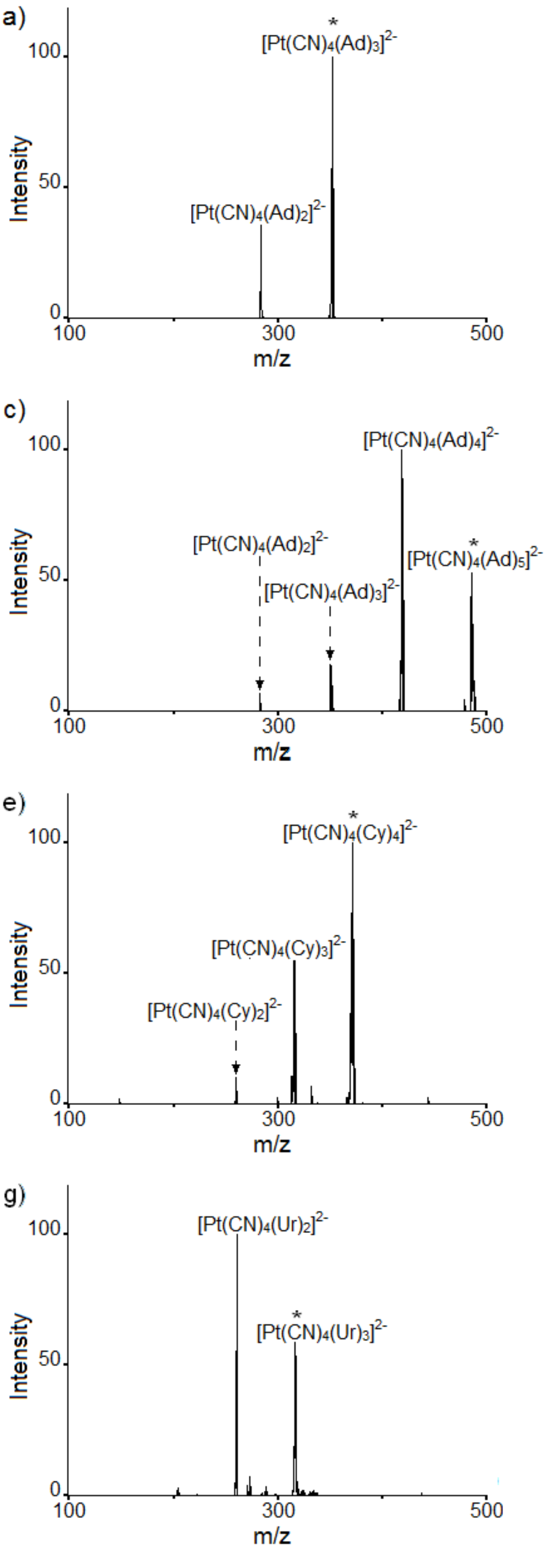

Figure 3.10: Negative ion fragmentation mass spectra of a) $[Pt(CN)_4(Ad)_3]^{2-}$ at 4.0%, b) $[Pt(CN)_4(Ad)_4]^{2-}$ at 4.0%, c) $[Pt(CN)_4(Ad)_5]^{2-}$ at 4.0%, d) $[Pt(CN)_4(Cy)_3]^{2-}$ at 4.0%, e) $[Pt(CN)_4(Cy)_4]^{2-}$ at 4.0%, f) $[Pt(CN)_4(Cy)_5]^{2-}$ at 3.2%, g) $[Pt(CN)_4(Ur)_3]^{2-}$ at 4.0%. Precursor ions are marked with *.

For the clusters of the platinum tetracyanide dianion with three or more nucleobases (*Figure 3.10*), no fragment ions are observed for the deprotonation or dimerization pathways, fragmentation is only observed to occur through dissociation (3.6). Smaller signals are also observed for secondary fragmentation of the ion formed by dissociation.

$$[Pt(CN)_4M_n]^{2-} \rightarrow [Pt(CN)_4M_{(n-1)}]^{2-} + M \qquad (3.6)$$

Table 3.2: Fragment ions for clusters $[Pt(CN)_4M_n]^{2-}$. M = Ad, Cy, Th, Ur; n = 1-5.

m/z	Precursor Ion	Product Ions
216.7	$[Pt(CN)_4(Ad)]^{2-}$	$[Pt(CN)_4H]^-$, $[Ad - H]^-$
284.2	$[Pt(CN)_4(Ad)_2]^{2-}$	$[Pt(CN)_4]^-$, $[Ad_2 - H]^-$, $[Pt(CN)_4(Ad)]^{2-}$, $[Ad - H]^-$
351.7	$[Pt(CN)_4(Ad)_3]^{2-}$	$[Pt(CN)_4]^-$, $[Pt(CN)_4(Ad)_2]^{2-}$, $[Pt(CN)_4(Ad)]^{2-}$, $[Ad - H]^-$
419.3	$[Pt(CN)_4(Ad)_4]^{2-}$	$[Pt(CN)_4(Ad)_3]^{2-}$, $[Pt(CN)_4(Ad)_2]^{2-}$, $[Pt(CN)_4(Ad)]^{2-}$
486.8	$[Pt(CN)_4(Ad)_5]^{2-}$	$[Pt(CN)_4(Ad)_4]^{2-}$, $[Pt(CN)_4(Ad)_3]^{2-}$, $[Pt(CN)_4(Ad)_2]^{2-}$
204.6	$[Pt(CN)_4(Cy)]^{2-}$	$[Pt(CN)_4H]^-$, $[Pt(CN)_4]^{2-}$, $[Cy - H]^-$
260.2	$[Pt(CN)_4(Cy)_2]^{2-}$	$[Pt(CN)_4H]^-$, $[Pt(CN)_4(Cy)]^{2-}$, $[Pt(CN)_4]^{2-}$, $[Cy - H]^-$
315.7	$[Pt(CN)_4(Cy)_3]^{2-}$	$[Pt(CN)_4(Cy)_2]^{2-}$, $[Pt(CN)_4(Cy)]^{2-}$, $[Pt(CN)_4]^{2-}$
371.3	$[Pt(CN)_4(Cy)_4]^{2-}$	$[Pt(CN)_4(Cy)_3]^{2-}$, $[Pt(CN)_4(Cy)_2]^{2-}$
426.8	$[Pt(CN)_4(Cy)_5]^{2-}$	$[Pt(CN)_4(Cy)_4]^{2-}$, $[Pt(CN)_4(Cy)_3]^{2-}$
212.1	$[Pt(CN)_4(Th)]^{2-}$	$[Pt(CN)_4H]^-$, $[Pt(CN)_4]^{2-}$, $[Th - H]^-$
275.2	$[Pt(CN)_4(Th)_2]^{2-}$	$[Pt(CN)_4H]^-$, $[Th_2 - H]^-$, $[Pt(CN)_4(Th)]^{2-}$, $[Th - H]^-$
205.1	$[Pt(CN)_4(Ur)]^{2-}$	$[Pt(CN)_4H]^-$, $[Pt(CN)_4]^{2-}$, $[Ur - H]^-$
261.2	$[Pt(CN)_4(Ur)_2]^{2-}$	$[Pt(CN)_4H]^-$, $[Ur_2 - H]^-$, $[Pt(CN)_4(Ur)]^{2-}$, $[Ur - H]^-$
317.2	$[Pt(CN)_4(Ur)_3]^{2-}$	$[Pt(CN)_4(Ur)_2]^{2-}$

These results show that for the clusters of platinum tetracyanide with nucleobases, as the number of nucleobases increases, the fragmentation channels relating to deprotonation of the nucleobase decrease in intensity. This can be explained by considering the stability of the clusters. Clusters with more nucleobases will have the double charge on the platinum complex solvated more effectively than those with only one or two nucleobases. This means that the barrier height for the dissociation pathway will decrease as the number of solvating nucleobases increases and so, it will become more favoured over the deprotonation channels.

$[Pt(CN)_4(Ad)_2]^{2-}$ has a number of anomalous properties in its fragmentation spectrum. The metastable fragmentation peaks are significantly more intense than any of the other clusters investigated, with the cluster decaying to form $[Pt(CN)_4H]^-$, but notably not $[Ad - H]^-$ or $[Ad_2 - H]^-$, which should also be formed. Despite the fact that the ^{195}Pt isotopomer was exclusively selected during the isolation stage, $[Pt(CN)_4H]^-$ was observed to form in both its ^{194}Pt and ^{195}Pt isotopormers (MS^3 fragmentation of each of these peaks individually results in the loss of a mass of 27, consistent with HCN, confirming that these peaks are both $[Pt(CN)_4H]^-$, and that one is not $[Pt(CN)_4]^-$). The most likely explanation for this is that there is a second species which overlaps with $[Pt(CN)_4(Ad)_2]^{2-}$ in the mass spectrum. While this species has not been successfully identified, some information can be obtained. As the ^{194}Pt isotopomer of the unknown species is isolated alongside the ^{195}Pt isotopomer of $[Pt(CN)_4(Ad)_2]^{2-}$, it can be inferred that the *m/z* ratio of the unknown species is 0.5 higher than $[Pt(CN)_4(Ad)_2]^{2-}$. As $[Pt(CN)_4H]^-$ is formed upon fragmentation, it can be inferred that the species is an aggregation of $[Pt(CN)_4]^{2-}$ and a protic molecule with mass of 273 g mol^{-1} (1 g mol^{-1} heavier than 2 Ad).

3.3.3 Comparisons of Fragmentation Energies

By plotting the relative intensities of the precursor and fragment ions as the collision energy is varied, a CID curve can be created. By comparing the collision energy at which the relative intensity of the precursor ion reaches 50% (hereafter referred to as $E_{1/2}$), the relative barrier heights for fragmentation of the clusters can be directly compared.[82] Only platinum hexacyanide clusters with one and two nucleobases could be isolated with sufficient intensity to allow for reliable CID curves to be plotted. The platinum tetracyanide clusters could be isolated reliably with up to two nucleobases for cytosine, thymine and uracil, and up to three nucleobases for adenine. CID curves are given for the platinum hexacyanide clusters in *Figures 3.11-3.14* and for the platinum tetracyanide clusters in *Figures 3.15-3.18*. The values of $E_{1/2}$ are summarised in *Table 3.3*. It is important to note that the difference in *m/z* between $[Pt(CN)_4(Ad)_3]^{2-}$ and the one-nucleobase clusters is greater than 100, meaning that the values of $E_{1/2}$ should not be compared directly in these cases (see *Section 2.1.4*).[84] All of the other clusters are within the *m/z* 100 limit of each other, and so can be compared directly.

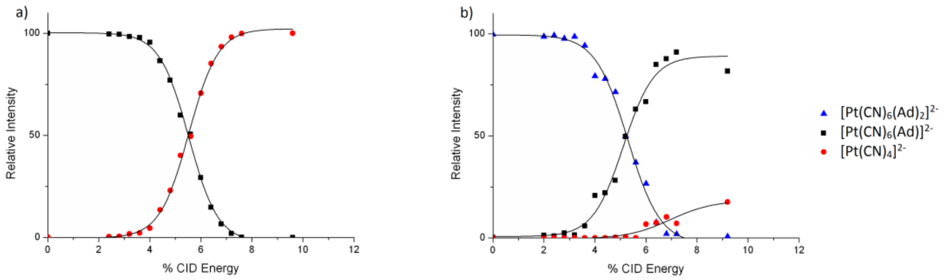

Figure 3.11: %CID curves for $[Pt(CN)_6(Ad)_n]^{2-}$, where a) $n = 1$, b) $n = 2$.

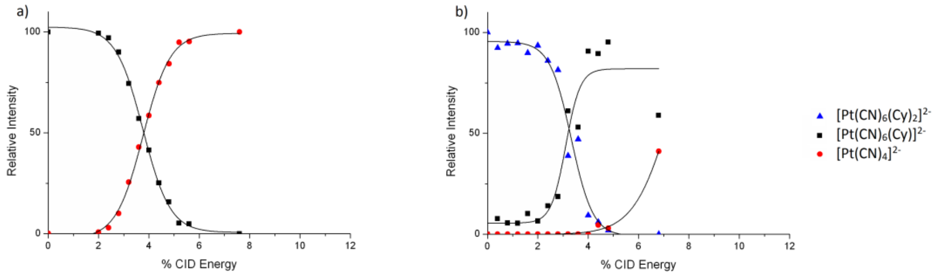

Figure 3.12: %CID curves for $[Pt(CN)_6(Cy)_n]^{2-}$, where a) $n = 1$, b) $n = 2$.

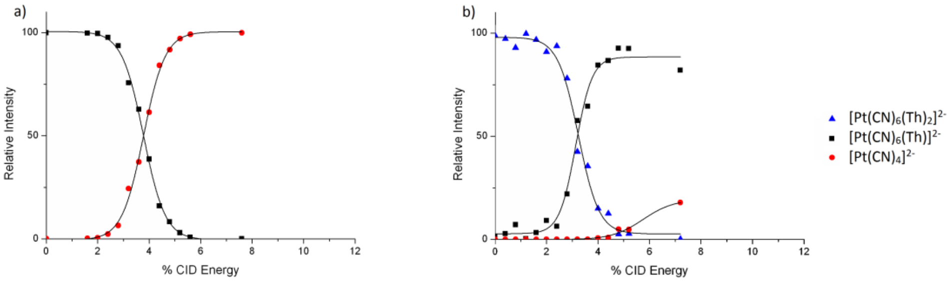

Figure 3.13: %CID curves for $[Pt(CN)_6(Th)_n]^{2-}$, where a) $n = 1$, b) $n = 2$.

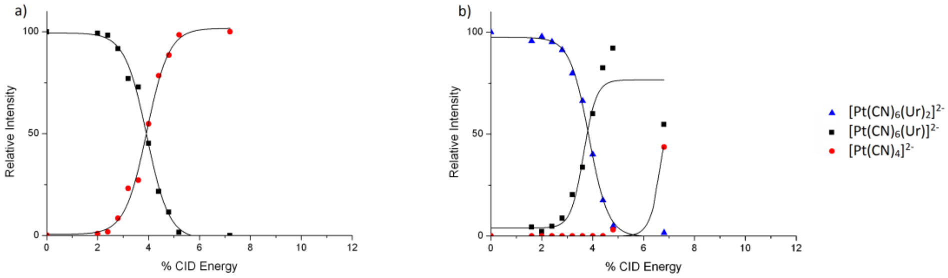

Figure 3.14: %CID curves for $[Pt(CN)_6(Ur)_n]^{2-}$, where a) $n = 1$, b) $n = 2$.

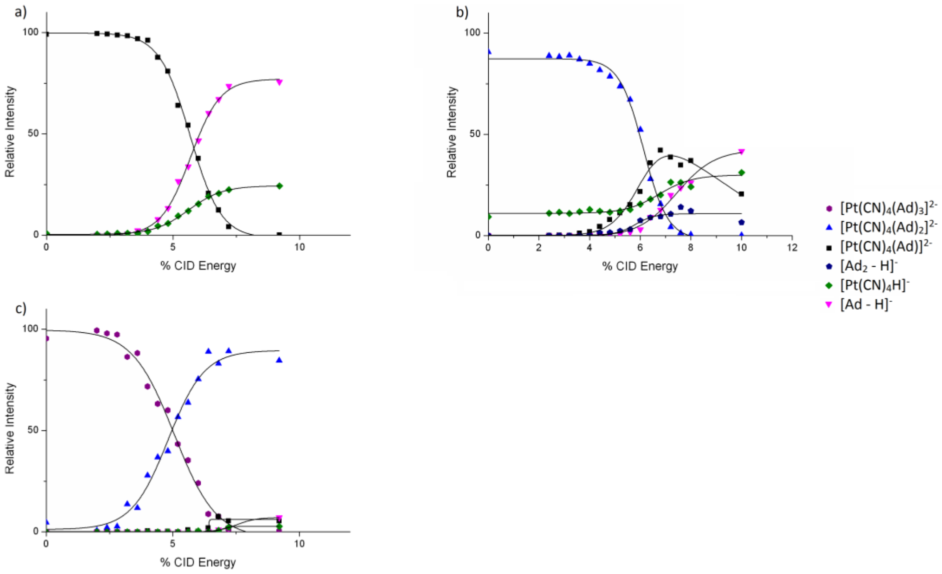

Figure 3.15: %CID curves for $[Pt(CN)_4(Ad)_n]^{2-}$, where a) $n = 1$, b) $n = 2$, c) $n = 3$.

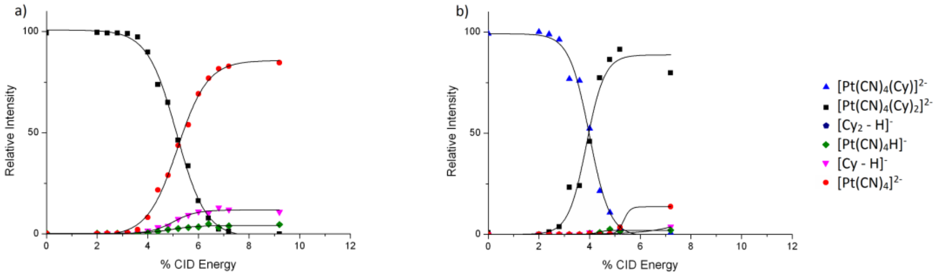

Figure 3.16: %CID curves for $[Pt(CN)_4(Cy)_n]^{2-}$, where a) $n = 1$, b) $n = 2$.

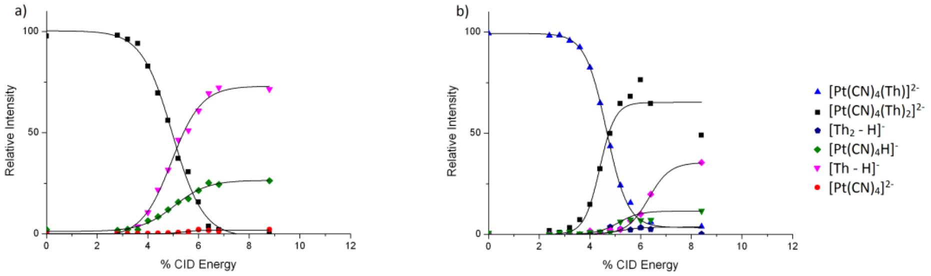

Figure 3.17: %CID curves for $[Pt(CN)_4(Th)_n]^{2-}$, where a) $n = 1$, b) $n = 2$.

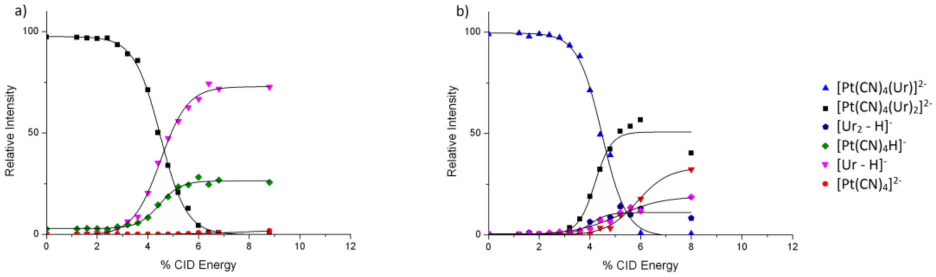

Figure 3.18: %CID curves for $[Pt(CN)_4(Ur)_n]^{2-}$, where a) $n = 1$, b) $n = 2$.

For both the platinum tetracyanide and hexacyanide clusters with all four of the nucleobases, $E_{1/2}$ was found to be higher for the clusters with one nucleobase compared those with two nucleobases, with one exception. These results are consistent with the structure postulated in *Section 3.3.1*, in which the two nucleobases are complexing to the dianion separately. Hydrogen bonds to the cyanide ligands will reduce the electron density of the platinum complex and if there are hydrogen bonds from multiple nucleobases, the charge will be solvated more than if it were a single nucleobase.[104, 122] This solvation will result in weaker electrostatic interactions in the hydrogen bonds, meaning that less energy is required to overcome the barrier to break the bonds. Additionally, it is possible that there is a steric effect, as the two nucleobases in the cluster will interact with each other to some degree. This interaction will prevent the nucleobases from binding in an optimal position, resulting in weaker hydrogen bonds.

Table 3.3: $E_{1/2}$ fragmentation energies for clusters $[Pt(CN)_mM_n]^{2-}$. M = Ad, Cy, Th, Ur; m = 4, 6; n = 1, 2, 3.

	Adenine	**Cytosine**	**Thymine**	**Uracil**
$[Pt(CN)_6M]^{2-}$	5.6%	3.8%	3.8%	3.9%
$[Pt(CN)_6M_2]^{2-}$	5.2%	3.6%	3.1%	3.8%
$[Pt(CN)_4M]^{2-}$	5.7%	5.1%	4.9%	4.8%
$[Pt(CN)_4M_2]^{2-}$	6.0%	4.0%	4.7%	4.4%
$[Pt(CN)_4M_3]^{2-}$	5.0%	-	-	-

The previously mentioned exception to the trend is $[Pt(CN)_4(Ad)_2]^{2-}$, which fragments at a higher collision energy that its one-adenine analogue. As was discussed in *Section 3.3.2*, it appears that there is an unknown species overlapping $[Pt(CN)_4(Ad)_2]^{2-}$ in the mass spectrum, which may well be the cause of the anomalous $E_{1/2}$ value. $[Pt(CN)_4(Ad)_3]^{2-}$ was found to fragment at a significantly lower energy than either the one- or two-adenine clusters, indicating that it is only the two-adenine cluster that is anomalous in this regard.

The $E_{1/2}$ values for the platinum tetracyanide clusters are higher than those of the equivalent platinum hexacyanide clusters in all cases. As with several of the other trends observed, this can be explained by considering the electron density on the platinum cyanide dianion. Both the platinum tetracyanide and hexacyanide clusters are dianionic and the excess charge will be mostly distributed across the cyanide ligands. As platinum tetracyanide has fewer ligands, each ligand will carry a larger portion of the excess charge, resulting in stronger electrostatic interactions between the cyanide ligand and the hydrogen of the nucleobase.

3.3.4 Computational Results

A number of density functional theory (DFT) calculations were conducted using the B3LYP/LANL2DZ basis set[112-115] to support the experimental results. To begin, clusters with a single nucleobase were investigated. *Figures 3.19-3.22* display the optimised structures of the clusters containing one nucleobase with $[Pt(CN)_6]^{2-}$ and *Figures 3.23-3.26* display the optimised structures for the clusters with $[Pt(CN)_4]^{2-}$. For each nucleobase, two low energy structures are obtained, which are almost identical in both the clusters with $[Pt(CN)_6]^{2-}$ and $[Pt(CN)_4]^{2-}$, and are labelled as **I** and **II** for the lowest and second lowest energy structures respectively.

It is interesting to observe that all of the $[Pt(CN)_4]^{2-}$ clusters are planar, with the exception of structure **II** for the thymine and uracil clusters, which have the nucleobase twisted perpendicular to the dianion. This is most likely caused by the two carbonyl groups on the nucleobases, which if the nucleobase was planar, would come in close contact with two of the cyanide groups of the dianion. As both the carbonyl groups and cyanide ligands are highly electronegative, the resulting electrostatic repulsions would be extremely unfavourable, and so the cluster takes a twisted structure, such that the carbonyl groups are pointing away from the cyanide ligands.

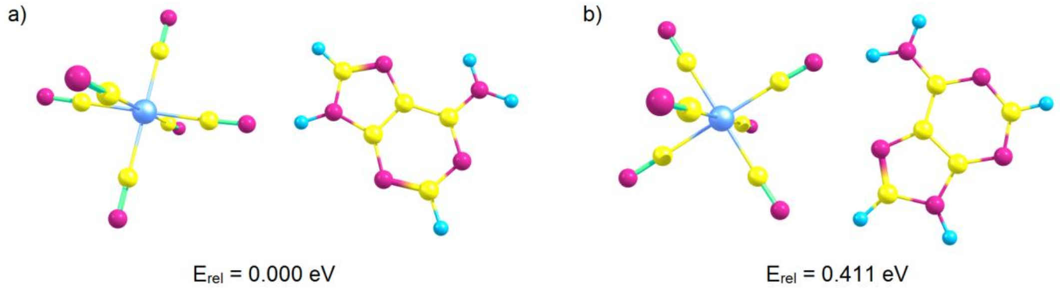

Figure 3.19: Low energy structures of $[Pt(CN)_6(Ad)]^{2-}$, a) structure **I**, b) structure **II**. Relative energies are displayed in the figure.

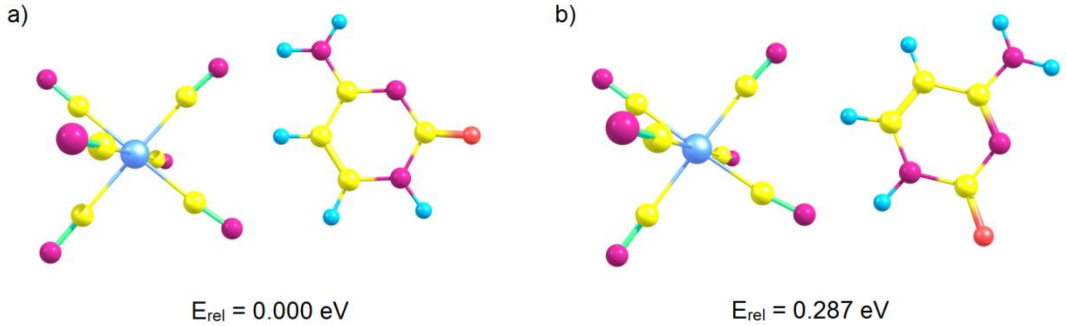

Figure 3.20: Low energy structures of $[Pt(CN)_6(Cy)]^{2-}$, a) structure **I**, b) structure **II**. Relative energies are displayed in the figure.

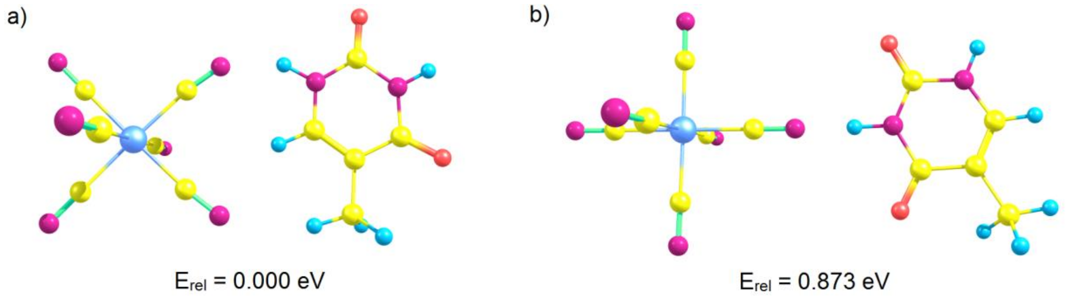

Figure 3.21: Low energy structures of $[Pt(CN)_6(Th)]^{2-}$, a) structure **I**, b) structure **II**. Relative energies are displayed in the figure.

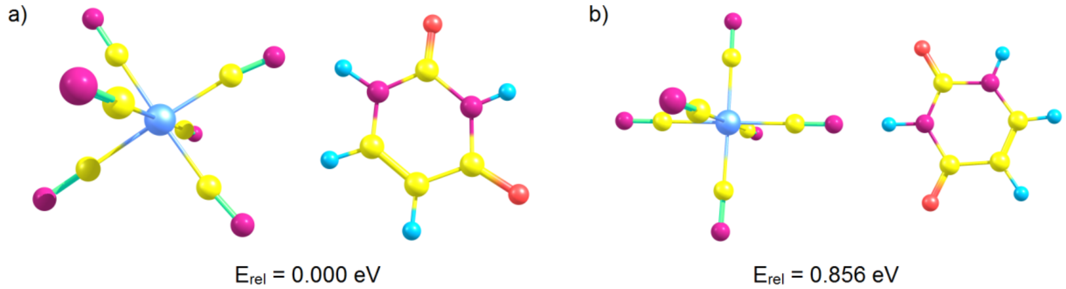

Figure 3.22: Low energy structures of $[Pt(CN)_6(Ur)]^{2-}$, a) structure **I**, b) structure **II**. Relative energies are displayed in the figure.

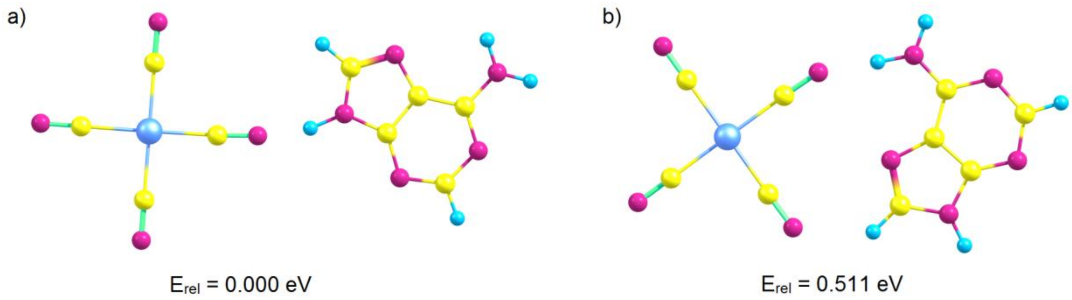

Figure 3.23: Low energy structures of $[Pt(CN)_4(Ad)]^{2-}$, a) structure **I**, b) structure **II**. Relative energies are displayed in the figure.

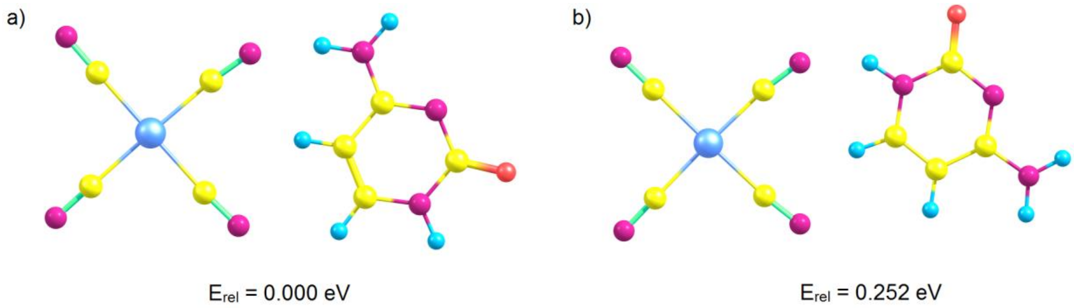

Figure 3.24: Low energy structures of $[Pt(CN)_4(Cy)]^{2-}$, a) structure **I**, b) structure **II**. Relative energies are displayed in the figure.

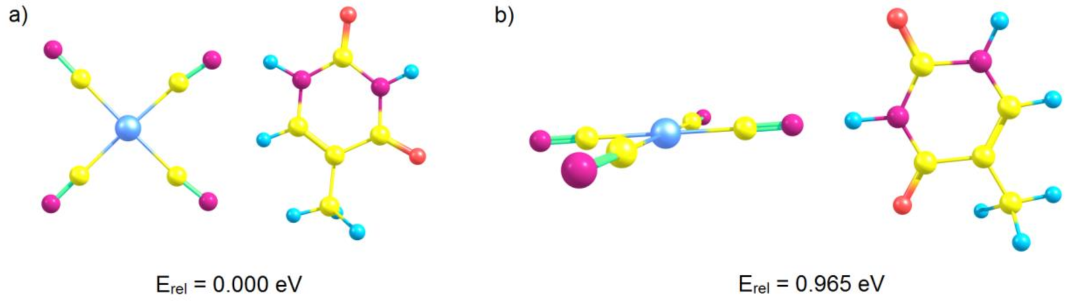

Figure 3.25: Low energy structures of $[Pt(CN)_4(Th)]^{2-}$, a) structure **I**, b) structure **II**. Relative energies are displayed in the figure.

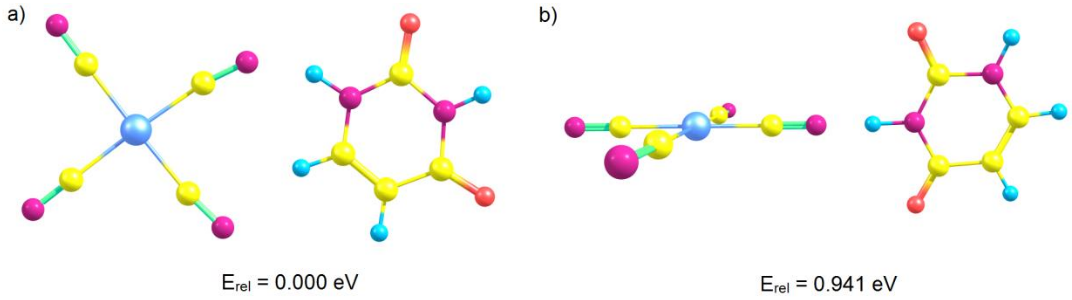

Figure 3.26: Low energy structures of $[Pt(CN)_4(Ur)]^{2-}$, a) structure **I**, b) structure **II**. Relative energies are displayed in the figure.

In addition to the structures displayed, $[Pt(CN)_4]^{2-}$ clusters with the nucleobase coordinating directly to the platinum centre through a heteroatom were investigated. In all cases, no local minima could be identified, confirming that these are unstable structures, as was postulated in *Section 3.3.2*.

The relative abundances of each of the structures can be determined using the Boltzmann distribution equation:[127]

$$\frac{N_i}{\sum N_i} = \frac{g_i\, e^{-E_i/\, k_B T}}{Z(T)} \tag{3.7}$$

Where k_B is the Boltzmann constant, T is the temperature (assumed to be the source temperature, 373 K), g_i is the degeneracy (assumed to be 1 for each structure) and Z(T) is the partition function:

$$Z(T) = \sum g_i\, e^{-E_i/k_B T} \tag{3.8}$$

The results, displayed in *Tables 3.4 and 3.5*, indicate that for all nucleobases, it is only structure **I** that is present under the conditions of the ion trap.

Table 3.4: Relative energies and abundances of structures of the clusters $[Pt(CN)_6M]^{2-}$.

Nucleobase	**Relative Energy, E_{rel} / eV**		**Relative Abundance**	
	Structure **I**	Structure **II**	Structure **I**	Structure **II**
Adenine	0	0.411	100.0%	0.0%
Cytosine	0	0.287	100.0%	0.0%
Thymine	0	0.873	100.0%	0.0%
Uracil	0	0.856	100.0%	0.0%

Table 3.5: Relative energies and abundances of structures of the clusters $[Pt(CN)_4M]^{2-}$.

Nucleobase	**Relative Energy, E_{rel} / eV**		**Relative Abundance**	
	Structure **I**	Structure **II**	Structure **I**	Structure **II**
Adenine	0	0.511	100.0%	0.0%
Cytosine	0	0.252	100.0%	0.0%
Thymine	0	0.965	100.0%	0.0%
Uracil	0	0.941	100.0%	0.0%

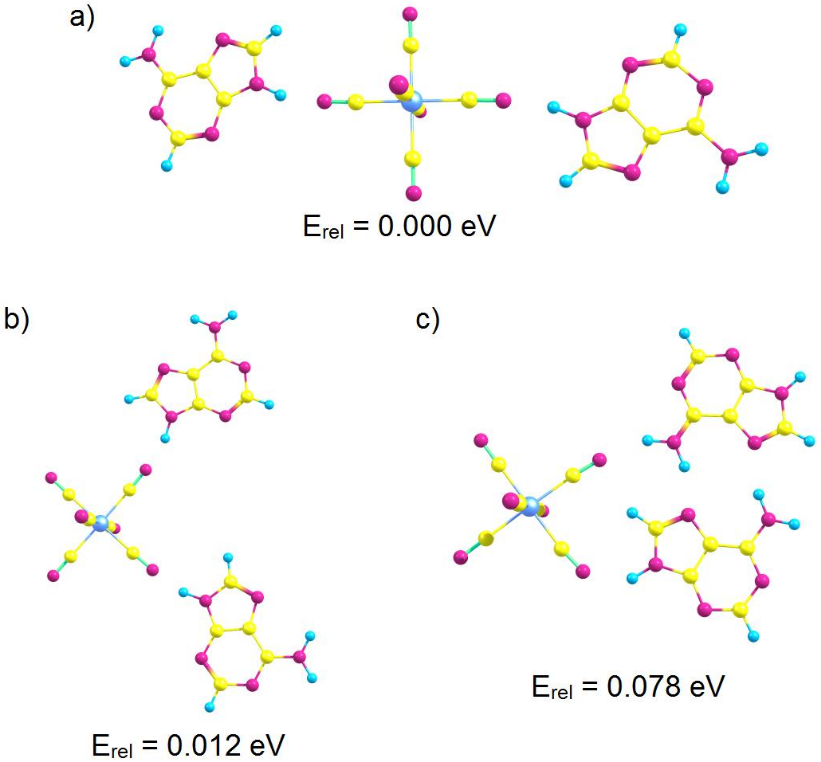

Figure 3.27: Low energy structures of $[Pt(CN)_6(Ad)_2]^{2-}$, a) structure **III**, b) structure **IV**, c) structure **V**. Relative energies are displayed in the figure.

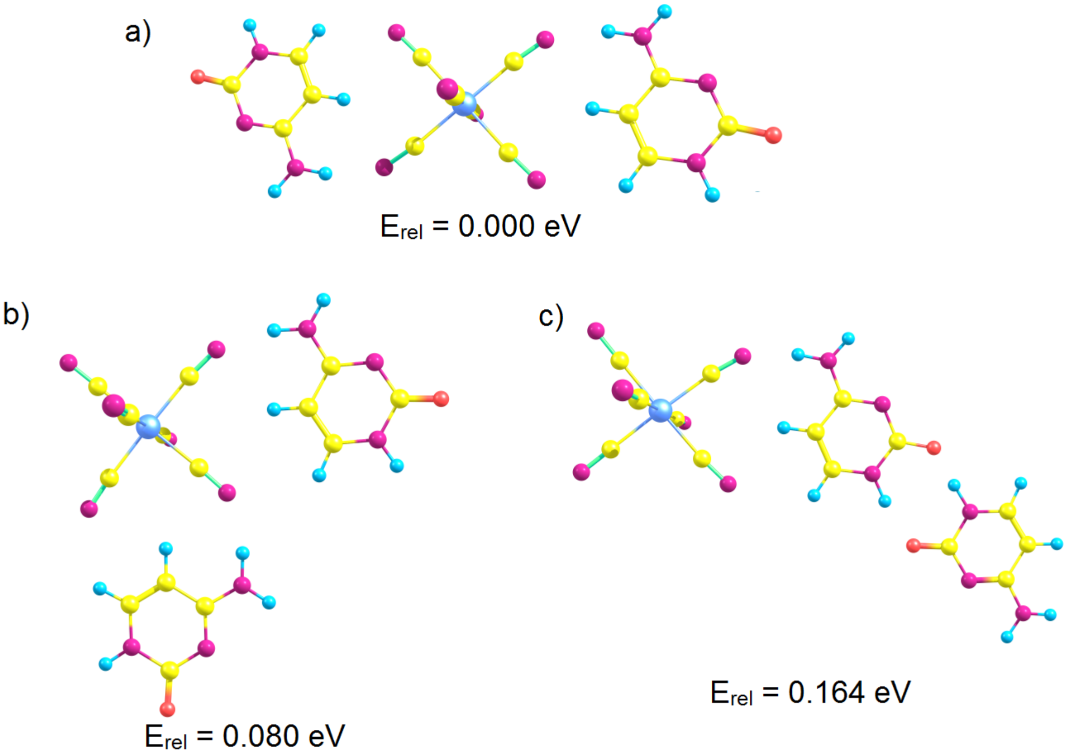

Figure 3.28: Low energy structures of $[Pt(CN)_6(Cy)_2]^{2-}$, a) structure **III**, b) structure **IV**, c) structure **V**. Relative energies are displayed in the figure.

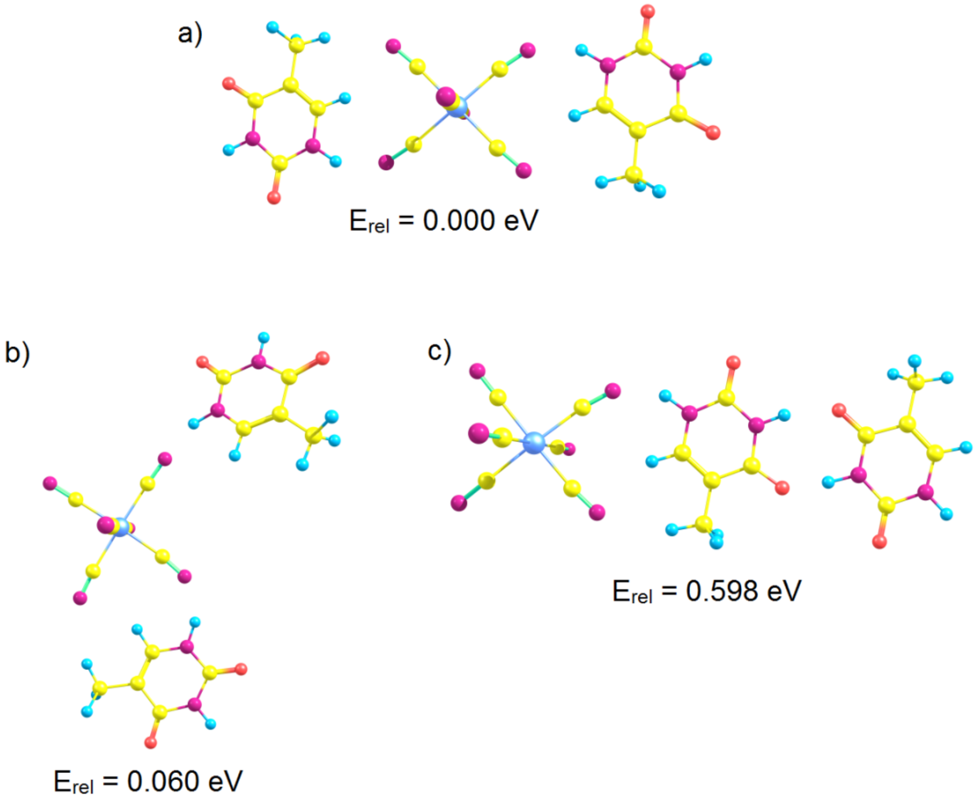

Figure 3.29: Low energy structures of $[Pt(CN)_6(Th)_2]^{2-}$, a) structure **III**, b) structure **IV**, c) structure **V**. Relative energies are displayed in the figure.

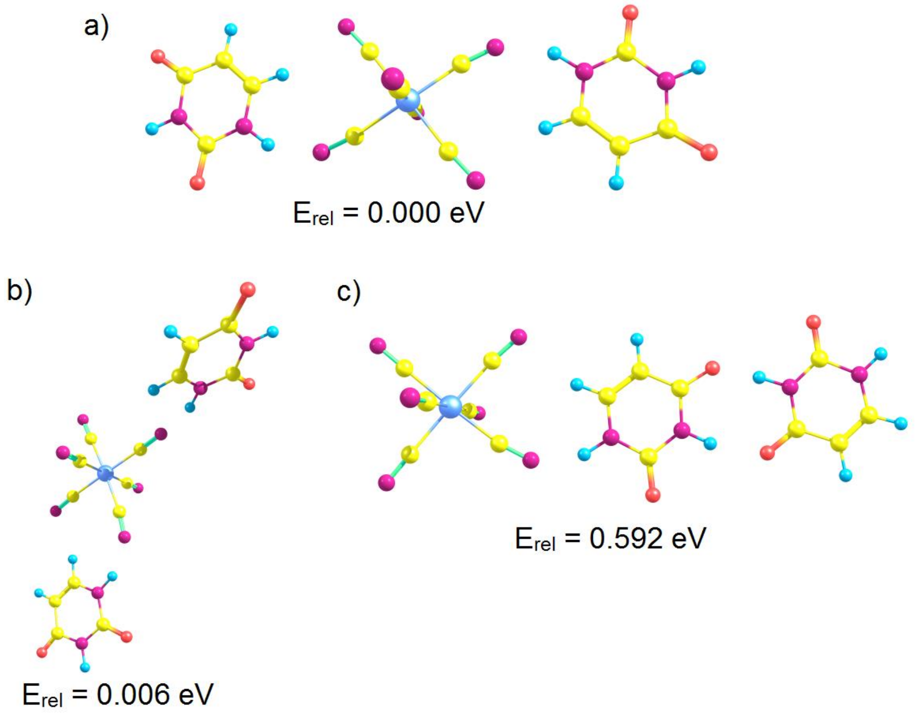

Figure 3.30: Low energy structures of $[Pt(CN)_6(Ur)_2]^{2-}$, a) structure **III**, b) structure **IV**, c) structure **V**. Relative energies are displayed in the figure.

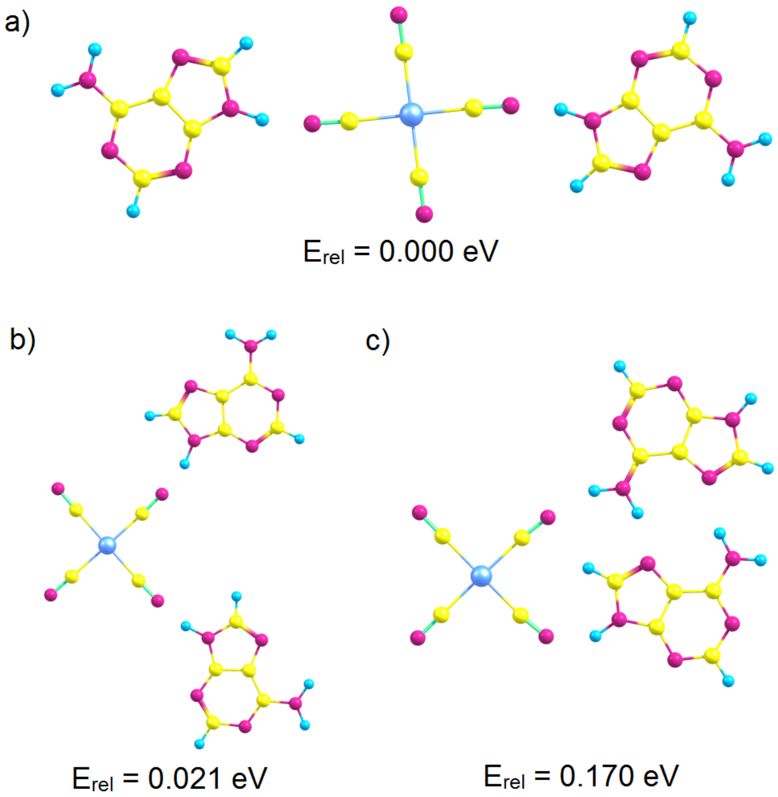

Figure 3.31: Low energy structures of $[Pt(CN)_4(Ad)_2]^{2-}$, a) structure **III**, b) structure **IV**, c) structure **V**. Relative energies are displayed in the figure.

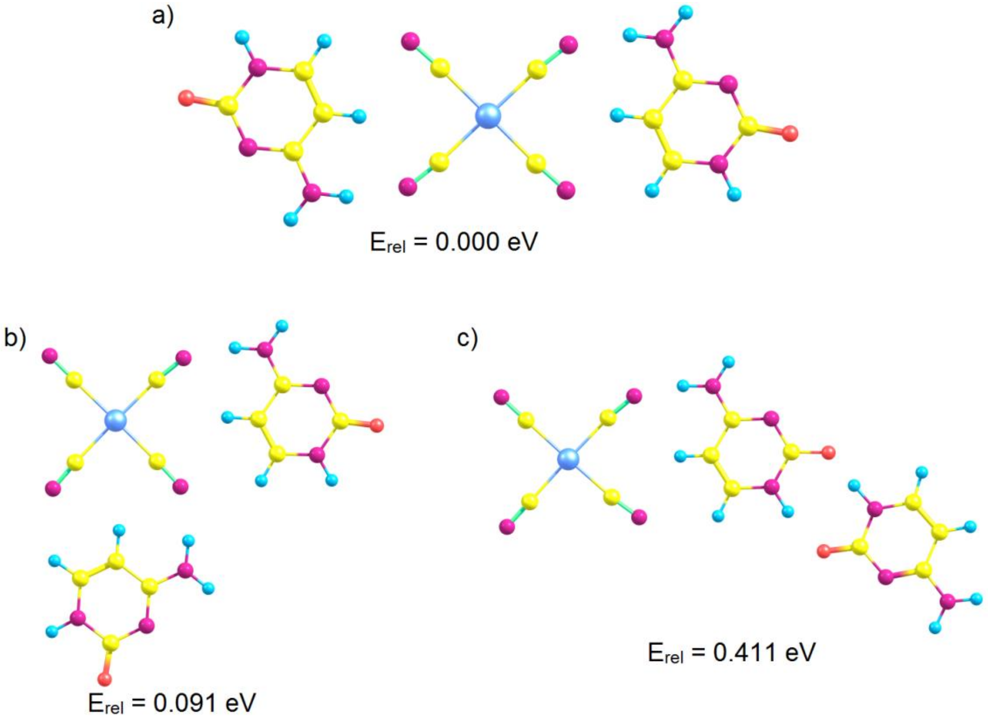

Figure 3.32: Low energy structures of $[Pt(CN)_4(Cy)_2]^{2-}$, a) structure **III**, b) structure **IV**, c) structure **V**. Relative energies are displayed in the figure.

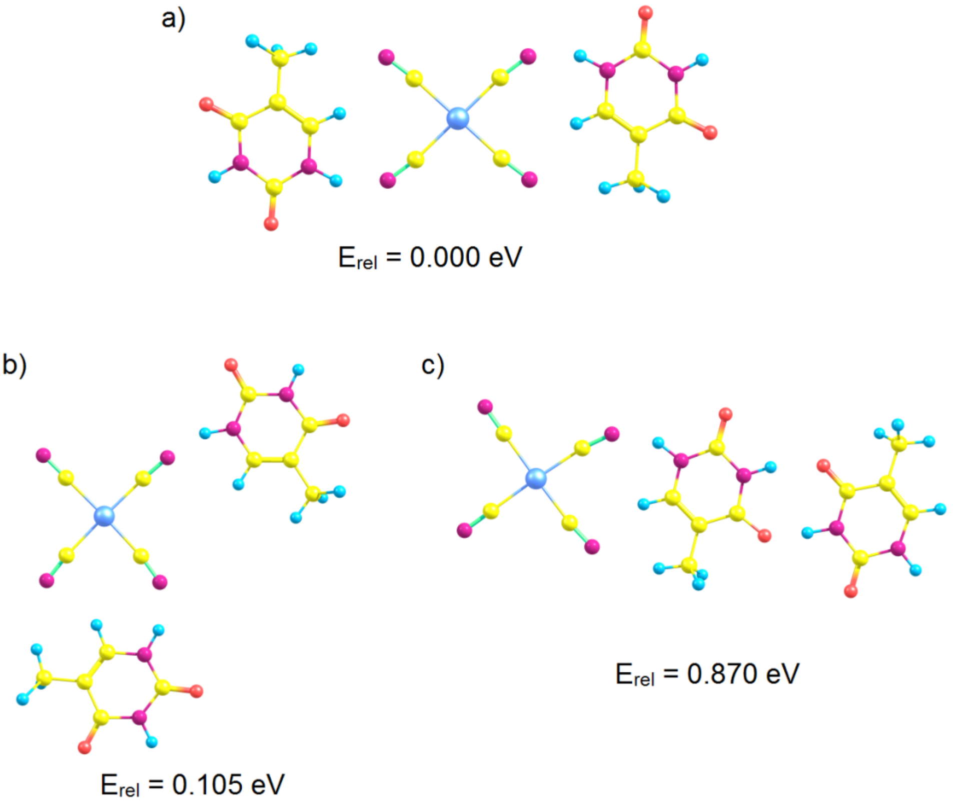

Figure 3.33: Low energy structures of $[Pt(CN)_4(Th)_2]^{2-}$, a) structure **III**, b) structure **IV**, c) structure **V**. Relative energies are displayed in the figure.

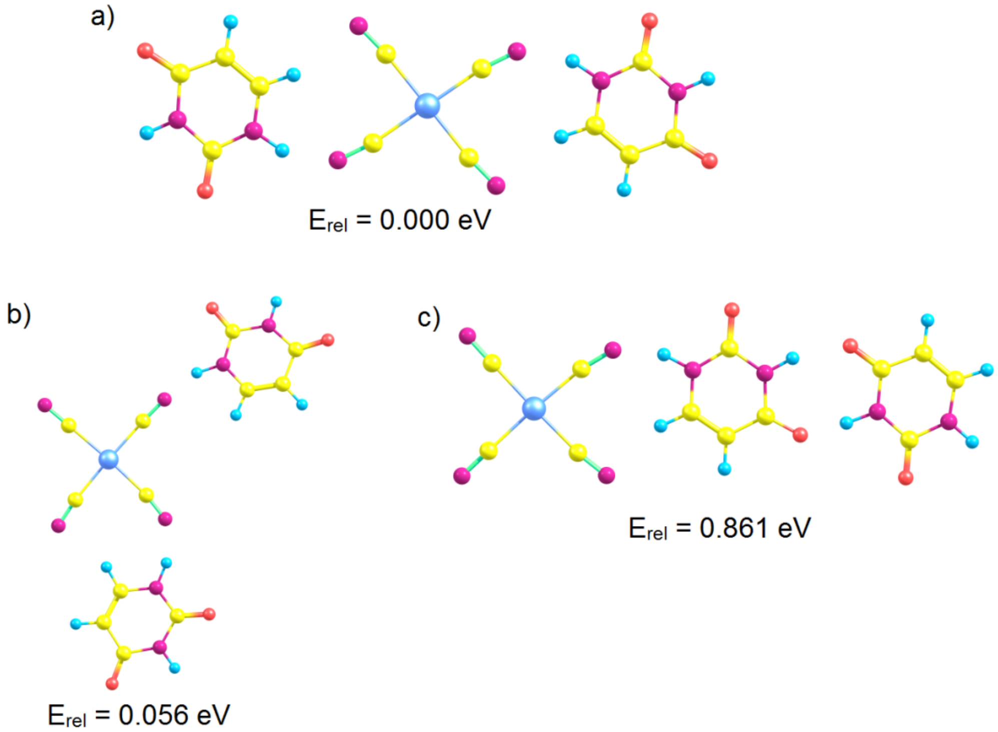

Figure 3.34: Low energy structures of $[Pt(CN)_4(Ur)_2]^{2-}$, a) structure **III**, b) structure **IV**, c) structure **V**. Relative energies are displayed in the figure.

Next, the clusters containing two nucleobases were investigated, with three low-energy structures examined for each. The first structure, **III**, has the nucleobases coordinating to opposite cyanide ligands, the second structure, **IV**, has the nucleobases coordinating to adjacent cyanide ligands and the final structure, **V**, has the two nucleobases hydrogen bonding together to form a base-pair. These structures are displayed in *Figures 3.27-3.30* for the $[Pt(CN)_6]^{2-}$ clusters and in *Figures 3.31-3.34* for the $[Pt(CN)_4]^{2-}$ clusters. In all cases, **III** was found to be the lowest energy structure and **V** to be the highest energy structure.

As with the clusters with a single nucleobase, the relative abundances of the different structures can be determined using the Boltzmann distribution equation (3.7). The results of this, displayed in *Tables 3.6 and 3.7*, show that structures **III** and **IV** will both be present under the conditions of the ion trap, while structure **V** will be present only in very small quantities. This is consistent with all of the experimental data and the structure postulated in *Section 3.3.1*.

Table 3.6: Relative energies and abundances of structures of the clusters $[Pt(CN)_6M_2]^{2-}$.

Nucleobase	**Relative Energy, E_{rel} / eV**			**Relative Abundance**		
	Structure **III**	Structure **IV**	Structure **V**	Structure **III**	Structure **IV**	Structure **V**
Adenine	0	0.012	0.078	59.8%	37.3%	2.9%
Cytosine	0	0.080	0.164	95.6%	4.2%	0.2%
Thymine	0	0.060	0.598	91.0%	9.0%	0.0%
Uracil	0	0.006	0.592	56.1%	43.9%	0.0%

Table 3.7: Relative energies and abundances of structures of the clusters $[Pt(CN)_4M_2]^{2-}$.

Nucleobase	**Relative Energy, E_{rel} / eV**			**Relative Abundance**		
	Structure **III**	Structure **IV**	Structure **V**	Structure **III**	Structure **IV**	Structure **V**
Adenine	0	0.021	0.170	69.4%	30.5%	0.1%
Cytosine	0	0.091	0.411	97.1%	2.9%	0.0%
Thymine	0	0.105	0.870	98.3%	1.7%	0.0%
Uracil	0	0.056	0.861	89.9%	10.1%	0.0%

It is interesting to note that the relative abundances of structures **IV** and **V** are higher in the $[Pt(CN)_6]^{2-}$ clusters than the equivalent $[Pt(CN)_4]^{2-}$ clusters. As $[Pt(CN)_6]^{2-}$ has the charge spread over more atoms, it is more stable[120] and so effective solvation of the charge will have less of an effect on the overall energy. This means that structures **IV** and **V**, which are less effective in solvating the charge, will be more favoured in the $[Pt(CN)_6]^{2-}$ clusters, leading to the observed higher abundances. A second interesting aspect to note is that structure **V** is present at a significantly higher abundance for the clusters containing adenine than any of the other nucleobases. By examining structure **V** for the clusters, it is seen that both of the adenine molecules are forming hydrogen bonds to the dianion in this structure, which is not observed for any of the other nucleobases. This will result in the charge being more effectively solvated, leading to a lower energy and higher abundance of the structure. Finally, the abundances of structure **IV** are significantly lower for the clusters of cytosine and thymine compared to the other two nucleobases. The optimal structure for the interaction of a single nucleobase (structure **I**) involves interaction of the nucleobase with one cyanide ligand for adenine and uracil and two cyanide ligands for cytosine and thymine. As structure **IV** has the nucleobases binding to adjacent sides of the dianion, there will be one cyanide ligand that both nucleobases would ideally interact with for the clusters with cytosine and thymine. This means that one of the nucleobases will be forced to bind in a sub-optimal position, raising the energy of the structure and causing the observed lower abundance.

In *Section 3.3.2*, it was observed that the $[Pt(CN)_4M_2]^{2-}$ clusters fragmented to produce a deprotonated nucleobase dimer (3.5b). This fragmentation channel was much more intense for adenine and uracil than for cytosine and thymine. Out of the three structures, the dimerization fragmentation channel is likely to occur from structures **IV** and **V**, as these have the two nucleobases in close proximity. As was discussed above, the relative abundance of structure **IV** is significantly higher for the clusters containing adenine and uracil, consistent with the presence of the dimerization fragmentation channel.

The relative strengths of the N-H hydrogen bonds of the clusters can be obtained by comparing the N-H bond lengths of the optimised structures (*Table 3.8*), as shorter bond lengths are associated with higher bond energies.[128] The results mirror what was observed in the experimental data: the hydrogen bonds are stronger for the platinum tetracyanide clusters and for the clusters with a single nucleobase.

Table 3.8: N-H hydrogen bond lengths in Å for the clusters $[Pt(CN)_mM_n]^{2-}$. M = Ad, Cy, Th, Ur; m = 4, 6; n = 1, 2.

	$[Pt(CN)_4M]^{2-}$	$[Pt(CN)_4M_2]^{2-}$	$[Pt(CN)_6M]^{2-}$	$[Pt(CN)_6M_2]^{2-}$
Adenine	1.570	1.611	1.681	1.708
Cytosine	1.827	1.858	1.909	1.934
Thymine	1.730	1.771	1.831	1.864
Uracil	1.679	1.718	1.773	1.802

3.3.5 Comparison to $[Pt(CN)_4(H_2O)_m]^{2-}$ and $[Pt(CN)_4(MeCN)_n]^{2-}$

A similar study has been conducted, using CID experiments and DFT calculations to investigate the interaction of the platinum tetracyanide dianion with the solvents water and acetonitrile.[105] The calculations performed for the cluster $[Pt(CN)_4(H_2O)_4]^{2-}$ indicate that the solvent molecules will all bind to one side of the dianion, forming a "surface solvated" structure. This is in contrast to the results presented in this chapter, which indicate that in the clusters $[Pt(CN)_4M_2]^{2-}$, the nucleobases will preferentially complex to different cyanide ligands. This stark difference between the two systems can be explained by the different degrees of polarisation within the nucleobases and the solvent molecules. Both water and acetonitrile are extremely polar molecules, with each atom carrying a large partial charge. This means that stabilisation of the solvent molecules by hydrogen bonding is more energetically favourable than stabilisation of the dianion. While the nucleobases have a number of polar groups, overall each atom will carry a much lower partial charge than those of the solvent molecules. This means that stabilisation of the nucleobases is not as necessary and it is more favourable for the nucleobases to solvate the charge on the dianion.

This difference is further reflected in the experimental results. The CID fragmentation of both the clusters containing water and acetonitrile lead to the loss of the entire solvent array, rather than the sequential loss observed here for the nucleobase clusters. This is consistent with the proposed structures for the clusters: if the solvent molecules were complexed as a surface solvated structure, the cleavage of a single hydrogen bond would lead to disruption of the entire solvent array, leading to the dissociation of all of the solvent molecules. On the other hand, if the solvent molecules were complexed individually, as was observed for the nucleobases in this study, the cleavage of one hydrogen bond would have little effect on the remaining solvent molecules and only a single molecule would dissociate.

3.4 Conclusion

In summary, gas phase clusters comprised of platinum cyanide dianions and different nucleobases have been synthesised using electrospray ionisation and investigated using low energy collision induced dissociation in a quadrupole ion trap. The platinum hexacyanide clusters were found to fragment by sequential dissociation of the uncharged nucleobases from the clusters, while the platinum tetracyanide clusters fragment by either sequential dissociation of the nucleobases or proton transfer to produce the $[Pt(CN)_4H]^-$ anion. As the number of nucleobases in the platinum tetracyanide clusters increase, the contribution of the deprotonation pathways decreases and direct dissociation becomes more prevalent. The strength of the hydrogen bonding interactions was found to be stronger for the clusters containing the platinum tetracyanide dianion, and for clusters with fewer nucleobases. These trends can be explained by considering the distribution of the excess charge over the dianion in these clusters.

DFT calculations were used to investigate the structures and relative energies of the clusters containing one and two nucleobases. In all cases, the structures of the clusters are very similar with both platinum tetracyanide and hexacyanide. For the two-nucleobase clusters, the structure with the lowest energy had the nucleobases forming hydrogen bonds to separate cyanide ligands.

Chapter 4

Effects of Varying Chain Length on the Interaction of Carboxylate Anions with Gas-Phase Arginine

4.1 Introduction

In solution[129] and as solids,[130] amino acids tend to exist in their charge-separated zwitterionic forms. The non-zwitterionic, canonical structures of the amino acids will predominate in the gas phase due to the lack of charge solvation from a solvent or from other intermolecular interactions.[131] The zwitterionic structure can be stabilised to varying degrees by complexation of a second species, such as solvent molecules,[41] alkali metals[50, 132] and halides,[40] making the study of the interactions of gas-phase amino acids a particularly interesting topic.

Understanding the interactions of ions with amino acids is important, as it can provide an insight into the ways in which these ions will interact with proteins in a biological system. For example, the Hofmeister series[2] ranks various ions based on their ability to salt in and out proteins and has been found to affect a number of physical properties in aqueous systems.[133-135] Studies of these systems in the gas phase is useful, as it enables the interactions to be inspected without interference from solvent molecules. It is therefore unsurprising that there have been a large number of studies looking at the interactions of gas phase of amino acids, both theoretically[136, 137] and experimentally, using techniques including infrared multiphoton dissociation[40, 138, 139] and collision induced dissociation.[50, 51]

This chapter describes the interaction of arginine with carboxylate anions, $CH_3(CH_2)_nCO_2^-$ (n = 3-7, 9, 10) and $HO_2C(CH_2)_nCO_2^-$ (n = 3-5, 7-10). Collision induced dissociation experiments in a quadrupole ion trap and molecular mechanics calculations are used to investigate the effect of altering the chain length of the carboxylate on the structure of the cluster. The work presented in this chapter builds on preliminary studies of these systems, conducted in a previous thesis,[140] in which only the n = 3-5, 9, 10 dicarboxylic acid systems were investigated. A change in the fragmentation patterns was observed for the dicarboxylic acid clusters after $n = 5$ and it was therefore postulated that a structural change occurred for the clusters at this chain length. This conclusion was clearly ambiguous since the full range of chain lengths had not been explored. In this study, we investigate the full range of systems to unambiguously determine the point at which the transition occurs. In addition to presenting the full experimental results, an extended set of molecular mechanics calculations are presented to support the experimental results.

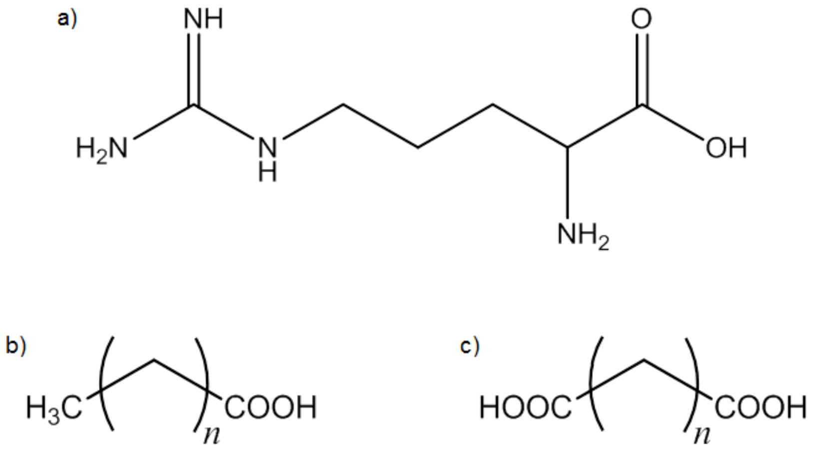

Figure 4.1: Species used in this chapter, a) arginine, b) monocarboxylic acids n = 3-5, 7-10, c) dicarboxylic acids n = 3-7, 9, 10.

4.2 Experimental

4.2.1 Experimental Methods

All experiments were performed using a Bruker Esquire 6000 Quadrupole Ion Trap mass spectrometer equipped with an electrospray ionisation ion source, run in negative mode, as described in *Chapter 2*. Samples were run with an injection rate of 4.0 µL min^{-1}, nebulising gas pressure of 10.0 psi, drying flow rate of 8.0 L min^{-1}, source temperature of 100˚C and ion excitation time of 40 ms. The ion signal was optimised using the automatic tuning function of the spectrometer, all spectra were averaged for 1 minute, from *m/z* 50-500 with a resolution of m/z 0.35 (FWHM). Fragment spectra were obtained using the manual CID function of the spectrometer, with an isolation window of m/z 2.0 and CID energy values quoted as a percentage of the maximum resonance excitation voltage (100% = 2.50 V).

The investigated species were created by electrospraying solutions containing both L-arginine and the relevant acid, both at 5×10^{-5} mol dm^{-3} in 100% methanol. All chemicals were purchased from Sigma-Aldrich and were used as provided, without additional purification.

All spectra are presented with their intensities normalised, such that the most intense signal has an intensity of 100%. This allows for easy comparison between fragmentation spectra, even where the absolute intensity of the parent ions varies considerably. CID curves were obtained by plotting the relative intensities of the signals in the fragmentation mass spectra relating to the parent and fragment ions against fragmentation energy, in steps of 0.4%. Typical experimental errors (obtained from repeat runs) were ±3%.

4.2.2 Computational Details

Calculations were performed using Spartan 08[141] with the MMFF94 force field.[142] Initially, the equilibrium geometry of the arginine-acid cluster was optimised. From this optimised structure, a conformer search was run, which examined 10,000 conformers and saved the 100 lowest energy conformers for further analysis.

Calculations were run for clusters of arginine in its canonical and zwitterionic forms, with singly deprotonated monocarboxylic acids and dicarboxylic acids. It is assumed for the calculations that the acid will be deprotonated and will carry the excess charge, as all of the acids investigated have a lower pk_a than arginine.[143, 144] It is possible for the deprotonated site to exist on the acid, on arginine, or distributed between the two, with the proton lying between the two partial negative charges. The structure of zwitterionic arginine involves deprotonation of the carboxylic acid group and protonation of the guanidine group, as these are respectively the most acidic and basic sites in canonical arginine.[145]

4.3 Experimental Results

4.3.1 Monocarboxylic Acid-Arginine Clusters

Collision induced dissociation (CID) fragmentation spectra of clusters of arginine (Arg) with the monocarboxylic acids $H_3C(CH_2)_nCO_2H$ (n = 3-7, 9, 10) are given in *Figure 4.2* (n = 8 was not investigated, as the peak in the mass spectrum for the cluster overlapped with the dimer of the acid and so could not be effectively isolated).

There are two significant fragmentation channels observed for these species: deprotonation (4.1a), and cyanamide loss (4.1b).

$$[\mathrm{H_3C(CH_2)}_n\mathrm{CO_2 \cdot Arg}]^- \rightarrow [\mathrm{Arg} - \mathrm{H}]^- + \mathrm{H_3C(CH_2)}_n\mathrm{CO_2H} \qquad (4.1a)$$

$$[\mathrm{H_3C(CH_2)}_n\mathrm{CO_2 \cdot Arg}]^- \rightarrow$$
$$[\mathrm{Arg} - \mathrm{CN_2H_2} - \mathrm{H}]^- + \mathrm{H_3C(CH_2)}_n\mathrm{CO_2H} + \mathrm{CN_2H_2} \qquad (4.1b)$$

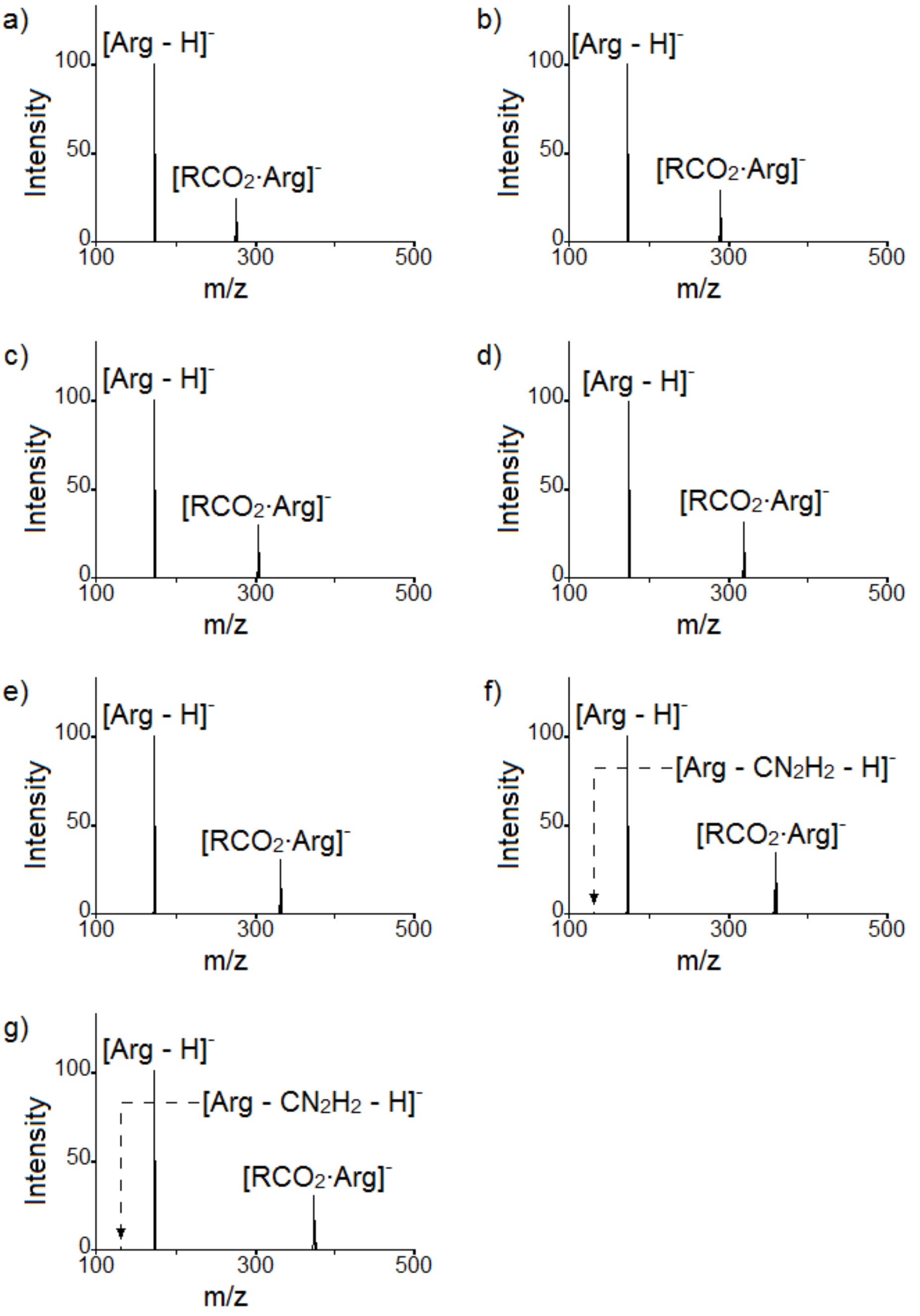

Figure 4.2: Negative ion fragmentation mass spectra of $[\mathrm{RCO_2 \cdot Arg}]^-$, R = $\mathrm{CH_3(CH_2)}_n$ for a) n = 3 at 8.0%, b) n = 4 at 7.6%, c) n = 5 at 7.6%, d) n = 6 at 8.0%, e) n = 7 at 8.4%, f) n = 9 at 8.4%, g) n = 10 at 8.8%.

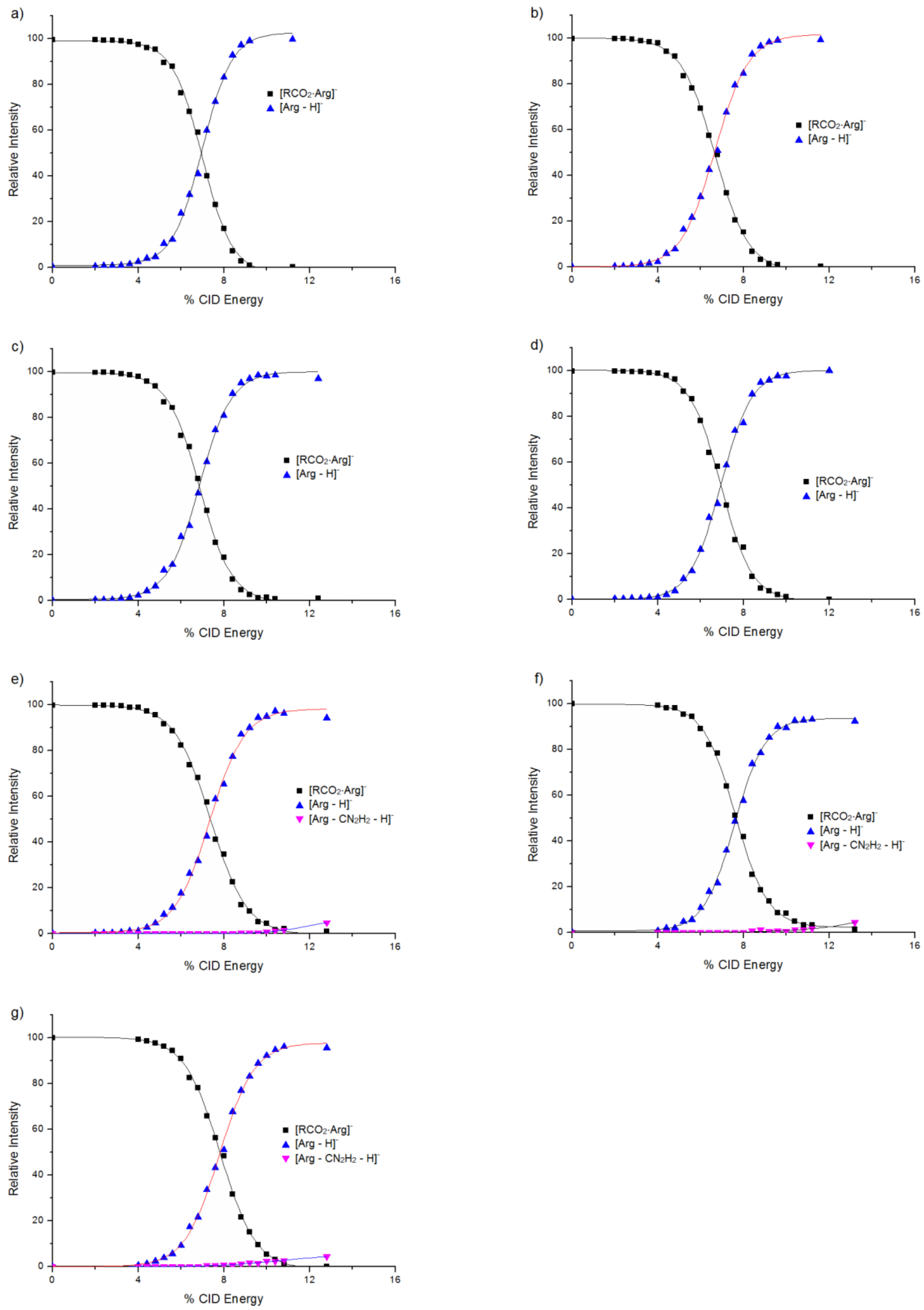

Figure 4.3: % CID curves for $[RCO_2{\cdot}Arg]^-$, R = $CH_3(CH_2)_n$, where a) $n = 3$, b) $n = 4$, c) $n = 5$, d) $n = 6$, e) $n = 7$, f) $n = 9$, g) $n = 10$.

For clusters with all of the monocarboxylic acids, the dominant fragmentation channel is deprotonation, with cyanamide ($H_2N{-}C{\equiv}N$) loss a relatively minor channel. The channel relating to the cyanamide loss is especially interesting, given that it has been linked to the presence of zwitterionic arginine.[51] Additionally, fragmentation channels are also observed for direct dissociation of the acid without deprotonation arginine (4.1c) and the loss of ammonia from arginine (4.1d), although these are significantly less intense than either of the major fragmentation channels.

$$[H_3C(CH_2)_nCO_2{\cdot}Arg]^- \rightarrow H_3C(CH_2)_nCO_2^- + Arg \qquad (4.1c)$$

$$\begin{aligned}&[H_3C(CH_2)_nCO_2{\cdot}Arg]^- \rightarrow \\ &[Arg - NH_3 - H]^- + H_3C(CH_2)_nCO_2H + NH_3 \qquad (4.1d)\end{aligned}$$

% fragmentation CID curves are given for the clusters in *Figure 4.3*. The precursor ions are stable across the low energy region, indicating that they are not metastable species.[119] By comparing the collision energy at which the relative intensity of the precursor ion reaches 50% ($E_{1/2}$), the stabilities of the different clusters can be compared.[82] As is seen in *Figure 4.4* and *Table 4.1*, $E_{1/2}$ of the clusters gradually rises as the chain length of the monocarboxylic acid increases. This can be explained by the longer hydrocarbon chains having a stronger inductive effect, donating more electron density to the carboxylate group and increasing the negative charge.[146] This results in an increase the strength of the electrostatic interaction of the carboxylate and the arginine.

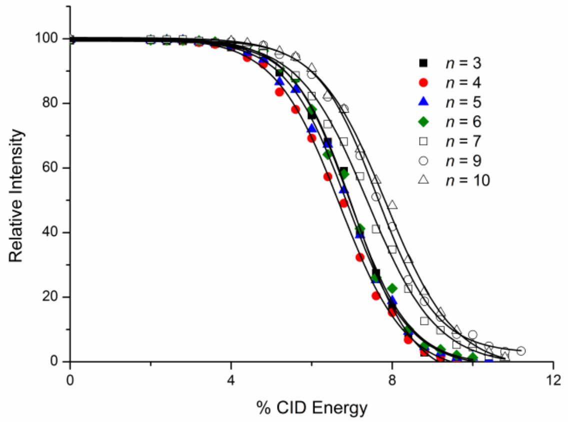

Figure 4.4: % Fragmentation decay curves for $[CH_3(CH_2)_nCO_2{\cdot}Arg]^-$, n = 3-7, 9, 10.

Table 4.1: Fragmentation energies and product ions for clusters $[CH_3(CH_2)_nCO_2{\cdot}Arg]^-$, n = 3-7, 9, 10.

Precursor ion $[CH_3(CH_2)_nCO_2{\cdot}Arg]^-$	$E_{1/2}$	**Product ions**
$n = 3$	7.0%	$[Arg – H]^-$
$n = 4$	6.8%	$[Arg – H]^-$
$n = 5$	6.9%	$[Arg – H]^-$, $[Arg – CN_2H_2 – H]^-$, $[Arg – NH_3 – H]^-$, RCO_2^-
$n = 6$	7.0%	$[Arg – H]^-$, $[Arg – CN_2H_2 – H]^-$, $[Arg – NH_3 – H]^-$, RCO_2^-
$n = 7$	7.4%	$[Arg – H]^-$, $[Arg – CN_2H_2 – H]^-$, $[Arg – NH_3 – H]^-$, RCO_2^-
$n = 9$	7.7%	$[Arg – H]^-$, $[Arg – CN_2H_2 – H]^-$, $[Arg – NH_3 – H]^-$, RCO_2^-
$n = 10$	7.9%	$[Arg – H]^-$, $[Arg – CN_2H_2 – H]^-$, $[Arg – NH_3 – H]^-$, RCO_2^-

4.3.2 Dicarboxylic acid-Arginine Clusters

CID fragmentation spectra of clusters of arginine and the dicarboxylic acids $HO_2C(CH_2)_nCO_2H$ (n = 3-5, 7-10) are shown in *Figure 4.5* (n = 6 was not investigated, as the peak for the cluster overlapped with the dimer of the acid). Alongside deprotonation (4.2b) and cyanamide loss (4.2c), which were also observed as major fragments for the monocarboxylic acid clusters, a third fragmentation channel, direct dissociation (4.2a) is also observed.

$$[HO_2C(CH_2)_nCO_2{\cdot}Arg]^- \rightarrow HO_2C(CH_2)_nCO_2^- + Arg \qquad (4.2a)$$

$$[HO_2C(CH_2)_nCO_2{\cdot}Arg]^- \rightarrow [Arg – H]^- + HO_2C(CH_2)_nCO_2H \qquad (4.2b)$$

$$[HO_2C(CH_2)_nCO_2{\cdot}Arg]^- \rightarrow$$
$$[Arg – CN_2H_2 – H]^- + HO_2C(CH_2)_nCO_2H + CN_2H_2 \qquad (4.2c)$$

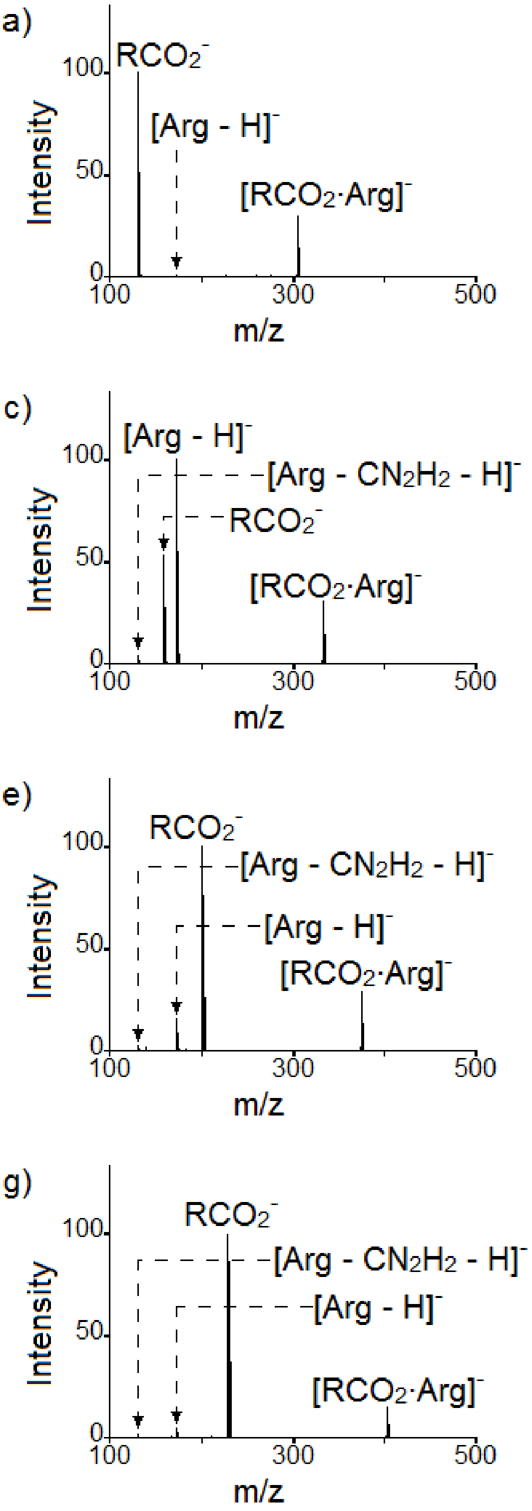

Figure 4.5: Negative ion fragmentation mass spectra of $[RCO_2 \cdot Arg]^-$, R = $HO_2C(CH_2)_n$, where a) $n = 3$ at 9.6%, b) $n = 4$ at 10.4%, c) $n = 5$ at 11.2%, d) $n = 7$ at 12.0%, e) $n = 8$ at 12.8%, f) $n = 9$ at 7.2%, g) $n = 10$ at 7.6%.

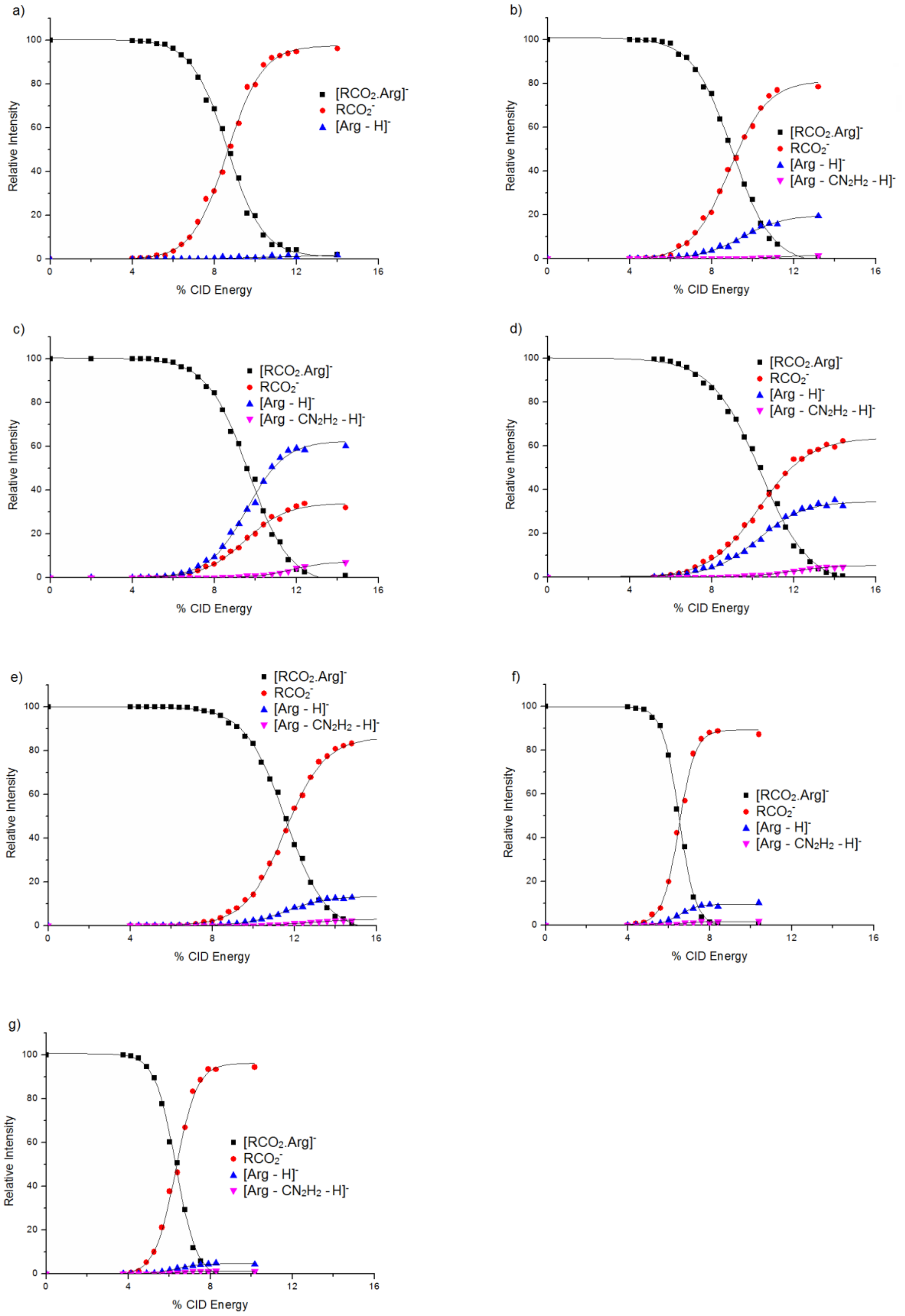

Figure 4.6: % CID curves for $[RCO_2{\cdot}Arg]^-$, R = $HO_2C(CH_2)_n$, where a) n = 3, b) n = 4, c) n = 5, d) n = 7, e) n = 8, f) n = 9, g) n = 10.

In contrast to the monocarboxylic acid clusters, direct dissociation is the most significant fragmentation channel for the majority of the dicarboxylic acid-arginine clusters. This is most likely due to the stabilities of the carboxylate ions of the monocarboxylic and dicarboxylic acids; the carboxylate of the dicarboxylic acid will be more stable, as the negative charge will be stabilised by hydrogen bonding from the second carboxylic acid group, reducing its basicity and therefore making it less susceptible to deprotonate arginine upon dissociation. The peak relating to deprotonation increases in intensity up to $n = 5$, for which it is the most intense channel. After this, it begins to decrease in intensity and direct dissociation becomes the most intense fragmentation channel again. For all of the clusters, the least significant 'major' fragment channel is cyanamide loss, although it is significantly more intense than for the monocarboxylic acid clusters. Additionally, low intensity, minor fragmentation peaks were observed for ions formed by the loss of ammonia from arginine (4.2d), and the fragmentation of the dicarboxylic acid to lose carbon dioxide (4.2e), water (4.2f) and both carbon dioxide and water (4.2g).

$$[HO_2C(CH_2)_nCO_2{\cdot}Arg]^- \rightarrow$$
$$[Arg - NH_3 - H]^- + HO_2C(CH_2)_nCO_2H + NH_3 \qquad (4.2d)$$

$$[HO_2C(CH_2)_nCO_2{\cdot}Arg]^- \rightarrow$$
$$[HO_2C(CH_2)_nCO_2 - CO_2]^- + Arg + CO_2 \qquad (4.2e)$$

$$[HO_2C(CH_2)_nCO_2{\cdot}Arg]^- \rightarrow$$
$$[HO_2C(CH_2)_nCO_2 - H_2O]^- + Arg + H_2O \qquad (4.2f)$$

$$[HO_2C(CH_2)_nCO_2{\cdot}Arg]^- \rightarrow$$
$$[HO_2C(CH_2)_nCO_2 - CO_2 - H_2O]^- + Arg + CO_2 + H_2O \qquad (4.2g)$$

% fragmentation CID curves were plotted for the dicarboxylic acid-arginine clusters (*Figure 4.6*) and the $E_{1/2}$ values compared (*Figure 4.7* and *Table 4.2*). The values of $E_{1/2}$ increase up to $n = 8$, after which the values drop dramatically and the fragmentation energy for $n = 9$ and 10 is significantly lower than for the other dicarboxylic acid clusters. The increase in $E_{1/2}$ for *n* = 3-8 is much more rapid than was observed for the monocarboxylic acid clusters, so it is unlikely that the increase is purely due to an increase in the inductive effect. It seems likely that there is a gradual change in the structure of the clusters as the chain length of the acid is increased. The step in $E_{1/2}$ from *n* = 8-9 is especially interesting as it indicates that there is a significant change in the structure of the cluster.

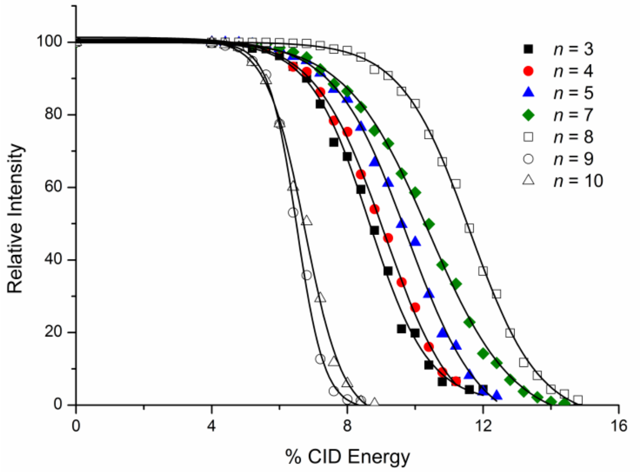

Figure 4.7: % Fragmentation decay curves for $[CH_3(CH_2)_nCO_2·Arg]^-$, *n* = 3-7, 9, 10.

Table 4.2: Fragmentation energies and product ions for clusters $[HO_2C(CH_2)_nCO_2·Arg]^-$, *n* = 3-6, 8-10.

Precursor ion $[HO_2C(CH_2)_nCO_2·Arg]^-$	**$E_{1/2}$**	**Product ions**
n = 3	8.8%	RCO_2^-, $[Arg – H]^-$, $[RCO_2 – CO_2]^-$, $[RCO_2 – H_2O]^-$
n = 4	9.1%	RCO_2^-, $[Arg – H]^-$, $[Arg – CN_2H_2 - H]^-$, $[Arg – NH_3 – H]^-$, $[RCO_2 – CO_2]^-$, $[RCO_2 – H_2O]^-$
n = 5	9.6%	$[Arg – H]^-$, RCO_2^-, $[Arg – CN_2H_2 - H]^-$, $[Arg – NH_3 – H]^-$, $[RCO_2 – CO_2 – H_2O]^-$, $[RCO_2 – CO_2]^-$, $[RCO_2 – H_2O]^-$
n = 7	10.4%	RCO_2^-, $[Arg – H]^-$, $[Arg – CN_2H_2 - H]^-$, $[Arg – NH_3 – H]^-$, $[RCO_2 – CO_2 – H_2O]^-$, $[RCO_2 – H_2O]^-$
n = 8	11.6%	RCO_2^-, $[Arg – H]^-$, $[Arg – CN_2H_2 - H]^-$, $[Arg – NH_3 – H]^-$, $[RCO_2 – CO_2 – H_2O]^-$, $[RCO_2 – H_2O]^-$
n = 9	6.5%	RCO_2^-, $[Arg – H]^-$, $[Arg – CN_2H_2 - H]^-$, $[Arg – NH_3 – H]^-$, $[RCO_2 – CO_2 – H_2O]^-$, $[RCO_2 – H_2O]^-$
n = 10	6.8%	RCO_2^-, $[Arg – H]^-$, $[Arg – CN_2H_2 - H]^-$, $[Arg – NH_3 – H]^-$, $[RCO_2 – CO_2 – H_2O]^-$, $[RCO_2 – H_2O]^-$

4.4 Theoretical Results

In an attempt to better understand the system, a theoretical study was undertaken to supplement the experimental results. Clusters of canonical and zwitterionic arginine with deprotonated monocarboxylic acids $H_3C(CH_2)_nCO_2H$ (n = 3-9) and dicarboxylic acids $HO_2C(CH_2)_nCO_2H$ (n = 4-10) were investigated.

Using the conformer distribution feature of Spartan 08,[141] the 100 lowest energy conformers were obtained for each cluster. Although the ions in the trap are collisionally cooled by the helium buffer gas, they will still have sufficient energy to convert between the low energy conformers.[147] This means that the results obtained through the conformer distribution calculation will give a representation of the different conformers of the clusters present in the trap.

4.4.1 Monocarboxylic Acid-Arginine Clusters

The conformer distributions for the clusters of zwitterionic arginine and the monocarboxylic acids produced results where all of the 100 low energy conformers had the same structure (*Figure 4.8*). This structure involves an interaction of the arginine to the carboxylate group of the acid through the protonated guanidinium group, with two hydrogen bonds. This type of hydrogen bonding interaction is not unusual and has been observed for both arginine[148] and carboxylates.[109] Additionally, the guanidinium group will form an intramolecular hydrogen bond to the carboxylate of the arginine. The unfunctionalised hydrocarbon chain will orient away from the arginine molecule and will not significantly interact with the rest of the cluster.

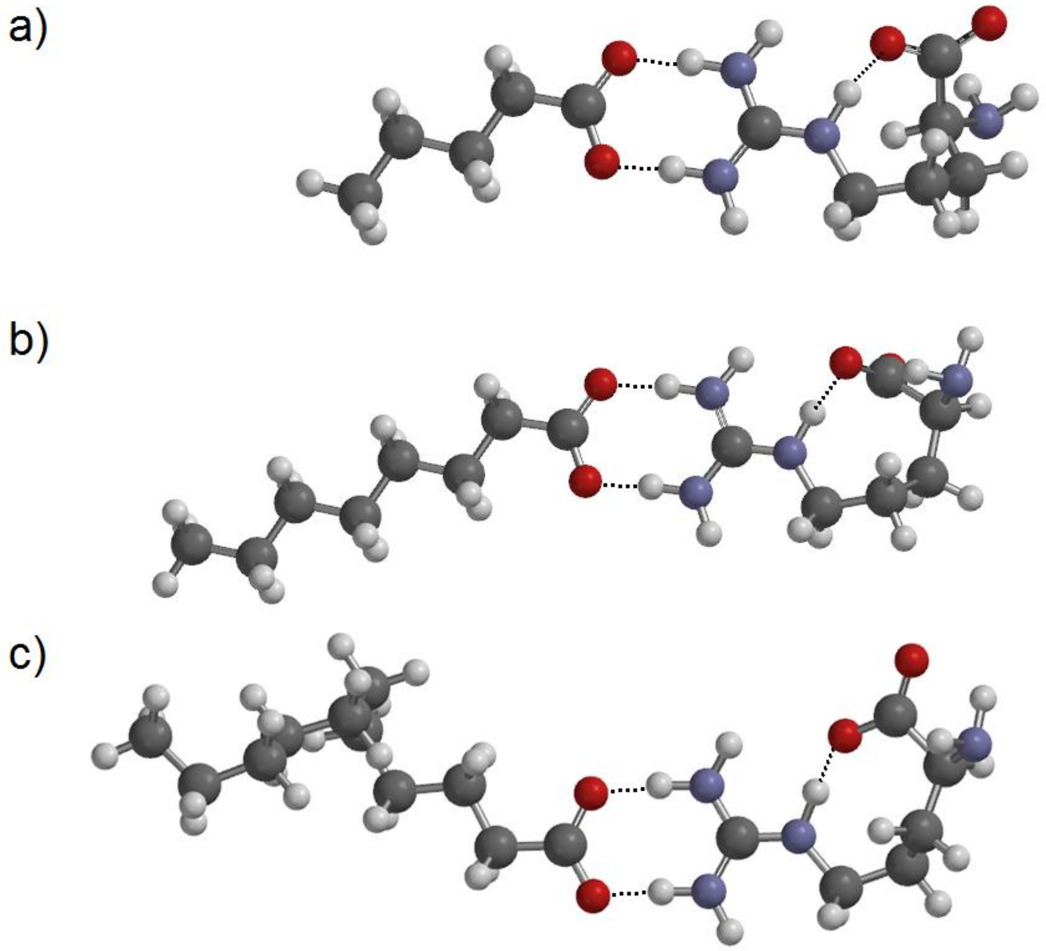

Figure 4.8: Structures of zwitterionic arginine clusters of $[CH_3(CH_2)_nCO_2 \cdot Arg]^-$, where a) $n = 3$, b) $n = 6$, c) $n = 9$.

Similar results are obtained for the clusters of canonical arginine with the monocarboxylic acids (*Figure 4.9*). One structure is observed, with arginine hydrogen bonding to the carboxylate group of the acid and the hydrocarbon chain not significantly interacting. However, hydrogen bonding from arginine will occur through multiple sites, consisting of the carboxylic acid group, the guanidine group and in some cases, the amino group.

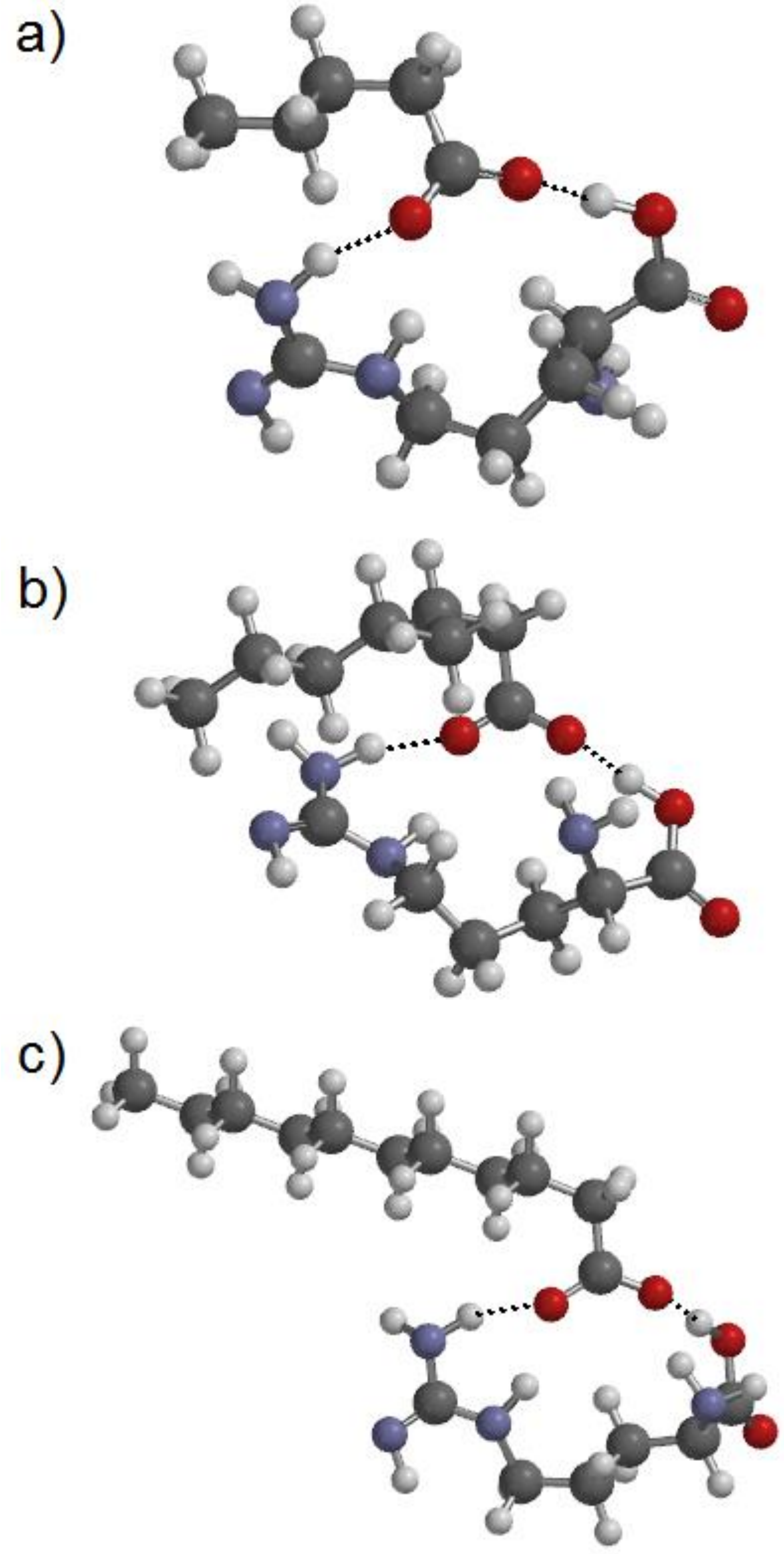

Figure 4.9: Structures of canonical arginine clusters of $[CH_3(CH_2)_nCO_2{\cdot}Arg]^-$, where a) $n = 3$, b) $n = 6$, c) $n = 9$.

As the chain length of the monocarboxylic acid increases, there is no obvious change in the structures of the clusters with either canonical or zwitterionic arginine. This is expected, as the only change in the structures is the increasing length of the hydrocarbon tail, which does not interact with the rest of the cluster and so, would not be expected to affect the structures significantly.

4.4.2 Dicarboxylic Acid-Arginine Clusters

The experimental results for the clusters of arginine with the dicarboxylic acids indicate that they are more complicated than their monocarboxylic acid counterparts. This is likely to be the result of the dicarboxylic acids having a second functional group, increasing the number of ways in which they can bind to arginine. This is reflected in the results of the conformer search, which show that the 100 lowest energy conformers of the zwitterionic arginine-dicarboxylic acid clusters can be assigned to two structures.

The first structure, **zI** (*Figure 4.10*), involves a somewhat similar structure to the monocarboxylic acid-zwitterionic arginine structure, with the arginine donating two hydrogen bonds through the guanidinium group to the carboxylate of the acid, as well as one to the carboxylate of the arginine. The carboxylic acid group of the acid will hydrogen bond intramolecularly to the carboxylate group of the acid. The second structure, **zII** (*Figure 4.11*), again involves the guanidinium group of the arginine double-hydrogen bonding to the carboxylate group of the acid, but this time, the carboxylic acid group of the acid will hydrogen bond intermolecularly to the carboxylate group of the arginine to form a ring-like structure.

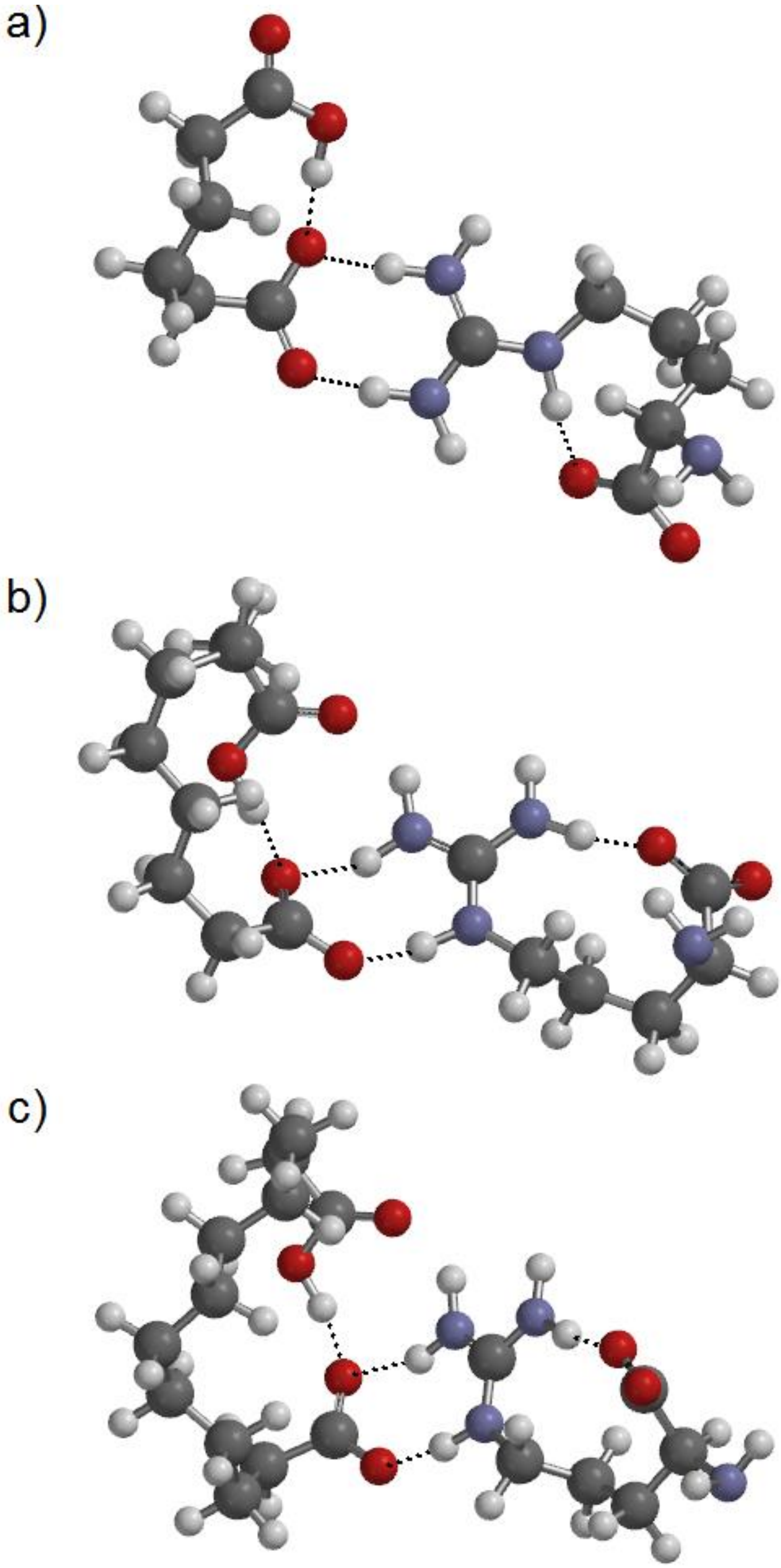

Figure 4.10: Structures of zwitterionic arginine clusters, conformer **zI**, $[HO_2C(CH_2)_nCO_2 \cdot Arg]^-$, where a) $n = 4$, b) $n = 7$, c) $n = 10$.

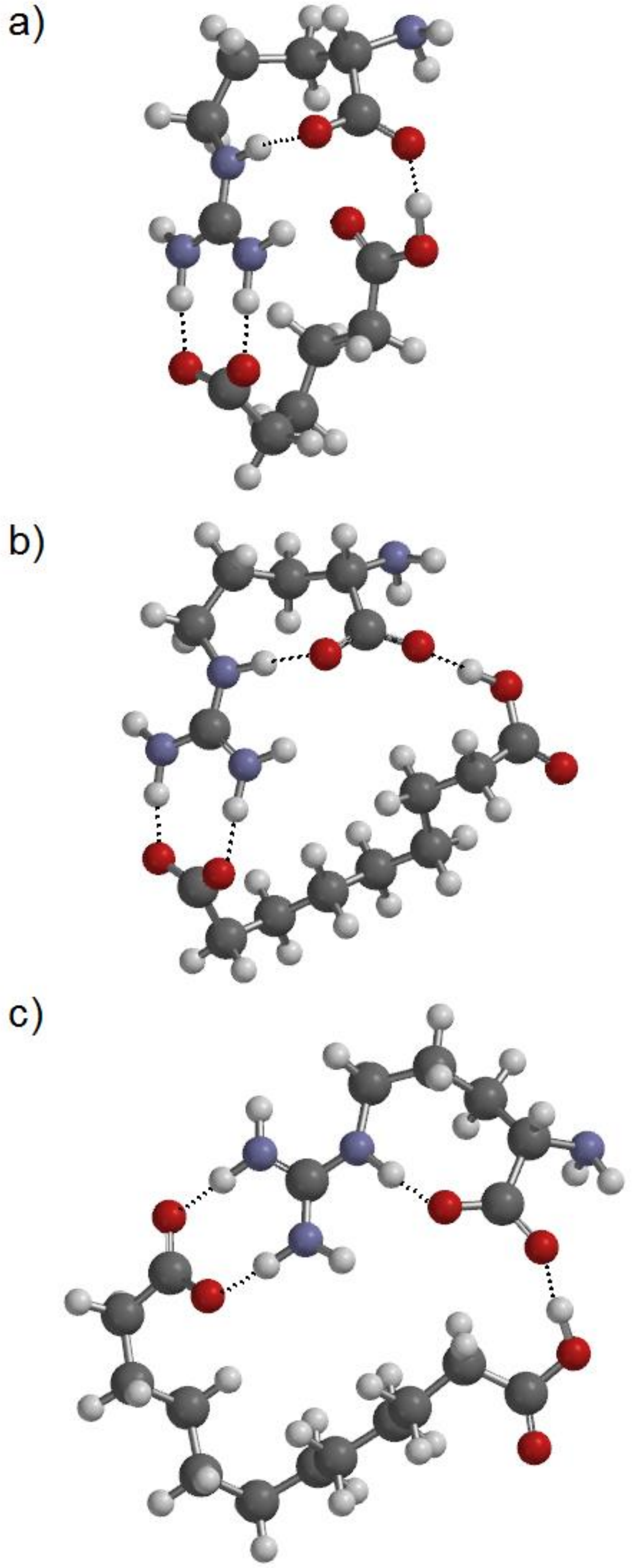

Figure 4.11: Structures of zwitterionic arginine clusters, conformer **zII**, $[HO_2C(CH_2)_nCO_2\cdot Arg]^-$, where a) $n = 4$, b) $n = 7$, c) $n = 10$.

As the chain length of the dicarboxylic acid increases, the two structures stay remarkably similar, however the number of conformers assigned to each structure changes dramatically (*Figure 4.12*). For n = 4, both structures are observed in significant numbers, with structure **zII** being present slightly in excess. As the chain length of the acid increases, the proportion of structure **zII** increases and by n = 6, it is present overwhelmingly in excess. This trend can be easily explained: structure **zII** is the overall favoured structure and so predominates for the longer chain dicarboxylic acids. However, for the acids with shorter chains, the cluster has to take a very strained structure to allow both interactions to occur. As a result, structure **zI** becomes favoured, as it can be formed without a significant amount of strain.

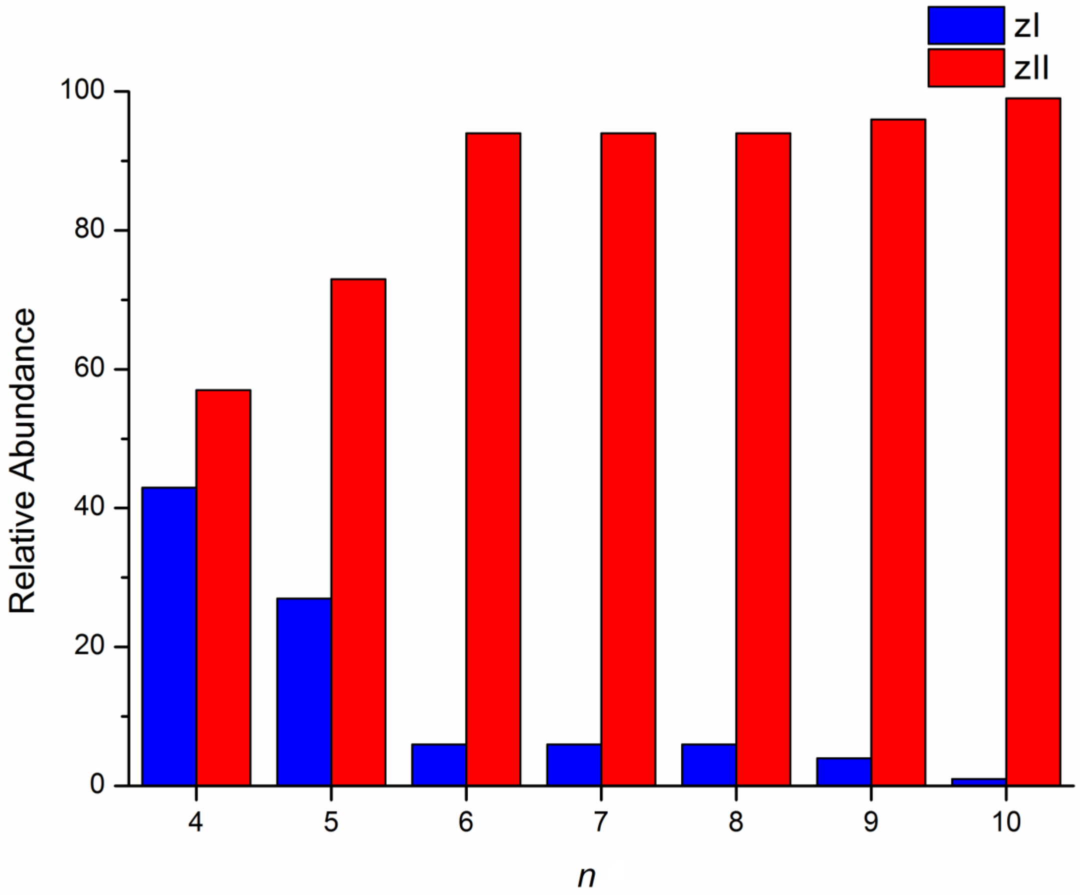

Figure 4.12: Relative abundance of conformers **zI** and **zII** in the zwitterionic arginine clusters $[HO_2C(CH_2)_nCO_2{\cdot}Arg]^-$, n = 4-10

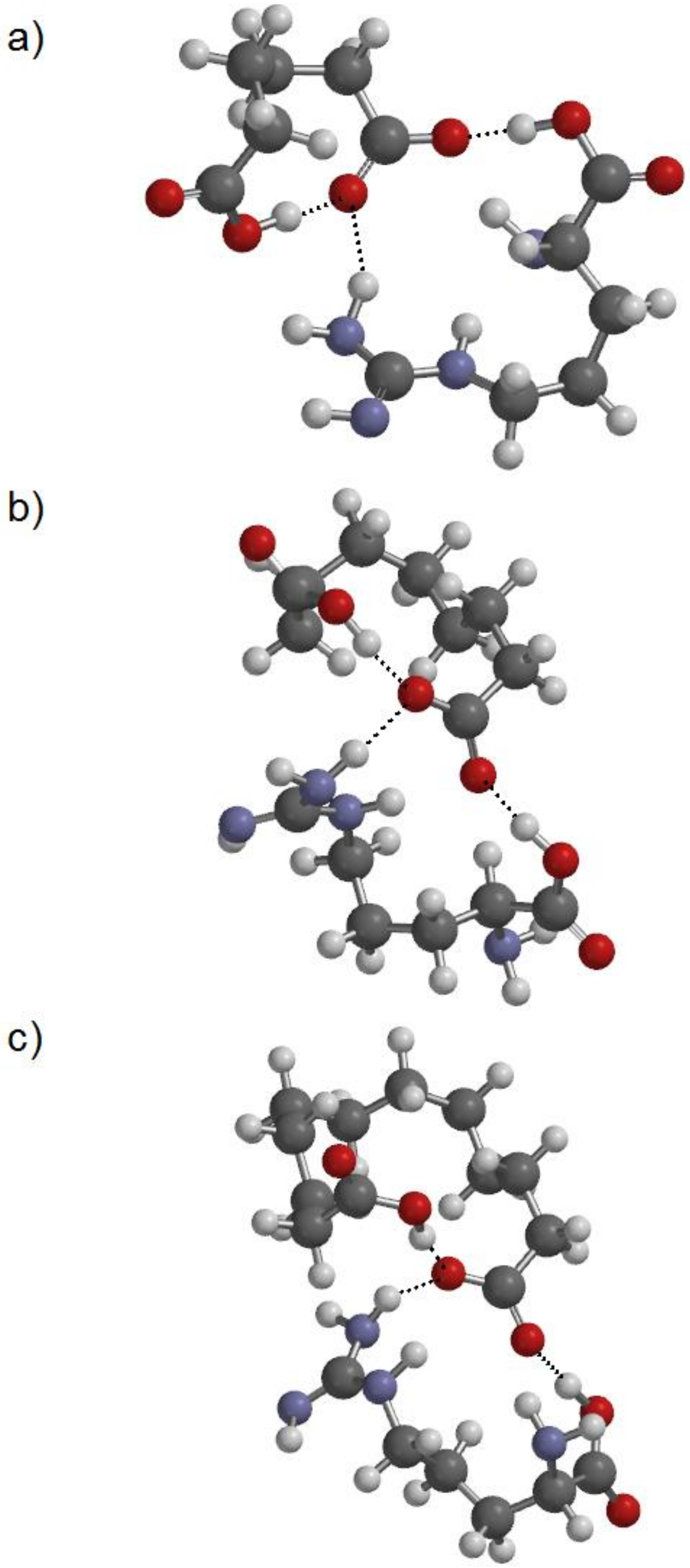

Figure 4.13: Structures of canonical arginine clusters, conformer **cI**, $[HO_2C(CH_2)_nCO_2 \cdot Arg]^-$, where a) $n = 4$, b) $n = 7$, c) $n = 10$.

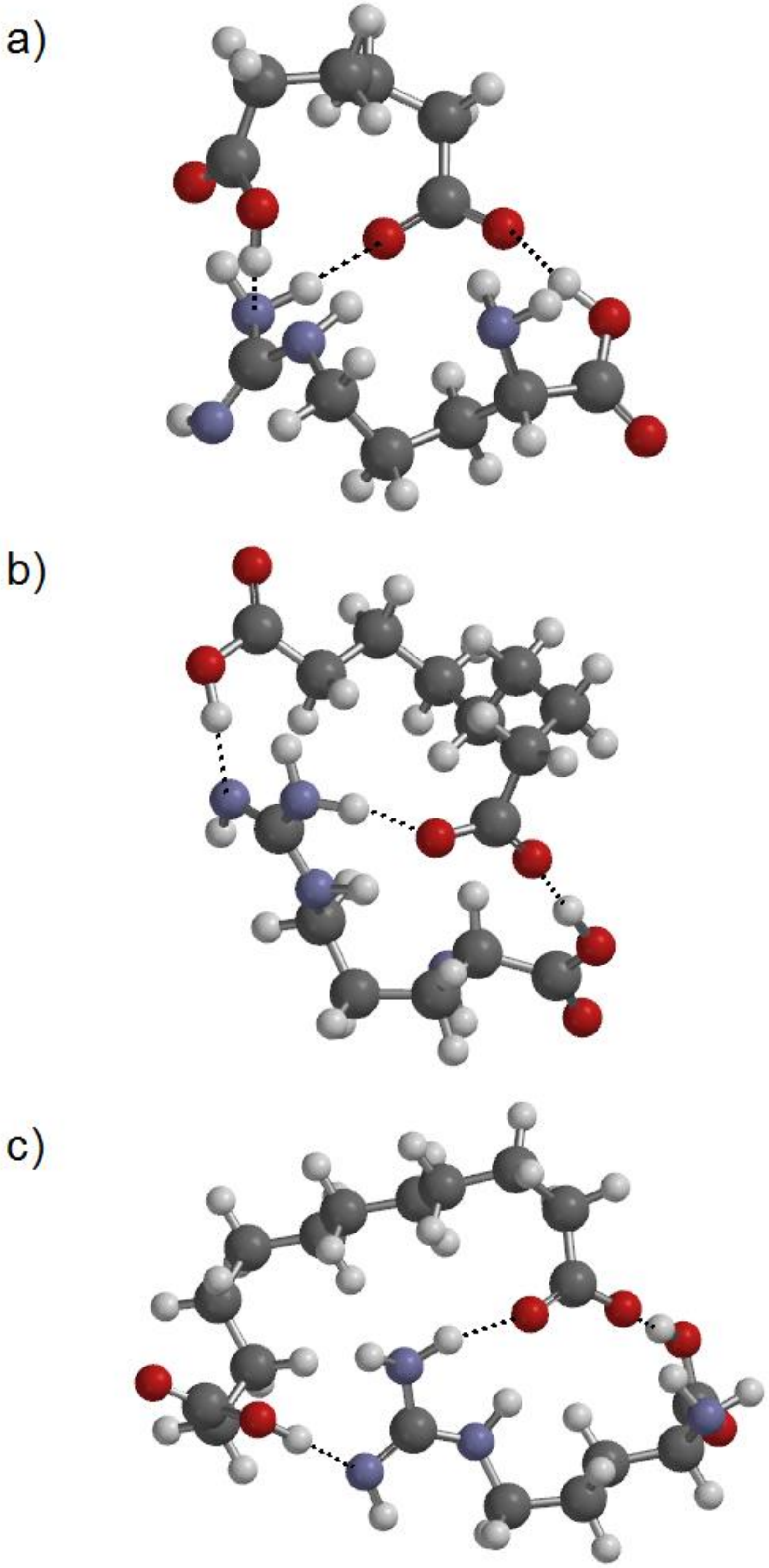

Figure 4.14: Structures of canonical arginine clusters, conformer **cII**, $[HO_2C(CH_2)_nCO_2{\cdot}Arg]^-$, where a) $n = 4$, b) $n = 7$, c) $n = 10$.

As with the zwitterionic structures, the conformers obtained for the canonical structures of the cluster can be arranged into two structural groups. The first structure, **cI** (*Figure 4.13*), involves hydrogen bonding of the arginine to the carboxylate group of the dicarboxylic acid through the carboxylic acid and guanidine groups. The carboxylic acid group of the acid will form an intramolecular hydrogen bond to the carboxylate group. The second structure, **cII** (*Figure 4.14*), again involves hydrogen bonding of arginine to the dicarboxylic acid's carboxylate through multiple sites. The carboxylic acid group of the acid will form a hydrogen bond to the arginine, usually to a lone pair on the guanidine group, but in some cases to the carboxylic acid. These structures, **cI** and **cII** are roughly analogous to the zwitterionic structures **zI** and **zII** respectively.

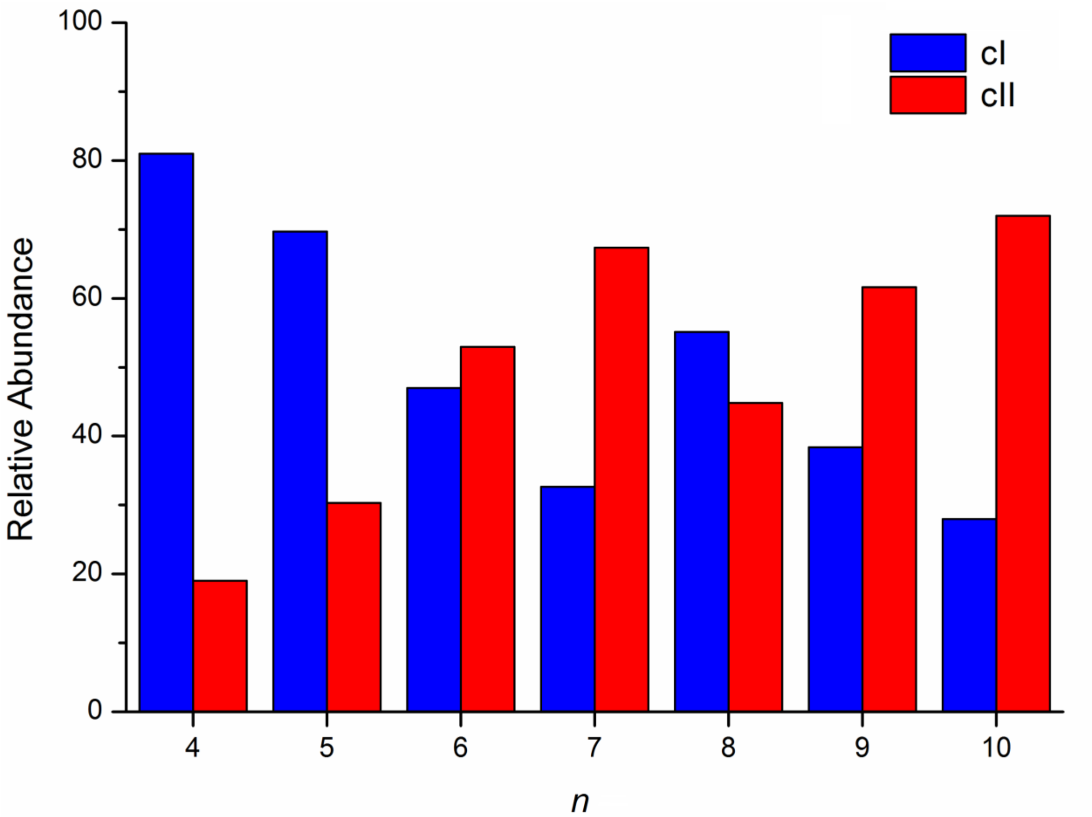

Figure 4.15: Relative abundance of conformers cI and cII in the canonical arginine clusters $[HO_2C(CH_2)_nCO_2{\cdot}Arg]^-$, n = 4-10

As the chain length of the acid increases, the contribution of conformer **cII** increases (*Figure 4.15*), corresponding to the reduction in strain of the cluster, as was also observed for the zwitterionic structures, although the change is much more gradual. For n = 4, structure **cII** has a contribution of 19%, which gradually rises until at n = 10 the contribution is 72%. The exception to this trend is the change from n = 7-8, at which point, the contribution of conformer **cII** decreases from 67% to 45%, after which it continues to rise at a similar rate to before. The reasons for this shift in conformer distribution are unclear, there is no obvious change in the structure of either of the conformers from before or after the shift and neither conformer appears to be particularly strained, either before or after the change.

4.4.3 Comparisons to Experimental Data

The results obtained from the conformer distribution calculations for the monocarboxylic acid-arginine clusters show that there is no change in the conformer distribution as the chain length of the acid increases. This is fully consistent with the experimental results, which do not indicate that there is any change in the structure of the clusters.

The dicarboxylic acid-arginine clusters see a change in the conformer distribution as the chain length of the acid increases. This is consistent with the experimental results, in which the increasing $E_{1/2}$ values of the clusters indicate a change in structure as the length of the acid increases. Furthermore, the binding energies for structure **cII** and **zII**, which predominate for the longer dicarboxylic acids, are expected to be higher than **cI** and **zI**. This is a result of the **cII** and **zII** structures each having an additional site of interaction between the acid and arginine, with the carboxylic acid group of the dicarboxylic acid forming an intermolecular hydrogen bond to arginine.

While the general increase in $E_{1/2}$ from *n* = 3-8 is explained by the conformer distributions, there is much less information regarding the change in structure predicted from the change in fragmentation energy for the *n* = 9 and 10 dicarboxylic acid-arginine clusters. The 'step' in the conformer distribution of the dicarboxylic acid-canonical arginine clusters from *n* = 7-8 appears to somewhat match the trend in binding energy. However, the change is much smaller than would be expected for that dramatic a difference in binding energy and the change occurs at a different chain length. This means that a simple change in the conformer distribution cannot be used to adequately explain the change in fragmentation energy observed.

One potential explanation for the change in fragmentation energy is that for *n* = 3-8 the clusters contains zwitterionic arginine and *n* = 9, 10 contains canonical arginine. If this were the case, it would not have been observed in the conformer distribution calculations, as canonical and zwitterionic arginine were treated separately. Calculations at a higher level of theory, such as DFT[86] could be used to determine the relative energies of the clusters, and thus determine which form of arginine will predominate in with different acids. Alternately, using infrared multiphoton dissociation, infrared spectra of the clusters inside the ion trap could be generated,[37] allowing the structures of the ions to be investigated directly.

4.5 Conclusions

The theoretical results obtained provide a new perspective on the experimental data, and can provide the solutions to a number of questions unanswerable purely through collision induced dissociation experiments.

The calculations provide a convincing explanation of the general trends observed in the binding energy observed in the experimental data. For the monocarboxylic acid-arginine clusters, the minimal change of $E_{1/2}$ with acid chain length is explained by the conformer distributions obtained, in which there is no significant change with chain length. The small increase in $E_{1/2}$ that is observed can be attributed to an increase in the inductive effect with acid chain length. The significantly more rapid increase in $E_{1/2}$ for the dicarboxylic acid-arginine clusters as the chain length of the acid increases is explained by the increasing contribution of conformers with a ring-like structure. This structure contains an additional hydrogen bonding site connecting the acid and arginine, resulting in an increase in the strength of the overall interaction.

The theoretical results do not entirely explain the significant drop in the binding energy observed for the longer chain dicarboxylic acid-arginine clusters. This is most likely the result of limitations of the calculations. Notably, the clusters containing canonical and zwitterionic arginine were treated separately, while it is possible that a combination of the two is present. Higher level calculations and IR spectroscopy could be used to provide a more in depth understanding of the clusters, and could help to understand this change in structure.

Analysis of the dianionic clusters, where the dicarboxylic acids are doubly deprotonated could be used to see if comparable results could be produced. It would be expected that these dianionic clusters would have a higher binding energy than those investigated here, due to stronger electrostatic interactions caused by the increased negative charge. Additionally, clusters of arginine with different extended molecular ions, such as amines, alcohols or sulfates, could be analysed to see if the trends observed here are unique to carboxylic acids or will translate to other systems.

Chapter 5

Potential Syntheses and Electrospray Ionisation Mass Spectrometry of Subnanometre Clusters

5.1 Introduction

Since the 1980s, the study of metal nanoparticles has become a major area of interest in research due to their interesting chemical and physical properties, bridging the gap between molecular and material systems. Clusters of metal atoms smaller than one nanometre further bridge this gap and have received a significant amount of attention in the last few years.[149-156] While the distinction of these ‘subnanometre clusters’ (also referred to as quantum clusters) with small nanoparticles (1-2 nm) is entirely arbitrary, they do display a number of interesting properties, not seen in larger nanoparticles. In contrast to nanoparticles, they tend to exhibit a number of molecule-like properties, including discrete energy levels[157] and strong photoluminescence.[158, 159] These properties have shown to be significantly affected by the number of atoms in the cluster.[160]

Clusters with a range of metals, including Cu, Ag, Au and Pt, with sizes ranging from two atoms to tens of atoms have been produced, through a range of different methods. There are two general methods by which the clusters can be synthesised: either the clusters can be produced ‘bottom-up’ by the reduction of a molecular precursor or ‘top-down’ by etching a larger nanoparticle.[156] As with nanoparticles, a protecting ligand is required to prevent the subnanometre clusters from aggregating. The number of atoms in the resulting clusters, and therefore the properties, can be controlled by altering the conditions of the synthesis. Characterisation is achieved using a range of methods, including UV-vis and IR spectroscopy, elemental analysis and mass spectrometry.

While there has been extensive characterisation of subnanometre clusters in the solid phase and in solution, there has been significantly less work done to characterise these systems as isolated particles in the gas phase.[161-164] This is an area that we are interested in exploring as it allows for detailed structures to be probed, without interference by the interactions of solvent molecules. We are especially interested in investigating the interactions of these subnanometre clusters with molecules of biological interest, which is not an area that has been extensively studied. This can provide an insight into how they will interact in biological systems, allowing for potential health risks and cytotoxic properties of the clusters to be assessed. In order to do this, we searched the literature for a synthesis that could be used to produce appropriate clusters for our needs. The synthesis would ideally be reasonably simple and needs to produce subnanometre clusters that can be electrosprayed to produce ions with a mass to charge ratio of below 3,000. In this chapter, we describe our attempts to synthesise the subnanometre clusters through various previously described methods.

5.2 Tryptophan and Silver Nitrate

Quadrupole ion trap (QIT) mass spectrometry experiments, conducted by the group of Philippe Dugourd found that singly charged silver subnanometre clusters could be produced.[165] The clusters were initially formed by electrospraying a solution of tryptophan (Trp) and silver nitrate ($AgNO_3$) in methanol and water, with acetic acid. In the resulting mass spectrum, there were three series of peaks observed. The first of these simply involved the replacement of acidic protons on tryptophan with silver (I) ions, with no subnanometre clusters formed. The other two series of peaks involve one tryptophan, with multiple aggregated silver atoms, not consistent with the replacement of acidic protons with silver ions. These structures involve the loss of one or two hydrogen atoms, such that the silver clusters contain an even number of electrons: $[(Trp)Ag_n - H]^+$ ($n = 2, 4, 6, 8$) and $[(Trp)Ag_n - 2H]^+$ ($n = 5, 7, 9$).

Fragmentation of the $[(Trp)Ag_7 - 2H]^+$ and $[(Trp)Ag_9 - 2H]^+$ clusters using collision induced dissociation in a QIT primarily resulted in the formation of the bare Ag_7^+ and Ag_9^+ subnanometre clusters respectively (5.1a). The bare clusters were found to fragment either by the loss of a neutral silver atom (5.1b), or a neutral silver dimer (5.1c).

$$[(Trp)Ag_n - 2H]^+ \rightarrow Ag_n^+ + [Trp - 2H] \tag{5.1a}$$

$$Ag_n^+ \rightarrow Ag_{n-1}^+ + Ag \tag{5.1b}$$

$$Ag_n^+ \rightarrow Ag_{n-2}^+ + Ag_2 \tag{5.1c}$$

Further experimental work by Dugourd and co-workers investigated the properties of these clusters using photofragmentation experiments[166-168] and density functional theory calculations.[167, 169]

We repeated the experimental procedure described in [165], using the Bruker Esquire 6000 quadrupole ion trap mass spectrometer, a similar instrument to that used in the original work. A solution of tryptophan (1×10^{-4} mol dm^{-3}) and silver nitrate (5×10^{-4} mol dm^{-3}) in a 1:1 (v/v) methanol and water was electrosprayed, keeping the conditions as similar as possible to those of the original experiment. A spectrum, clearly containing both tryptophan and silver was produced (*Figure 5.1*), however, the only peaks visible were the ones in which silver cations replaced acidic protons on tryptophan. No peaks containing silver clusters were visible in the spectrum. Making changes to the sample, including the time before use, pH and relative concentration of silver nitrate and tryptophan had little effect on the spectra obtained.

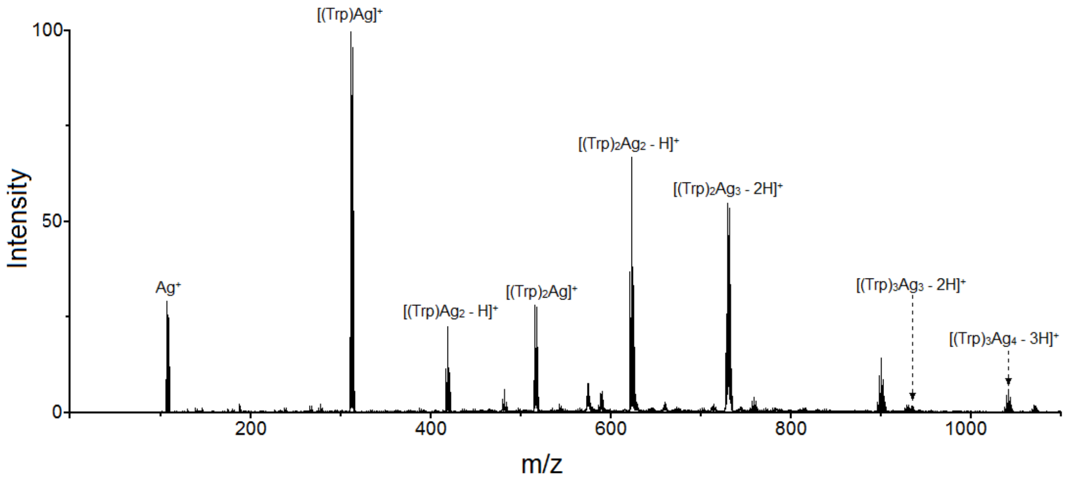

Figure 5.1: Positive ion ESI-MS of tryptophan and silver nitrate. Unlabelled peaks are assigned to species not containing both silver and tryptophan.

While none of the reported silver clusters were produced, fragmentation of $[(\mathrm{Trp})\mathrm{Ag}_3 - 2\mathrm{H}]^+$ was found to produce Ag_3^+ (*Figure 5.2*). This is interesting, as the fragmentation requires reduction of the silver ions, indicating that tryptophan can act as a reducing agent. This process has been previously observed,[163] with silver clusters Ag_n^+ and $\mathrm{Ag}_{n-1}\mathrm{H}^+$ (where n is an odd number) formed by collision induced dissociation of complexes of silver with glycine and *N*,*N*-dimethyl glycine in a quadrupole ion trap mass spectrometer. These silver clusters have been described extensively in the literature, both in the gas phase[164] and in solution.[170]

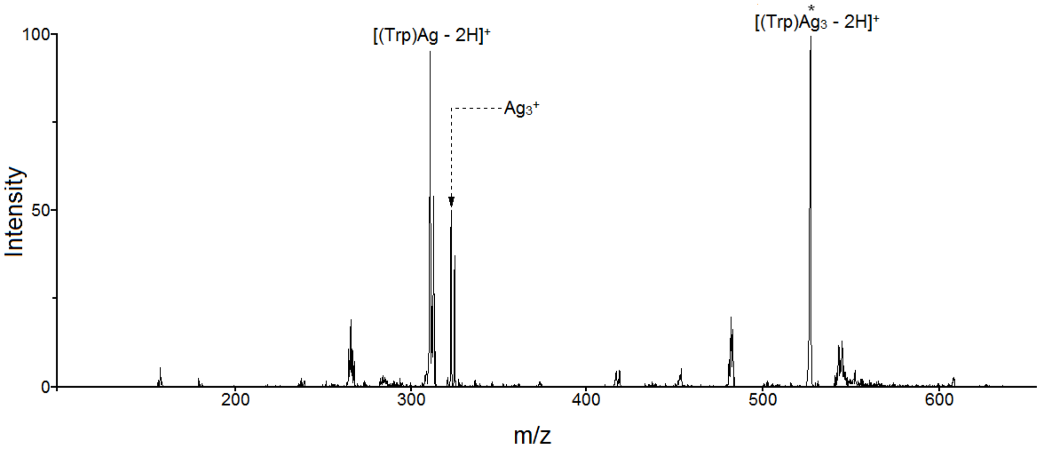

Figure 5.2: MS^3 Positive ion fragment mass spectrum of $[(Trp)Ag_3 - 2H]^+$, formed by the MS^2 fragmentation of $[(Trp)_2Ag_3 - 2H]^+$. Precursor ion is marked with *.

5.3 Histidine and Chloroauric Acid

A number of papers deal with the synthesis of subnanometre particles by the reduction of precursor metal complexes using mild organic reducing agents. A paper by Yang et al.[171] describe a particularly appealing example, in which chloroauric acid ($HAuCl_4$) is used to form Au_{10} clusters, with histidine (His) acting as both a reducing and capping ligand. The reaction was especially appealing, since it only requires the mixing of histidine and chloroauric acid in an aqueous solution for a couple of hours. The resulting solution was analysed by Yang et al. using photoluminescence spectroscopy and mass spectrometry.

We repeated the published synthesis and using the Bruker Esquire 6000 mass spectrometer, produced a mass spectrum that closely matched the one presented in the original paper. Investigation using the quadrupole ion trap mass spectrometer produced a series of metastable peaks, which alongside the somewhat poor resolution of the spectrometer (*m/z* 0.35), made the spectrum difficult to analyse. As a result, the system was analysed using a Bruker SolariX FTICR mass spectrometer, which produced a much clearer spectrum (*Figure 5.3*).

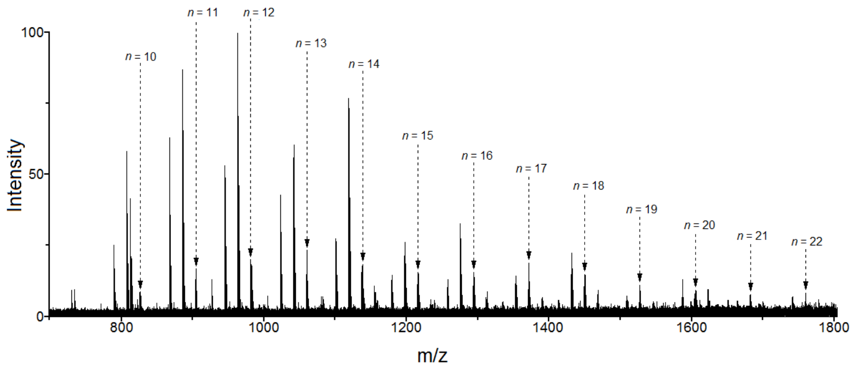

Figure 5.3: Negative ion ESI-FTICR-MS of histidine and chloroauric acid reaction mixture. $[(\mathrm{His})_n\mathrm{Cl}_3 + \mathrm{H}]^{2-}$ peaks are labelled (assigned as $[(\mathrm{His})_{(n\text{-}12)}\mathrm{Au}_{10}]^{2-}$ by Yang et al.).

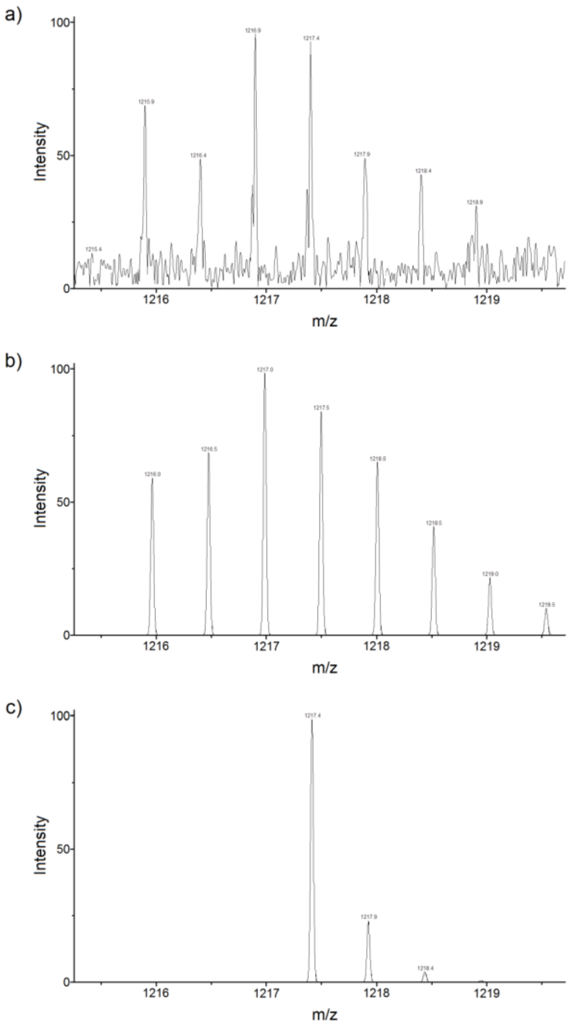

Figure 5.4: a) Experimentally obtained spectrum, showing the isotope pattern for the signal at m/z 1217, b) simulated isotope pattern for $[(\mathrm{His})_{15}\mathrm{Cl}_3 + \mathrm{H}]^{2-}$, c) simulated isotope pattern for $[(\mathrm{His})_3\mathrm{Au}_{10}]^{2-}$.

It was immediately clear that there were a number of issues relating to the interpretation of the original mass spectrum. There were a series of signals, consistent with $[Au_{10}(His)_n]^{2-}$ (n = 1-10), as the paper had described. However, this series continued to lower *m/z* than was described in the paper, continuing to what would be n = -2. Additionally, the signals were comprised of a significant number of isotope peaks (*Figure 5.4*). While the ^{13}C isotope of carbon would produce some isotope peaks, it does not account for the isotope pattern observed. By simulating the isotope patterns of several possible structures, it was found that the signals were a very good fit with $[(His)_nCl_3 + H]^{2-}$ (n = 10-22). This seems plausible, as chlorine could be provided by the chloroauric acid, and various other aggregations of histidine and chlorine were also observed in the mass spectrum.

5.4 Glutathione and Gold Nanoparticles

Zhou et al. describe the production of Au_8 clusters by the etching of gold nanoparticles of various sizes using glutathione with the aid of sonication.[172] The reaction involved the sonication of a vial containing an aqueous solution of glutathione and gold nanoparticles, which was then purified by centrifugation.

The mechanism was proposed to involve a ‘nitrogen atom-activated surface reaction’, in which the glutathione coordinates to the surface of the nanoparticle through a nitrogen atom. Coupled with the effect of sonication, this weakens the strength of the bonding of the gold atoms on the surface of the nanoparticle, causing them to rearrange, potentially resulting in the fragmentation of small gold clusters from the surface. Au_8 has been shown to be a particularly stable cluster, as it is a ‘magic number’ cluster, due to its favourable electronic configuration.[173]

The clusters were analysed by Zhou et al. using UV-vis absorption and photoluminescence spectroscopy and mass spectrometry, using an ESI-Q-TOF mass spectrometer. The synthesis was repeated using several different amino acids as a replacement for glutathione, which produced similar results in the photoluminescence spectra, however, there was no evidence for the Au_8 clusters in the mass spectra. This was attributed to the weak strength of the Au-N gold-amino acid bond, compared to the Au-S gold-glutathione bond, meaning that the clusters would break down in the electrospray source and so would not be visible.

We repeated the experiment using 5 nm gold nanoparticles in a phosphate buffered saline solution, purchased from Sigma-Aldrich. A vial containing an aqueous solution of glutathione (0.01 mol dm^{-3}) and gold nanoparticles (5.5×10^9 particles dm^{-3}) placed into an Ultrawave sonic bath for 8 hours. Over this time, the solution changed colour from a pale red to clear. Unlike in the original work, centrifugation was not used for purification, and the crude reaction mixture was directly analysed.

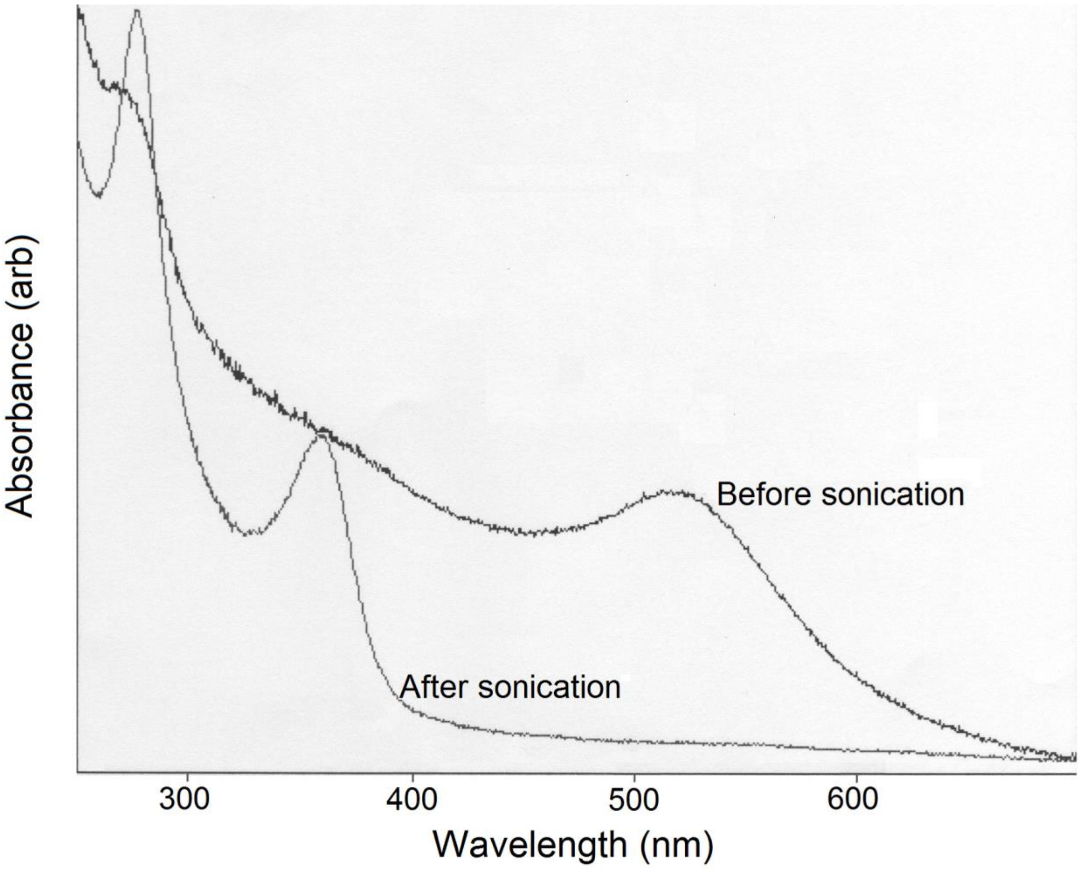

Figure 5.5: UV-vis spectrum of the glutathione and gold nanoparticle reaction mixture before and after sonication.

UV-vis spectroscopy with a Shimadzu UV-2600 spectrometer produced a similar spectrum to the one presented in the paper (*Figure 5.5*). However, analysis by mass spectrometry produced a negative ion spectrum in which the only peaks that could be identified were deprotonated glutathione and deprotonated oxidised glutathione (*Figure 5.6*). There were a number of other peaks in the spectrum, which could not be identified, however none were consistent with the gold clusters described in the paper.

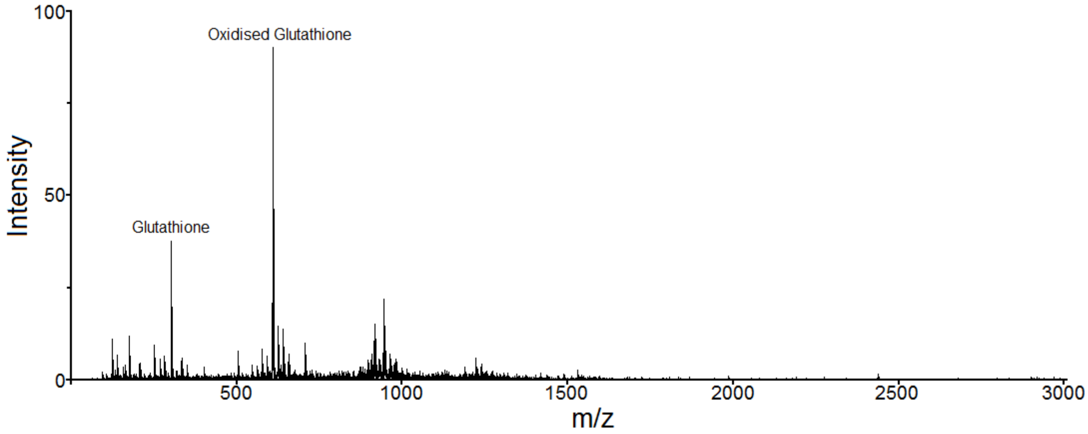

Figure 5.6: Negative ion ESI-MS of glutathione and gold nanoparticle reaction mixture after sonication.

Despite following the original procedure, as the colour of the reaction mixture cleared, a dark purple precipitate formed. While the identity of the precipitate was not confirmed, it seems likely that it is an aggregation of the nanoparticles. EDX spectroscopy[174] could be used to identify the atomic composition of the precipitate, and thus its identity. Repeating the synthesis using a different nanoparticle precursor may provide different results, and therefore would be worth investigating.

5.5 Mercaptosuccinic Acid and Silver Nitrate

Using a solid state method, Ag_9 clusters with a mercaptosuccinic acid (MSA) capping agent were synthesised by Rao et al.[175] Without a solvent, MSA and silver nitrate were ground together for approximately 10 minutes to form an orange intermediate. Solid sodium borohydride was then added and the mixture was ground for a further 10 minutes, reducing the silver to form a brownish black powder containing silver clusters capped with MSA. The clusters were then slowly dissolved in water, precipitated with ethanol, collected using centrifugation and purified using polyacrylamide gel electrophoresis. The clusters were found to slowly decay in an aqueous solution, although they were stable as a solid under laboratory conditions and further rapid analysis using a large number of techniques, including ESI-MS, were possible. The clusters were clearly observable in the resulting mass spectrum as $[Ag_9(MSA)_7 - 2H]^{2-}$ and its sodiated analogues, $[Ag_9(MSA)_7 - (n+2)H + nNa]^{2-}$ (n = 1-12).

Repeating the synthesis, we found that the initial reaction proceeded smoothly and the changes in colour closely matched what was described in the original work. However, upon dissolving the crude product in water and precipitating the clusters out using ethanol, a dark brown product was obtained, in contrast with the ‘reddish brown powder’ observed in the paper. Rather than using centrifuge separation, we collected the precipitate using filter paper, which was not expected to significantly affect the product.

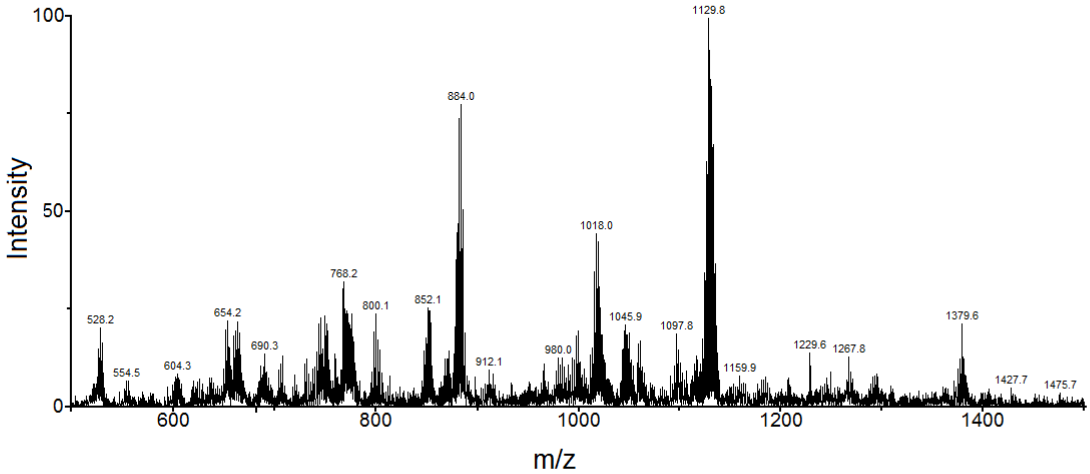

Figure 5.7: Negative ion ESI-MS of MSA and silver nitrate reaction mixture.

The product was immediately analysed using mass spectrometry, which showed a number of unidentifiable peaks, which appear to contain varying numbers of silver atoms, as indicated by the isotope patterns (Figure 5.7). However, there was no trace of the $[Ag_9(MSA)_7 - 2H]^{2-}$ ion. The reason for this is unclear, however, it seems that there is an issue with either dissolving of the crude product in water or the precipitation of the clusters with ethanol, as this is where our reaction mixture appeared to differ from what was described in the original paper. The paper notes that it is important to add the water slowly, as rapid addition will result in the aggregation of the clusters to form larger nanoparticles. While we have replicated this stage multiple times, following the description in the paper as closely as possible, the results have been similar each time. Analysis of the crude product using mass spectrometry produced similar results, with no trace of the Ag_9 cluster.

5.6 Further Work

Of the four methods used to synthesise subnanometre clusters, none were successful. Further searching of the literature identified three promising methods that could be attempted in future work and will be briefly described below.

Wu et al. describe a ‘rationally designed wet chemical method’ for the synthesis of Ag_7 clusters, capped with 2,3-dimercaptosuccinic acid (DMSA).[176] The synthesis first involves the creation of $Ag_x(DMSA)_y$ intermediates by mixing $AgNO_3$ and DMSA in ethanol at 0˚C, which are then reduced to form the silver clusters by the addition of $NaBH_4$. The clusters are only poorly soluble in ethanol, and so precipitate out and are collected by centrifugation. DMSA was found to be a very effective capping agent, as it has two thiol groups, meaning that it is very effective at stabilising small clusters compared to similar monothiols. The clusters were investigated using a number of techniques, most importantly for us, ESI-Q-TOF mass spectrometry. A number of peaks are clearly visible in the published mass spectra, corresponding to $[Ag_7(DMSA)_4]^-$ and its sodiated analogues, $[Ag_7(DMSA)_4$

– nH + nNa]$^-$ (n = 1-5). Further to this, a second paper was published, describing the CID fragmentation of these clusters using a Q-TOF mass spectrometer.[177] Initially, the DMSA ligands fragment to leave just the sulphur atom, producing $[Ag_7S_4]^-$. At higher collision energies, this cluster proceeded to sequentially lose silver atoms from the metal core, eventually leaving S_4^-. A third paper describes the use of these clusters in the degradation of various chlorocarbons.[178]

Bertino et al. describe a simple method for the creation of small gold clusters, Au_n ($n \leq 11$) using diphosphine ligands.[179] Under an inert atmosphere, $Au(PPh_3)Cl$ and a diphosphine capping agent, $P(Ph)_2(CH_2)_mP(Ph)_2$ (L^m) were dissolved in chloroform and a borane tert butylamine complex ($^tBuH_2N{\cdot}BH_3$) reducing agent was added. The products were characterised using UV-vis absorption spectroscopy and ESI-FTICR mass spectrometry. Interestingly, diphosphine ligands with different chain lengths produce different sized gold clusters. The L^3 ligand produced $[Au_{11}(L^3)_5]^{3+}$, L^4 produced a range of clusters, with between 8 and 11 gold atoms, and L^5 produced clusters with between 8 and 10 gold atoms.

Guo et al. used a heterophase etching process to produce Au_8 clusters with a 2-dimethylamino ethanethiol (DMAET) ligand. Previously synthesised nanoparticles, capped with dodecylamine (DDA) were dissolved in toluene and mixed with an aqueous solution of DMAET. This biphasic system was stirred continuously for several days, during which time the dark purple organic layer became transparent. The organic phase was found to contain the Au_8 clusters, which were analysed with UV-vis absorption and photoluminescence spectroscopy, and MALDI-TOF mass spectrometry, which contained only one signal, attributable to $[Au_8(DDA)_2(DMAET)_3]^+$.

5.7 Conclusions

In summary, four different methods for the synthesis of subnanometre clusters were attempted and the products were characterised using mass spectrometry. Ultimately, none of the methods were successful. This is indicative of the synthetic challenges associated with these subnanometre clusters, and suggests that the species synthesised may be relatively unstable. Alternate synthetic pathways may be used to produce more stable subnanometre clusters, suitable for our needs.

Abbreviations

Ad	Adenine
Arb	Arbitrary
Arg	Arginine
°C	Degrees Celsius
CID	Collision Induced Dissociation
Cy	Cytosine
DDA	Dodecylamine
DFT	Density Functional Theory
DMAET	2-Dimethylamino Ethanethiol
DMSA	2,3-Dimercaptosuccinic acid
DNA	Deoxyribonucleic Acid
$E_{1/2}$	Half Energy
EDX	Energy-Dispersive X-ray
ESI	Electrospray Ionisation
FTICR	Fourier Transform Ion Cyclotron Resonance
IMS	Ion Mobility Spectrometry
IR	Infrared
IRMPD	Infrared Multiphoton Dissociation
FWHM	Full Width Half Maximum
His	Histidine

K	Kelvin
L	Litre
m	Metre
MALDI	Matrix-Assisted Laser Desorption Ionisation
MCA	Multiply Charged Anion
mol	Moles
min	Minute
MS	Mass Spectrometry
MSA	Mercaptosuccinic Acid
m/z	Mass to Charge Ratio
PES	Potential Energy Surface
psi	Pounds per Square Inch
QIT	Quadrupole Ion Trap
Q-TOF	Quadrupole-Time of Flight
REMPI	Resonance Enhanced Multiphoton Ionisation
s	Second
Th	Thymine
TOF	Time of Flight
Trp	Tryptophan
Ur	Uracil
UVPD	Ultraviolet Photodissociation
UV-vis	Ultraviolet-Visible
V	Volt

References

1. A. H. J. Wang, G. J. Quigley, F. J. Kolpak, J. L. Crawford, J. H. van Boom, G. van der Marel and A. Rich, *Nature*, 1979, **282**, 680-686.
2. Y. Zhang and P. S. Cremer, *Current Opinion in Chemical Biology*, 2006, **10**, 658-663.
3. J. A. Hinson and D. W. Roberts, *Annual Review of Pharmacology and Toxicology*, 1992, **32**, 471-510.
4. M. S. de Vries and P. Hobza, *Annual Review of Physical Chemistry*, 2007, **58**, 585-612.
5. P. E. Barran, N. C. Polfer, D. J. Campopiano, D. J. Clarke, P. R. R. Langridge-Smith, R. J. Langley, J. R. W. Govan, A. Maxwell, J. R. Dorin, R. P. Millar and M. T. Bowers, *International Journal of Mass Spectrometry*, 2005, **240**, 273-284.
6. K. Müller-Dethlefs and P. Hobza, *Chemical Reviews*, 1999, **100**, 143-168.
7. E. G. Robertson and J. P. Simons, *Physical Chemistry Chemical Physics*, 2001, **3**, 1-18.
8. J. Řezáč and P. Hobza, *Journal of Chemical Theory and Computation*, 2013, **9**, 2151-2155.
9. I. Alkorta and S. J. Grabowski, 2012.
10. Z. Tian and S. R. Kass, *Journal of the American Chemical Society*, 2008, **130**, 10842-10843.
11. J. P. Simons, *Molecular Physics*, 2009, **107**, 2435-2458.
12. M. R. Nimlos, D. F. Kelley and E. R. Bernstein, *The Journal of Physical Chemistry*, 1989, **93**, 643-651.
13. A. Held and D. W. Pratt, *Journal of the American Chemical Society*, 1993, **115**, 9708-9717.
14. E. G. Robertson, M. R. Hockridge, P. D. Jelfs and J. P. Simons, *The Journal of Physical Chemistry A*, 2000, **104**, 11714-11724.
15. J. A. Dickinson, M. R. Hockridge, R. T. Kroemer, E. G. Robertson, J. P. Simons, J. McCombie and M. Walker, *Journal of the American Chemical Society*, 1998, **120**, 2622-2632.
16. G. Meijer, M. S. Vries, H. E. Hunziker and H. R. Wendt, *Applied Physics B*, 1990, **51**, 395-403.

17. A. Lesarri, S. Mata, J. C. Lopez and J. L. Alonso, *Review of Scientific Instruments*, 2003, **74**, 4799-4804.
18. B. R. Veenstra, H. T. Jonkman and J. Kommandeur, *The Journal of Physical Chemistry*, 1994, **98**, 3538-3543.
19. M. Yamashita and J. B. Fenn, *The Journal of Physical Chemistry*, 1984, **88**, 4671-4675.
20. J. B. Fenn, M. Mann, C. K. Meng, S. F. Wong and C. M. Whitehouse, *Science*, 1989, **246**, 64-71.
21. J. B. Fenn, M. Mann, C. K. Meng, S. F. Wong and C. M. Whitehouse, *Mass Spectrometry Reviews*, 1990, **9**, 37-70.
22. M. Karas, D. Bachmann and F. Hillenkamp, *Analytical Chemistry*, 1985, **57**, 2935-2939.
23. J. B. Fenn, *Angewandte Chemie International Edition*, 2003, **42**, 3871-3894.
24. K. Tanaka, H. Waki, Y. Ido, S. Akita, Y. Yoshida, T. Yoshida and T. Matsuo, *Rapid Communications in Mass Spectrometry*, 1988, **2**, 151-153.
25. R. Knochenmuss, *Analyst*, 2006, **131**, 966-986.
26. M. Karas, D. Bachmann, U. Bahr and F. Hillenkamp, *International Journal of Mass Spectrometry and Ion Processes*, 1987, **78**, 53-68.
27. T. Wyttenbach and M. T. Bowers, in *Annual Review of Physical Chemistry*, Annual Reviews, Palo Alto, Editon edn., 2007, vol. 58, pp. 511-533.
28. J. L. Kinsey, *Annual Review of Physical Chemistry*, 1977, **28**, 349-372.
29. T. Uchimura, *Analytical Sciences*, 2005, **21**, 1395-1400.
30. J. A. Barnes and T. E. Gough, *Journal of Chemical Physics*, 1987, **86**, 6012-6017.
31. G. G. Brown, B. C. Dian, K. O. Douglass, S. M. Geyer, S. T. Shipman and B. H. Pate, *Review of Scientific Instruments*, 2008, **79**.
32. N. R. Walker, *Philosophical Transactions: Mathematical, Physical and Engineering Sciences*, 2007, **365**, 2813-2828.
33. E. Nir, K. Kleinermanns and M. S. de Vries, *Nature*, 2000, **408**, 949-951.
34. E. Nir, C. Plützer, K. Kleinermanns and M. de Vries, *The European Physical Journal D - Atomic, Molecular, Optical and Plasma Physics*, 2002, **20**, 317-329.
35. L. Joly, R. Antoine, M. Broyer, P. Dugourd and J. Lemoine, *Journal of Mass Spectrometry*, 2007, **42**, 818-824.
36. D. M. Peiris, Y. Yang, R. Ramanathan, K. R. Williams, C. H. Watson and J. R. Eyler, *International Journal of Mass Spectrometry and Ion Processes*, 1996, **157–158**, 365-378.
37. J. Oomens, B. G. Sartakov, G. Meijer and G. von Helden, *International Journal of Mass Spectrometry*, 2006, **254**, 1-19.

38. D. S. Cornett, M. Peschke, K. Laihing, P. Y. Cheng, K. F. Willey and M. A. Duncan, *Review of Scientific Instruments*, 1992, **63**, 2177-2186.
39. M. W. Forbes, M. F. Bush, N. C. Polfer, J. Oomens, R. C. Dunbar, E. R. Williams and R. A. Jockusch, *The Journal of Physical Chemistry A*, 2007, **111**, 11759-11770.
40. J. T. O’Brien, J. S. Prell, G. Berden, J. Oomens and E. R. Williams, *International Journal of Mass Spectrometry*, 2010, **297**, 116-123.
41. M. F. Bush, J. S. Prell, R. J. Saykally and E. R. Williams, *Journal of the American Chemical Society*, 2007, **129**, 13544-13553.
42. S. A. McLuckey and D. E. Goeringer, *Journal of Mass Spectrometry*, 1997, **32**, 461-474.
43. K. L. Busch, G. L. Glish and S. A. McLuckey, *Mass Spectrometry/Mass Spectrometry: Techniques and Applications of Tandem Mass Spectrometry*, VCH, 1988.
44. L. Sleno and D. A. Volmer, *Journal of Mass Spectrometry*, 2004, **39**, 1091-1112.
45. R. B. Cody, R. C. Burnier and B. S. Freiser, *Analytical Chemistry*, 1982, **54**, 96-101.
46. A. K. Vrkic, T. Taverner and R. A. J. O'Hair, *Journal of the Chemical Society, Dalton Transactions*, 2002, 4024-4034.
47. A. K. Vrkic, T. Taverner, P. F. James and R. A. J. O'Hair, *Dalton Transactions*, 2004, 197-208.
48. O. Y. Ali and T. D. Fridgen, *ChemPhysChem*, 2012, **13**, 588-596.
49. O. Y. Ali, N. M. Randell and T. D. Fridgen, *ChemPhysChem*, 2012, **13**, 1507-1513.
50. R. A. Jockusch, W. D. Price and E. R. Williams, *The Journal of Physical Chemistry A*, 1999, **103**, 9266-9274.
51. E. M. Milner, M. G. D. Nix and C. E. H. Dessent, *The Journal of Physical Chemistry A*, 2011, **116**, 801-809.
52. A. B. Kanu, P. Dwivedi, M. Tam, L. Matz and H. H. Hill, *Journal of Mass Spectrometry*, 2008, **43**, 1-22.
53. D. Collins and M. Lee, *Analytical and Bioanalytical Chemistry*, 2002, **372**, 66-73.
54. R. Guevremont, K. W. M. Siu, J. Wang and L. Ding, *Analytical Chemistry*, 1997, **69**, 3959-3965.
55. B. T. Ruotolo, S.-J. Hyung, P. M. Robinson, K. Giles, R. H. Bateman and C. V. Robinson, *Angewandte Chemie International Edition*, 2007, **46**, 8001-8004.
56. C. Uetrecht, R. J. Rose, E. van Duijn, K. Lorenzen and A. J. R. Heck, *Chemical Society Reviews*, 2010, **39**, 1633-1655.

57. B. T. Ruotolo, J. L. P. Benesch, A. M. Sandercock, S.-J. Hyung and C. V. Robinson, *Nat. Protocols*, 2008, **3**, 1139-1152.
58. E. v. Duijn, A. Barendregt, S. Synowsky, C. Versluis and A. J. R. Heck, *Journal of the American Chemical Society*, 2009, **131**, 1452-1459.
59. A. De Leon, A. F. Jalbout and V. A. Basiuk, *International Journal of Quantum Chemistry*, 2010, **110**, 953-959.
60. R. Kaschner and D. Hohl, *Journal of Physical Chemistry A*, 1998, **102**, 5111-5116.
61. T. van Mourik and R. J. Gdanitz, *Journal of Chemical Physics*, 2002, **116**, 9620-9623.
62. Y. Zhao and D. G. Truhlar, *The Journal of Physical Chemistry A*, 2006, **110**, 5121-5129.
63. E. G. Hohenstein, S. T. Chill and C. D. Sherrill, *Journal of Chemical Theory and Computation*, 2008, **4**, 1996-2000.
64. Y. Zhao and D. Truhlar, *Theoretical Chemistry Accounts*, 2008, **120**, 215-241.
65. S. Grimme, J. Antony, S. Ehrlich and H. Krieg, *Journal of Chemical Physics*, 2010, **132**, 19.
66. F. O. Kannemann and A. D. Becke, *Journal of Chemical Theory and Computation*, 2010, **6**, 1081-1088.
67. J. Antony and S. Grimme, *Physical Chemistry Chemical Physics*, 2006, **8**, 5287-5293.
68. S. Kristyán and P. Pulay, *Chemical Physics Letters*, 1994, **229**, 175-180.
69. Bruker-Daltronics, *Esquire 6000 manual*.
70. G. Taylor, *Proceedings of the Royal Society of London. Series A. Mathematical and Physical Sciences*, 1964, **280**, 383-397.
71. J. N. Smith, R. C. Flagan and J. L. Beauchamp, *The Journal of Physical Chemistry A*, 2002, **106**, 9957-9967.
72. M. Dole, L. L. Mack, R. L. Hines, R. C. Mobley, L. D. Ferguson and M. B. Alice, *The Journal of Chemical Physics*, 1968, **49**, 2240-2249.
73. L. L. Mack, P. Kralik, A. Rheude and M. Dole, *The Journal of Chemical Physics*, 1970, **52**, 4977-4986.
74. J. V. Iribarne and B. A. Thomson, *The Journal of Chemical Physics*, 1976, **64**, 2287-2294.
75. V. Znamenskiy, I. Marginean and A. Vertes, *The Journal of Physical Chemistry A*, 2003, **107**, 7406-7412.
76. S. Nguyen and J. B. Fenn, *Proceedings of the National Academy of Sciences*, 2007, **104**, 1111-1117.
77. S. Banerjee and S. Mazumdar, *International Journal of Analytical Chemistry*, 2012, 40.

78. R. E. March, *Journal of Mass Spectrometry*, 1997, **32**, 351-369.

79. W. Paul, *Angewandte Chemie International Edition in English*, 1990, **29**, 739-748.

80. É. Mathieu, Journal de Mathématiques Pures et Appliquées, Editon edn., 1868, pp. 137-203.

81. J. N. Louris, R. G. Cooks, J. E. P. Syka, P. E. Kelley, G. C. Stafford and J. F. J. Todd, *Analytical Chemistry*, 1987, **59**, 1677-1685.

82. K. Hart and S. McLuckey, *Journal of the American Society for Mass Spectrometry*, 1994, **5**, 250-259.

83. W. E. Boxford and C. E. H. Dessent, *Physical Chemistry Chemical Physics*, 2006, **8**, 5151-5165.

84. M. Satterfield and J. S. Brodbelt, *Inorganic Chemistry*, 2001, **40**, 5393-5400.

85. M. Born and R. Oppenheimer, *Annalen der Physik*, 1927, **389**, 457-484.

86. A. D. Becke, *The Journal of Chemical Physics*, 1993, **98**, 5648-5652.

87. P. Hohenberg and W. Kohn, *Physical Review*, 1964, **136**, B864-B871.

88. N. L. Allinger, Y. H. Yuh and J. H. Lii, *Journal of the American Chemical Society*, 1989, **111**, 8551-8566.

89. V. G. S. Box, *Molecular modeling annual*, 1997, **3**, 124-141.

90. C. J. Cramer, *Essentials of Computational Chemistry*, John Wiley and Sons, 2002.

91. J.-Y. Yi, J. Bernholc and P. Salamon, *Computer Physics Communications*, 1991, **66**, 177-180.

92. A. Urruticoechea, R. Alemany, J. Balart, A. Villanueva, F. Vinals and G. Capella, *Current Pharmaceutical Design*, 2010, **16**, 3-10.

93. S. Nussbaumer, P. Bonnabry, J.-L. Veuthey and S. Fleury-Souverain, *Talanta*, 2011, **85**, 2265-2289.

94. A. M. J. Fichtinger-Schepman, J. L. Van der Veer, J. H. J. Den Hartog, P. H. M. Lohman and J. Reedijk, *Biochemistry*, 1985, **24**, 707-713.

95. E. R. Jamieson and S. J. Lippard, *Chemical Reviews*, 1999, **99**, 2467-2498.

96. P. J. Loehrer and L. H. Einhorn, *Annals of Internal Medicine*, 1984, **100**, 704-713.

97. N. Milosavljevic, C. Duranton, N. Djerbi, P. H. Puech, P. Gounon, D. Lagadic-Gossmann, M. T. Dimanche-Boitrel, C. Rauch, M. Tauc, L. Counillon and M. Poet, *Cancer Research*, 2010, **70**, 7514-7522.

98. M. Frańska, *International Journal of Mass Spectrometry*, 2007, **261**, 86-90.

99. A. E. Egger, C. G. Hartinger, H. B. Hamidane, Y. O. Tsybin, B. K. Keppler and P. J. Dyson, *Inorganic Chemistry*, 2008, **47**, 10626-10633.

100. P. Dolezel and V. Kuban, *Chemical Papers-Chemicke Zvesti*, 2002, **56**, 236-240.

101. C. Silvestri and J. S. Brodbelt, *Mass Spectrometry Reviews*, 2013, **32**, 247-266.
102. J. Talib, C. Green, K. J. Davis, T. Urathamakul, J. L. Beck, J. R. Aldrich-Wright and S. F. Ralph, *Dalton Transactions*, 2008, 1018-1026.
103. D. Garcia Sar, M. Montes-Bayon, E. Blanco Gonzalez and A. Sanz-Medel, *Journal of Analytical Atomic Spectrometry*, 2006, **21**, 861-868.
104. X.-B. Wang, J. B. Nicholas and L.-S. Wang, *The Journal of Chemical Physics*, 2000, **113**, 10837-10840.
105. E. M. Milner, M. G. D. Nix and C. E. H. Dessent, *Physical Chemistry Chemical Physics*, 2011, **13**, 18379-18385.
106. X. Yang, Y.-J. Fu, X.-B. Wang, P. Slavíček, M. Mucha, P. Jungwirth and L.-S. Wang, *Journal of the American Chemical Society*, 2004, **126**, 876-883.
107. D. S. Lambrecht, L. McCaslin, S. S. Xantheas, E. Epifanovsky and M. Head-Gordon, *Molecular Physics*, 2012, **110**, 2513-2521.
108. M. F. Bush, R. J. Saykally and E. R. Williams, *Journal of the American Chemical Society*, 2007, **129**, 2220-2221.
109. C. E. H. Dessent and C. Rigby, *Chemical Physics Letters*, 2003, **370**, 52-61.
110. P. D. Dau, J. Su, H.-T. Liu, J.-B. Liu, D.-L. Huang, J. Li and L.-S. Wang, *Chemical Science*, 2012, **3**, 1137-1146.
111. H. Wicke and A. Meleshyn, *The Journal of Physical Chemistry A*, 2010, **114**, 8948-8960.
112. T. H. Dunning Jr and P. J. Hay, *Modern Theoretical Chemistry, Vol. 3*, New York, 1976.
113. P. J. Hay and W. R. Wadt, *The Journal of Chemical Physics*, 1985, **82**, 299-310.
114. P. J. Hay and W. R. Wadt, *The Journal of Chemical Physics*, 1985, **82**, 270-283.
115. W. R. Wadt and P. J. Hay, *The Journal of Chemical Physics*, 1985, **82**, 284-298.
116. M. J. Frisch, G. W. Trucks, H. B. Schlegel, G. E. Scuseria, M. A. Robb, J. R. Cheeseman, G. Scalmani, V. Barone, B. Mennucci, G. A. Petersson, H. Nakatsuji, M. Caricato, X. Li, H. P. Hratchian, A. F. Izmaylov, J. Bloino, G. Zheng, J. L. Sonnenberg, M. Hada, M. Ehara, K. Toyota, R. Fukuda, J. Hasegawa, M. Ishida, T. Nakajima, Y. Honda, O. Kitao, H. Nakai, T. Vreven, J. A. Montgomery, J. E. Peralta, F. Ogliaro, M. Bearpark, J. J. Heyd, E. Brothers, K. N. Kudin, V. N. Staroverov, R. Kobayashi, J. Normand, K. Raghavachari, A. Rendell, J. C. Burant, S. S. Iyengar, J. Tomasi, M. Cossi, N. Rega, J. M. Millam, M. Klene, J. E. Knox, J. B. Cross, V. Bakken, C. Adamo, J. Jaramillo, R. Gomperts, R. E. Stratmann, O. Yazyev, A. J. Austin, R. Cammi, C. Pomelli, J. W. Ochterski, R. L. Martin, K. Morokuma, V. G. Zakrzewski, G. A. Voth, P. Salvador, J. J. Dannenberg, S. Dapprich, A. D.

Daniels, Farkas, J. B. Foresman, J. V. Ortiz, J. Cioslowski and D. J. Fox, Wallingford CT, Editon edn., 2009.

117. R. M. Burke, W. E. Boxford and C. E. H. Dessent, *The Journal of Chemical Physics*, 2007, **126**, 064308-064309.

118. R. J. Holmes, R. A. J. O'Hair and W. D. McFadyen, *Rapid Communications in Mass Spectrometry*, 2000, **14**, 2385-2392.

119. W. E. Boxford, J. K. Pearce and C. E. H. Dessent, *Chemical Physics Letters*, 2004, **399**, 465-470.

120. X.-B. Wang and L.-S. Wang, *Physical Review Letters*, 1999, **83**, 3402-3405.

121. R. Tonner, P. Schwerdtfeger, A. L. May, J. D. Steill, G. Berden, J. Oomens, S. R. Campagna and R. N. Compton, *The Journal of Physical Chemistry A*, 2012, **116**, 4789-4800.

122. C. L. Exstrom, M. K. Pomije and K. R. Mann, *Chemistry of Materials*, 1998, **10**, 942-945.

123. G. Heger, H. J. Deiseroth and H. Schulz, *Acta Crystallographica Section B*, 1978, **34**, 725-731.

124. X.-B. Wang, Y.-L. Wang, H.-K. Woo, J. Li, G.-S. Wu and L.-S. Wang, *Chemical Physics*, 2006, **329**, 230-238.

125. W. P. Fehlhammer and M. Fritz, *Chemical Reviews*, 1993, **93**, 1243-1280.

126. V. Verdolino, R. Cammi, B. H. Munk and H. B. Schlegel, *The Journal of Physical Chemistry B*, 2008, **112**, 16860-16873.

127. R. C. Dunbar, *Journal of Chemical Education*, 1982, **59**, 22.

128. L. Pauling, *The Journal of Physical Chemistry*, 1954, **58**, 662-666.

129. J. T. Edsall and M. H. Blanchard, *Journal of the American Chemical Society*, 1933, **55**, 2337-2353.

130. P. G. Jonsson and A. Kvick, *Acta Crystallographica Section B*, 1972, **28**, 1827-1833.

131. Z. B. Maksic and B. Kovacevic, *Journal of the Chemical Society, Perkin Transactions 2*, 1999, **0**, 2623-2629.

132. P. Wang, G. Ohanessian and C. Wesdemiotis, *International Journal of Mass Spectrometry*, 2008, **269**, 34-45.

133. E. Leontidis, *Current Opinion in Colloid & Interface Science*, 2002, **7**, 81-91.

134. L. M. Pegram and M. T. Record, *The Journal of Physical Chemistry B*, 2007, **111**, 5411-5417.

135. R. L. Baldwin, *Biophysical Journal*, 1996, **71**, 2056-2063.

136. G. Yang, Y. Zu, C. Liu, Y. Fu and L. Zhou, *The Journal of Physical Chemistry B*, 2008, **112**, 7104-7110.

137. S. X. Tian, H.-B. Li and J. Yang, *ChemPhysChem*, 2009, **10**, 1435-1437.

138. M. F. Bush, J. Oomens, R. J. Saykally and E. R. Williams, *Journal of the American Chemical Society*, 2008, **130**, 6463-6471.

139. C. N. Stedwell, J. F. Galindo, K. Gulyuz, A. E. Roitberg and N. C. Polfer, *The Journal of Physical Chemistry A*, 2013, **117**, 1181-1188.

140. E. M. Milner, MSc Thesis, University of York, 2010.

141. Y. Shao, L. F. Molnar, Y. Jung, J. Kussmann, C. Ochsenfeld, S. T. Brown, A. T. B. Gilbert, L. V. Slipchenko, S. V. Levchenko, D. P. O'Neill, R. A. DiStasio Jr, R. C. Lochan, T. Wang, G. J. O. Beran, N. A. Besley, J. M. Herbert, C. Yeh Lin, T. Van Voorhis, S. Hung Chien, A. Sodt, R. P. Steele, V. A. Rassolov, P. E. Maslen, P. P. Korambath, R. D. Adamson, B. Austin, J. Baker, E. F. C. Byrd, H. Dachsel, R. J. Doerksen, A. Dreuw, B. D. Dunietz, A. D. Dutoi, T. R. Furlani, S. R. Gwaltney, A. Heyden, S. Hirata, C.-P. Hsu, G. Kedziora, R. Z. Khalliulin, P. Klunzinger, A. M. Lee, M. S. Lee, W. Liang, I. Lotan, N. Nair, B. Peters, E. I. Proynov, P. A. Pieniazek, Y. Min Rhee, J. Ritchie, E. Rosta, C. David Sherrill, A. C. Simmonett, J. E. Subotnik, H. Lee Woodcock Iii, W. Zhang, A. T. Bell, A. K. Chakraborty, D. M. Chipman, F. J. Keil, A. Warshel, W. J. Hehre, H. F. Schaefer Iii, J. Kong, A. I. Krylov, P. M. W. Gill and M. Head-Gordon, *Physical Chemistry Chemical Physics*, 2006, **8**, 3172-3191.

142. T. A. Halgren, *Journal of Computational Chemistry*, 1996, **17**, 490-519.

143. J. M. Berg, J. L. Tymoczko and L. Stryer, *Biochemistry. 5th edition*, New York: W H Freeman, 2002.

144. E. A. Braude and F. C. Nachod, *Determination of Organic Structures by Physical Methods*, Academic Press, 1955.

145. M. S. Lehmann, J. J. Verbist, W. C. Hamilton and T. F. Koetzle, *Journal of the Chemical Society, Perkin Transactions 2*, 1973, **0**, 133-137.

146. C. K. Ingold, *Structure and Mechanism in Organic Chemistry*, 2 edn., G. Bell and Sons Ltd., 1969.

147. R. Blatt, P. Gill and R. C. Thompson, *Journal of Modern Optics*, 1992, **39**, 193-220.

148. L. Shimoni and J. P. Glusker, *Protein Science*, 1995, **4**, 65-74.

149. C. A. J. Lin, C. H. Lee, J. T. Hsieh, H. H. Wang, J. K. Li, J. L. Shen, W. H. Chan, H. I. Yeh and W. H. Chang, *Journal of Medical and Biological Engineering*, 2009, **29**, 276-283.

150. J. P. Wilcoxon and B. L. Abrams, *Chemical Society Reviews*, 2006, **35**, 1162-1194.

151. H. Xu and K. S. Suslick, *Advanced Materials*, 2010, **22**, 1078-1082.

152. R. Jin, *Nanoscale*, 2010, **2**, 343-362.

153. I. Diez and R. H. A. Ras, *Nanoscale*, 2011, **3**, 1963-1970.

154. L. Shang, S. Dong and G. U. Nienhaus, *Nano Today*, 2011, **6**, 401-418.

155. Y. Lu, W. Wei and W. Chen, *Chinese Science Bulletin*, 2012, **57**, 41-47.

156. Y. Lu and W. Chen, *Chemical Society Reviews*, 2012, **41**, 3594-3623.

157. T. Laaksonen, V. Ruiz, P. Liljeroth and B. M. Quinn, *Chemical Society Reviews*, 2008, **37**, 1836-1846.
158. J. P. Wilcoxon, J. E. Martin, F. Parsapour, B. Wiedenman and D. F. Kelley, *The Journal of Chemical Physics*, 1998, **108**, 9137-9143.
159. T. Huang and R. W. Murray, *The Journal of Physical Chemistry B,* 2001, **105**, 12498-12502.
160. J. Zheng, C. Zhang and R. M. Dickson, *Physical Review Letters*, 2004, **93**, 077402.
161. C. A. Fields-Zinna, J. S. Sampson, M. C. Crowe, J. B. Tracy, J. F. Parker, A. M. deNey, D. C. Muddiman and R. W. Murray, *Journal of the American Chemical Society*, 2009, **131**, 13844-13851.
162. R. Hamouda, F. Bertorelle, D. Rayane, R. Antoine, M. Broyer and P. Dugourd, *International Journal of Mass Spectrometry*, 2013, **335**, 1-6.
163. G. N. Khairallah and R. A. J. O'Hair, *Dalton Transactions*, 2005, **0**, 2702-2712.
164. G. N. Khairallah and R. A. J. O'Hair, *Angewandte Chemie*, 2005, **117**, 738-741.
165. T. Tabarin, R. Antoine, M. Broyer and P. Dugourd, *The European Physical Journal D - Atomic, Molecular, Optical and Plasma Physics*, 2006, **37**, 237-239.
166. T. Tabarin, R. Antoine, M. Broyer and P. Dugourd, *The European Physical Journal D*, 2009, **52**, 191-194.
167. R. Mitric, J. Petersen, A. Kulesza, V. BonaCic-Koutecky, T. Tabarin, I. Compagnon, R. Antoine, M. Broyer and P. Dugourd, *The Journal of Chemical Physics*, 2007, **127**, 134301-134309.
168. T. Tabarin, R. Antoine, I. Compagnon, M. Broyer, P. Dugourd, R. Mitrić, J. Petersen and V. Bonačić-Koutecký, *The European Physical Journal D*, 2007, **43**, 275-278.
169. R. Mitrić, J. Petersen, A. Kulesza, V. Bonačić-Koutecký, T. Tabarin, I. Compagnon, R. Antoine, M. Broyer and P. Dugourd, *Chemical Physics*, 2008, **343**, 372-380.
170. Y. Xiong, I. Washio, J. Chen, M. Sadilek and Y. Xia, *Angewandte Chemie International Edition*, 2007, **46**, 4917-4921.
171. X. Yang, M. Shi, R. Zhou, X. Chen and H. Chen, *Nanoscale*, 2011, **3**, 2596-2601.
172. R. Zhou, M. Shi, X. Chen, M. Wang and H. Chen, *Chemistry – A European Journal*, 2009, **15**, 4944-4951.
173. P. Pyykko, *Nat Nano*, 2007, **2**, 273-274.
174. S. Pascarelli, O. Mathon, M. Muñoz, T. Mairs and J. Susini, *Journal of Synchrotron Radiation*, 2006, **13**, 351-358.

175. T. U. B. Rao, B. Nataraju and T. Pradeep, *Journal of the American Chemical Society*, 2010, **132**, 16304-16307.

176. Z. Wu, E. Lanni, W. Chen, M. E. Bier, D. Ly and R. Jin, *Journal of the American Chemical Society*, 2009, **131**, 16672-16674.

177. Z. Wu, D.-e. Jiang, E. Lanni, M. E. Bier and R. Jin, *The Journal of Physical Chemistry Letters*, 2010, **1**, 1423-1427.

178. M. S. Bootharaju, G. K. Deepesh, T. Udayabhaskararao and T. Pradeep, *Journal of Materials Chemistry A*, 2013, **1**, 611-620.

179. M. F. Bertino, Z.-M. Sun, R. Zhang and L.-S. Wang, *The Journal of Physical Chemistry B*, 2006, **110**, 21416-21418.